UNIVERSITÀ DEGLI STUDI DI PADOVA

Dipartimento di Fisica e Astronomia "Galileo Galilei"

Master Degree in Physics

Final Dissertation

Development of an improved aberration correction system for optical microscopy

THESIS SUPERVISOR
Prof. Marco Bazzan
Dipartimento di Fisica e Astronomia "Galileo Galilei"

THESIS CO-SUPERVISORS
Dr. Stefano Bonora, Dr. Tommaso Furieri
Istituto di Fotonica e Nanotecnologie, CNR Padova

CANDIDATE
Alexey Vladimirovic Bortoli Saygashev

Academic Year 2023/2024

Introduction

Adaptive optics is a technology that has been theoretized by Horace W. Babcock in 1953; it has been practically implemented in seventies of the previous century for military and successively, at the end of eighties, for astronomical research in order to dynamically correct the atmospheric influence on the imaging systems. The basic principle is the possibility to induce optical aberrations by modification of the incoming light path via an optical element, which surface can be changed using an electromechanical actuation system. Successive development of the technology found further applications in astronomical, biomedical as well as industrial imaging research sectors; in particular, a successful application of adaptive optics in biological microscopy has shown its potential in the last decade.

This work focuses on the experimental use of adaptive optics methods applied to the microscopy. The system makes use of two deformable lenses as adaptive optics elements, that act transmissively; the capability of correction of aberrations over an extended field of view combined with a compact design allows the implementation of an improved adaptive optics framework on a wide class of commercial and custom microscopy systems. This work takes into exam the design, the implementation of the system and estimates experimentally its performance in case of an angularly misaligned sample compared to a single element adaptive optics system.

At first, the theoretical part is introduced: in the first chapter wave optics concepts are given in order to develop a more specialized theoretical description of aberrations and quality evaluation for imaging systems in the third chapter; the second chapter briefly describes the structure of a brightfield microscope while the chapter four talks about the adaptive optics in terms of technology as well as sensing and control procedure. In the experimental part, the chapter five describes the design, the construction, the calibration and the characterization of the optical setup and the adaptive optics instrumentation; in the chapter six, simulations of the system for angularly misaligned sample are run are performed; in the seventh chapter the imaging performance of the system is measured and analyzed in the order to demonstrate the improved capabilities of the adaptive optics on the system.

Acknowledgements

In first place, I want to acknowledge my thesis co-supervisors: I would like to express my deepest appreciation to Dr. Stefano Bonora for giving me the opportunity to work in his laboratory and learn about methods used in adaptive optics; I appreciate his expertise, professionalism and I thank him for the daily supervision, support and suggestions which have been extremely valuable the realization of this thesis; many thanks to Dr. Tommaso Furieri for the support in both theoretical and experimental parts while I was learning about adaptive optics, he helped me a lot with the more technical parts of this work.

I'm very grateful to my thesis supervisor Prof. Marco Bazzan for his valuable advice on this work and for providing his support in the most critical moments of the thesis; I also want to express my appreciation for his teachings that fed my curiosity towards the field of high precision optics.

I acknowledge the people of the research group for their daily support in laboratory; in particular, many thanks to Antonio Vanzo who assisted me in more practical aspects of this work; his criticism and suggestions were very appreciated.

Among the people who haven't directly influenced this work, I'm especially grateful to Prof. Caterina Braggio for helping and guiding me during these years of studies.

Finally, I'm deeply grateful to my dear ones here and far away for caring about me during these years and for their love.

Contents

Part I

Theory

Chapter 1

Scalar diffraction theory of light propagation

The scalar diffraction theory is used to describe the propagation of light and give basic blocks in the order to model the effects seen in an imaging system.

1.1 Plane-wave spectrum representation

The propagation of a monochromatic light wave satisfies the wave equation which can be recasted in terms the Helmholtz equation:

$$(\nabla^2 + k^2)E(x, y, z) = 0, \quad k = \frac{\omega}{c} \tag{1.1}$$

A solution can be chosen in form

$$E(x, y, z) = \hat{E}(k_x, k_y, z)e^{-jk_x x}e^{-jk_y y} \tag{1.2}$$

which, inserted in Equation 1.1 produces

$$\frac{\partial^2 \hat{E}}{\partial z^2}(k_x, k_y, z) = -(k^2 - k_x^2 - k_y^2)\hat{E}(k_x, k_y, z) = -k_z^2 \hat{E}(k_x, k_y, z) \tag{1.3}$$

by solving the equation and requiring forward propagation of waves $(z \geq 0)$

$$\hat{E}(k_x, k_y, z) = \hat{E}(k_x, k_y)e^{-jk_z z} \tag{1.4}$$

The solution Equation 1.4 tells us two possible ways of the wave propagation, respectively in *propagating* (case $k_z = \sqrt{k^2 - k_x^2 - k_y^2} \in j\mathbb{R}$ with $k^2 < k_x^2 + k_y^2$) and *evanescent* (case $k_z = \sqrt{k^2 - k_x^2 - k_y^2} \in \mathbb{R}$ with $k^2 > k_x^2 + k_y^2$) mode.

Two consistently different behaviours are present: while the propagating modes travel indefinitely, the evanescent modes with high spatial frequencies decay during the propagation.

The result is extended to a general case by considering all possible spatial frequencies:

$$E(x, y, z) = \int_{-\infty}^{+\infty} \int_{-\infty}^{+\infty} \hat{E}(k_x, k_y) e^{-jk_z z} e^{-jk_x x} e^{-jk_y y} \frac{dk_x dk_y}{(2\pi)^2} \tag{1.5}$$

This expression is also known as *plane-wave spectrum representation* or *angular spectrum representation*.

The solution of the Helmholtz equation Equation 1.4 can be rewritten as a spatial filter:

$$\hat{E}(k_x, k_y, z) = \hat{h}(k_x, k_y, z) \hat{E}(k_x, k_y) \tag{1.6}$$

where $\hat{h}(k_x, k_y, z) = e^{-jk_z z}$.

$\hat{h}(k_x, k_y, z)$ propagates the Fourier-transformed input field over $z = 0 \to z$.

By making use of the convolution theorem the result can be explicitly written in the real space:

$$E(x, y, z) = \int_{-\infty}^{+\infty} \int_{-\infty}^{+\infty} h(x - x', y - y', z) E(x', y', 0) \, dx' dy' \tag{1.7}$$

1.2   Fresnel diffraction integral

The Rayleigh-Sommerfield diffraction integral (Equation A.11) describes exactly the propagation of a monochromatic beam between the planes along the optical axis z; except for studying extreme near-field cases [21], a more mathematically convenient formulation is used.

The starting point is the The Rayleigh-Sommerfield integral:

$$E(\bar{r}_\perp, z) = \int_S \frac{2z}{R} \left(jk + \frac{1}{R} \right) \frac{e^{-jkR}}{4\pi R} \cdot E(\bar{r}'_\perp, 0) \, d^2\bar{r}'_\perp \tag{1.8}$$

the assumption for the Fresnel approximation is that

$$z \gg |\bar{r} - \bar{r}'| \tag{1.9}$$

$$z \gg \lambda \tag{1.10}$$

Consequently, the distance between the source and the observation point can be expanded to the second order:

$$R = \sqrt{(x - x')^2 + (y - y')^2 + z^2} = \sqrt{|\bar{r} - \bar{r}'|^2 + z^2} = z\sqrt{1 + \frac{|\bar{r}_\perp - \bar{r}'_\perp|^2}{z^2}} \approx z + \frac{|\bar{r}_\perp - \bar{r}'_\perp|^2}{2z} \tag{1.11}$$

and used for the quadratic approximation of the phase:

$$e^{-jkR} \approx e^{-jkz} \cdot e^{-jk|\bar{r}_\perp - \bar{r}'_\perp|^2/2z}$$

The condition $z \gg \lambda$ leads to $k \gg 1/R$, which together with $R \approx z$ simplifies the amplitude term:

$$\frac{2z}{R} \left(jk + \frac{1}{R} \right) \frac{1}{4\pi R} \approx \frac{jk}{2\pi z}$$

As result, the Fresnel propagation integral is:

$$E(\bar{r}_\perp, z) = \frac{jk}{2\pi z} e^{-jkz} \int_S e^{-jk|\bar{r}_\perp - \bar{r}'_\perp|^2/2z} \cdot E(\bar{r}'_\perp, 0) \, d^2\bar{r}'_\perp \tag{1.12}$$

The integral, rewritten in cartesian coordinates assumes the form of a Fourier transform:

$$E(x, y, z) = \frac{jk}{2\pi z} e^{-jkz} \int_S e^{-jk[(x-x')^2 + (y-y')^2]/2z} \cdot E(x', y', 0) \, dx' dy'$$

$$= \frac{jk}{2\pi z} e^{-jkz} e^{-jk(x^2+y^2)/2z} \int_{\mathbb{R}^2} e^{-jk[x'^2+y'^2]/2z} P(x', y') E(x', y', 0) \cdot e^{-jk\left[\frac{x}{z}x' + \frac{y}{z}y'\right]} \, dx' dy' \quad (1.13)$$

the pupil function

$$P(x', y') = \begin{cases} 1 & \text{if } (x', y') \in S \\ 0 & \text{otherwise} \end{cases}$$

is used to recast the integration domain into a Fourier-transformable expression.

The conditions of the validity for Equation 1.12 can be estimated by taking another order of Equation 1.11:

$$R \approx z + \frac{|\bar{r}_\perp - \bar{r}'_\perp|^2}{2z} - \frac{|\bar{r}_\perp - \bar{r}'_\perp|^4}{8z^3}$$

The approximation of the phase has the most sensible contribution on the result; for this reason the phase difference between the exact value and the Fresnel approximation is set be much less than unity:

$$\Delta\phi = k(R - R_{Fresnel}) = \frac{k|\bar{r}_\perp - \bar{r}'_\perp|^4}{8z^3} \ll 1$$

$$z \gg \frac{1}{2} k^{1/3} |\bar{r}_\perp - \bar{r}'_\perp|^{4/3}$$

1.3 Cascading optical elements

The propagation of the light in free space can be described in convolutional terms, as stated in Equation 1.7. This result remains valid in the case of a system with multiple optical elements.

The description can be made by assuming the possibility to express multiplicatively the transmission coefficient (T) due to the presence of an element in the optical plane:

$$E_+(\bar{r}_\perp) = T(\bar{r}_\perp)E_-(\bar{r}_\perp) \quad (1.14)$$

The propagation of the light from the input to the output plane can be consequently written as:

$$E_{out}(\bar{r}_\perp) = \int_S h(\bar{r}_\perp - \bar{u}_\perp, z_2) E_+(\bar{u}_\perp) \, d^2\bar{u}_\perp$$

$$= \int_S h(\bar{r}_\perp - \bar{u}_\perp, z_2) T(\bar{u}_\perp) E_-(\bar{u}_\perp) \, d^2\bar{u}_\perp$$

$$= \int_S \int_S h(\bar{r}_\perp - \bar{u}_\perp, z_2) T(\bar{u}_\perp) h(\bar{u}_\perp - \bar{r}'_\perp, z_1) E_{in}(\bar{r}'_\perp) \, d^2\bar{r}'_\perp d^2\bar{u}_\perp$$

$$= \int_S h(\bar{r}_\perp, \bar{r}'_\perp) E_{in}(\bar{r}'_\perp) \, d^2\bar{r}'_\perp$$

where $h(\bar{u}_\perp, z)$ is the Fresnel propagator between two planes at distance z.

We define $h(\bar{r}_\perp, \bar{r}'_\perp)$ as the *transfer function* between two planes:

$$h(\bar{r}_\perp, \bar{r}'_\perp) = \int_S h(\bar{r}_\perp - \bar{u}_\perp, z_2) T(\bar{u}_\perp) h(\bar{u}_\perp - \bar{r}'_\perp, z_1) \, d^2\bar{u}_\perp \tag{1.15}$$

The case of a system with two or more optical elements can be described in terms of transfer functions:

$$
\begin{aligned}
E_{out}(\bar{r}_\perp) &= \int_S h(\bar{r}_\perp, \bar{r}_{0,\perp}) E_0(\bar{r}_{0,\perp}) \, d^2\bar{r}_{0,\perp} \\
&= \int_S \int_S h(\bar{r}_\perp, \bar{r}_{0,\perp}) h(\bar{r}_{0,\perp}, \bar{r}'_\perp) E_{in}(\bar{r}'_\perp) \, d^2\bar{r}_\perp d^2\bar{r}_{0,\perp} \\
&= \int_S h_{sys}(\bar{r}_\perp, \bar{r}'_\perp) E_{in}(\bar{r}'_\perp) \, d^2\bar{r}_\perp
\end{aligned}
\tag{1.16}
$$

in which transfer functions at the intermediate stages can be integrated away in a more simple expression, which produces another transfer function:

$$h_{sys}(\bar{r}_\perp, \bar{r}'_\perp) = \int_S h(\bar{r}_\perp, \bar{r}_{0,\perp}) h(\bar{r}_{0,\perp}, \bar{r}'_\perp) \, d^2\bar{r}_{0,\perp} \tag{1.17}$$

1.4   Incoherent imaging

A large class of imaging system employs the light sources of incoherent type; following the Equation 1.16 the calculation of the light intensity on the final stage of the system can be calculated as the complex modulus squared of the electric field

$$
\begin{aligned}
I_{out}(\bar{r}_\perp) = |(E_{out}(\bar{r}_\perp)|^2 &= \left(\int_S h_{sys}(\bar{r}_\perp, \bar{r}'_\perp) E_{in}(\bar{r}'_\perp) \, d^2\bar{r}_\perp \right) \left(\int_S h_{sys}(\bar{r}_\perp, \bar{r}'_\perp) E_{in}(\bar{r}'_\perp) \, d^2\bar{r}_\perp \right)^* \\
&= \int_S \int_S h_{sys}(\bar{r}_\perp^\alpha, \bar{r}'^\alpha_\perp) h^*_{sys}(\bar{r}_\perp^\beta, \bar{r}'^\beta_\perp) E_{in}(\bar{r}'^\alpha_\perp) E^*_{in}(\bar{r}'^\beta_\perp) u^{\alpha,\beta} \, d^2\bar{r}_\perp^\alpha d^2\bar{r}_\perp^\beta
\end{aligned}
$$

where $u^{\alpha,\beta} = \begin{cases} 1 & \text{if coherent imaging} \\ \delta_{\alpha,\beta} & \text{if incoherent imaging} \end{cases}$

The second case tells that independent spatial input intensities are enough to reconstruct the intensity profile at the end of the system.

The incoherent imaging integral consequently produces:

$$I_{out}(\bar{r}_\perp) = \int_S |h_{sys}(\bar{r}_\perp, \bar{r}'_\perp)|^2 I_{in}(\bar{r}'_\perp) \, d^2\bar{r}'_\perp \tag{1.18}$$

1.5   Commonly used optical elements

1.5.1   Aperture

An aperture is an element which lets the light propagate freely through a portion of the plane, otherwise the light is absorbed:

$$T(\bar{r}_\perp) = \begin{cases} 1 & \text{if } \bar{r}_\perp \in U \\ 0 & \text{otherwise} \end{cases} \tag{1.19}$$

1.5.2 Lens

A lens is a multipurpose element commonly used to direct and shape the light in imaging applications.

An ideal thin lens is described as a spatial quadratic phase retarder:

$$T(\bar{r}_\perp) = e^{jk|\bar{r}_\perp|^2/2F} \tag{1.20}$$

where F is the focal length of the lens.

Equation 1.20 can be used to obtain a more familiar lensmaker's equation

$$\frac{1}{F} = (n-1)\left(\frac{1}{R_1} - \frac{1}{R_2}\right) \tag{1.21}$$

which derivation approximates the spherical surface of the lens to the second order:

$$\phi(r) = k_0 nd - (n-1)k_0\left(R - R\sqrt{1 - \frac{r^2}{R^2}}\right) \approx k_0 nd - (n-1)k_0\frac{r^2}{2R}$$

in particular, the last term of the expression corresponds to the optical path difference in Equation 1.20.

1.5.3 Phase screen

A general description of elements that act on the spatial profile of the phase, without introducing attenuations, is given as:

$$T(\bar{r}_\perp) = e^{jk\phi(r_\perp)}, \quad \phi(r_\perp) \in \mathbb{R} \tag{1.22}$$

This model is useful to represent the behaviour of adaptive optics elements, which can control the light phase in a non-trivial spatial-dependent way.

Chapter 2

Infinity-corrected bright-field microscope

A microscope is an instrument that creates images of objects, by illuminating and magnifying them, to study and analyse their specific parts. Most important functional parts are explained in the following sections.

2.1 Objective

One of the most critical elements of a microscope is the objective, which is a system of lenses that collects the light incoming through the sample; it is one of most costly parts of the microscope due to its role in producing images without distortions. A simple lens disperses the light at different wavelengths via *chromatic aberration*, which causes the creation of distorted images at different wavelenghts to the shift of the focal position along the optical axis; the problem can be addressed by using different refractive index lenses at the cost of introducing other spatial aberrations.

Consequently, for high performance applications the objective results in a complex system of high quality lenses; the objective can be classified based on their performance in correction of:

- chromatic aberrations: respectively achromat (which corrects chromatic aberration for red and blue colors), fluorite, apochromat (which corrects for red, green and blue colors) and super apochromat (four colors); this, while also trying to keep geometrical aberrations under control.

- spatial flatness: respectively simple achromat (65% of field flatness), semi-plan (80% of field flatness), plan (95% of field flatness).

The objective design specifies the *magnification* of the object on the resulting image and the *numerical aperture (NA)* which is the number that defines the acceptance angle of the light from the object.

A typical research microscope employs a design based on infinity-corrected objectives; this type of objectives create an image at the infinity and allows to focalize it at a finite distance with aid of a tube lens. Light is collimated at the intermediate stage; this configuration makes easier to the reason about the wavefront and insert additional instrumentation that performs wavefront shaping.
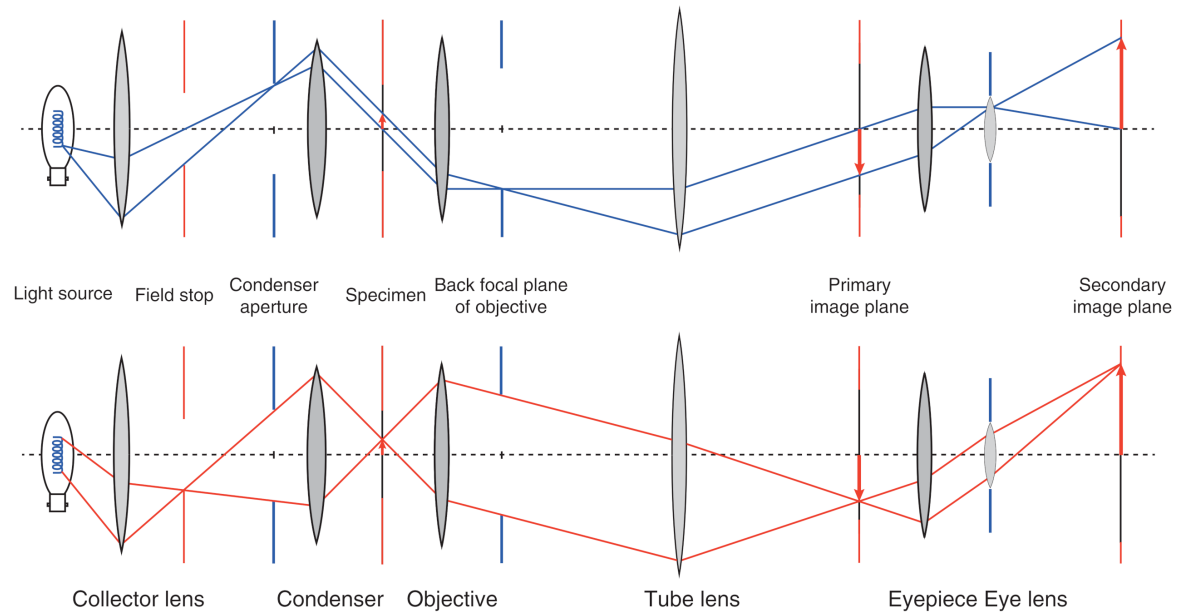
Figure 2.1: Köhler illumination schematics. The illumination path (above) is constructed to ensure a uniform sample illumination that doesn't produce an image of the illumination source; the image path of the specimen is represented (below). Source: Ulrich Kubitscheck, Fluorescence Microscopy From Principles to Biological Applications, sec. 2.2 [8]

2.2   Imaging and illumination paths

A bright-field microscope works by directing the illumination source through the imaging sample of interest and collecting the light on the plane where the image is formed.

There are two optical paths that determine the properties of the microscope:

- The imaging path, describes the light rays that start from the plane where the object stays (*object plane*) to the plane where its' image is produced (*image plane*). In this configuration the rays from the object plane are collimated by the objective, follow parallel paths and are focalized to the image plane, where a sensor is placed; the visualization by eye requires to create a second image plane, using an auxiliary eyepiece lens; the observer's eye lens will focalize the image on the surface of the retina.

- The illumination path defines how the light source acts in relationship to the image formation; in the desirable configuration illumination source doesn't caused the imaging of its sharp features and it possesses a spatially uniform distribution in the image plane.

  This requirement can be implemented using the Köhler illumination scheme.

  Köhler illumination employs following elements for its realization:

  - a non-coherent light source, like a halogen lamp or a light emitting diode (LED);

  - a collector stage, made of a lens system followed by a adjustable field aperture;

  - a condenser stage, made of an adjustable aperture followed by a system of lenses.

  The resulting configuration produces a pencil of parallel rays of the illumination source on the sampled specimen; in particular, every ray from the light source reaches the sample from

different directions, providing a uniform illumination. The illumination doesn't form an image in the image plane of the sample, resulting in absense of sharp features of the light source.

The field aperture can be used to adjust the size of the illumination region due to being conjugated to the plane of the sample. The condenser aperture size to adjusts the illumination brightness as well as resolution capabilities of the microscope, due to the change of the numerical aperture of the illumination; its position determines the position of the illumination region.

2.3 Sensor

The imaging sensor is the final stage of a microscope, which has the role of collecting the image forming light; it is responsible for translating the data from the analogical to the digital domain.

In the selection of the sensor some of experimental conditions need to be satisfied:

- *pixel size* of the sensor: this parameter limits (within the diffraction limit) the minimum distance can be separated in the image space of the system. Lower pixel sizes allow to resolve details better, while trading-off on the size of the field of view.

- *bit depth*: higher number of signal resolution bits allows to observe intensity variations with greater detail and increase the information for the analysis.

- *speed and throughput*: faster image collection allows to have a feedback on the optical system with less delay; while not critical for static imaging, it becomes useful to keep image collection rate high when adaptive optics methods are used.

Other camera properties like noise, integration time, exposure dynamic range, quantum efficiency at specific wavelength are to be taken into account, dependently on the particular experiment.

The currently employed sensors are based on CCD (coupled-charged device) and CMOS (complementary metal-oxide-semiconductor) technologies for the conversion of the incoming photons to the electric signal; while CCD sensors has been extensively used for long time, CMOS sensors have taken place due to a comparable performance and a lower cost; while CCD technology tends to produce lower electronic noise, CMOS performs better in terms of speed and power consumption. EM-CCD (electron multiplying CCD) technology is worth to be mentioned due to extremely low noise performance, which allows to perform single-photon detection experiments.

Chapter 3

Theory of aberrations in an optical system

In order to describe the effects of aberrations, some simple models that result in the formation of images are considered. The addition of aberrations will produce effects that will degrade the quality of the resulting image.

3.1 Image formation

The simplest case of the image formation results in through a lens.

The transfer through the system can be calculated using Equation 1.15 combined with effects caused by a lens Equation 1.20, in Fresnel propagation regime Equation 1.12.

$$h(\bar{r}_\perp, \bar{r}_\perp^{in}) = \int_{\mathbb{R}^2} h(\bar{r}_\perp - \bar{u}_\perp, z_2) T(\bar{u}_\perp) h(\bar{u}_\perp - \bar{r}_\perp^{in}, z_1) \, d^2\bar{u}_\perp \tag{3.1}$$

$$E_{out}(\bar{r}_\perp) = \int_{\mathbb{R}^2} h(\bar{r}_\perp, \bar{r}_\perp^{in}) E_{in}(\bar{r}_\perp^{in}) \, d^2\bar{r}_\perp^{in} \tag{3.2}$$

By writing the transfer function of the system explicitly:

$$h(\bar{r}_\perp, \bar{r}_\perp^{in}) = \int_{\mathbb{R}^2} \frac{jk}{2\pi z_1} e^{jk|\bar{u}_\perp - r_\perp^{in}|^2/2z_1} \cdot e^{jk|\bar{u}_\perp|^2/2F} \cdot \frac{jk}{2\pi z_2} e^{jk|\bar{r}_\perp - \bar{u}_\perp|^2/2z_2} \, d^2\bar{u}_\perp =$$

$$-\frac{k^2}{(2\pi)^2} \frac{1}{z_1 z_2} \int_{\mathbb{R}^2} \exp\left\{ jk \left[|\bar{u}_\perp|^2 \left(-\frac{1}{2z_1} - \frac{1}{2z_2} + \frac{1}{2F} \right) + \bar{u}_\perp \cdot \left(\frac{\bar{r}_\perp^{in}}{z_1} + \frac{\bar{r}_\perp}{z_2} \right) - \frac{|\bar{r}_\perp^{in}|^2}{2z_1} - \frac{|\bar{r}_\perp|^2}{2z_2} \right] \right\} d^2\bar{u}_\perp \tag{3.3}$$

the image formation condition is verified in case of cancellation of $|\bar{u}_\perp|^2$ term:

$$\frac{1}{z_1} + \frac{1}{z_2} = \frac{1}{F} \tag{3.4}$$

because the integral above results in a Dirac delta:

$$h(\bar{r}_\perp, \bar{r}_\perp^{in})^{IF} = -\frac{j}{2\pi} \frac{1}{z_1 z_2} \cdot \exp\left[jk \left(-\frac{|\bar{r}_\perp^{in}|^2}{2z_1} - \frac{|\bar{r}_\perp|^2}{2z_2} \right) \right] \cdot \delta\left(\frac{\bar{r}_\perp^{in}}{z_1} + \frac{\bar{r}_\perp}{z_2} \right) \tag{3.5}$$

nevertheless, this corresponds to transfering a delta impulse of the electric field from the input plane (*object plane*) to the output plane (*image plane*).

$$E_{in}(\bar{r}_\perp^{in}) = \delta(\bar{r}_\perp^{in} - \bar{r}_{\perp,0})$$

$$E_{out}(\bar{r}_\perp) = -\frac{j}{2\pi z_1} \exp\left[jk\left(-\frac{|r_{0,\perp}|^2}{2z_1} - \frac{|r_\perp|^2}{2z_2}\right)\right] \delta\left(\bar{r}_\perp + \frac{z_2}{z_1}\bar{r}_{0,\perp}\right) \tag{3.6}$$

We also see that the delta sets a relationship between the initial and the final impulse position on the optical planes, which is expressed by the *magnification* term:

$$M = -\frac{z_2}{z_1} \tag{3.7}$$

3.2   Point spread function and resolution limit

A real optical system cannot propagate the light from the whole optical plane; this system can be modelled by inserting a (circular) aperture in the lens plane, by using the following transmission relation:

$$T(\bar{u}_\perp) = T_{apert}(\bar{u}_\perp) \cdot T_{lens}(\bar{u}_\perp) = u_{C_R}(u_\perp) \cdot e^{jk|\bar{u}_\perp|^2/2F}$$

this is reflected on the transfer function, now integrated only over a finite circle C_R of radius R:

$$h(\bar{r}_\perp, \bar{r}_\perp^{in}) = \int_{\mathbb{R}^2} \frac{jk}{2\pi z_1} e^{jk|\bar{u}_\perp - r_\perp^{in}|^2/2z_1} \cdot u_{C_R}(u_\perp) \cdot e^{jk|\bar{u}_\perp|^2/2F} \cdot \frac{jk}{2\pi z_2} e^{jk|\bar{r}_\perp - \bar{u}_\perp|^2/2z_2} d^2\bar{u}_\perp =$$

$$-\frac{k^2}{(2\pi)^2} \frac{1}{z_1 z_2} \int_{C_R} \exp\left\{jk\left[|\bar{u}_\perp|^2\left(-\frac{1}{2z_1} - \frac{1}{2z_2} + \frac{1}{2F}\right) + \bar{u}_\perp \cdot \left(\frac{\bar{r}_\perp^{in}}{z_1} + \frac{\bar{r}_\perp}{z_2}\right) - \frac{|\bar{r}_\perp^{in}|^2}{2z_1} - \frac{|\bar{r}_\perp|^2}{2z_2}\right]\right\} d^2\bar{u}_\perp \tag{3.8}$$

By following the reasoning of the previous section and considering the image forming case ($1/z_1 + 1/z_2 = 1/F$) the resulting integral is obtained:

$$\int_0^R \int_0^{2\pi} \exp\left(jk\bar{r} \cdot \left(\frac{\bar{r}_\perp^{in}}{z_1} + \frac{\bar{r}_\perp}{z_2}\right)\right) r\,dr\,d\theta$$

$$= \int_0^R \int_0^{2\pi} \exp\left(jkr\left(\frac{|\bar{r}_\perp^{in}|}{z_1}\cos(\theta) + \frac{|\bar{r}_\perp|}{z_2}\cos(\theta + \alpha)\right)\right) r\,dr\,d\theta =$$

$$= \int_0^R \int_0^{2\pi} \exp\left(jkr(q\cos(\theta + \alpha))\right) r\,dr\,d\theta =$$

$$= 2\pi \int_0^R J_0\left(kr \cdot q\right) r\,dr =$$

$$= 2\pi \frac{R}{kq} J_1\left(kR \cdot q\right) \tag{3.9}$$

Harmonic addition theorem has been used to reduce the number of $\cos(\theta)$ terms to one and to be able to integrate the expression.

So finally:

$$h(\bar{r}_\perp, \bar{r}_\perp^{in}) = -\frac{1}{2\pi} \frac{kR}{z_1 z_2} \frac{1}{q} \exp\left(-jk\left(\frac{|\bar{r}_\perp^{in}|^2}{2z_1} + \frac{|\bar{r}_\perp|^2}{2z_2}\right)\right) \cdot J_1\left(kR \cdot q\right)$$

where $q = \sqrt{\left(\frac{|\bar{r}_\perp^{in}|}{z_1}\right)^2 + \left(\frac{|\bar{r}_\perp|}{z_2}\right)^2 + 2\frac{|\bar{r}_\perp^{in}|}{z_1}\frac{|\bar{r}_\perp|}{z_2}\cos\alpha} = \left|\frac{\bar{r}_\perp^{in}}{z_1} + \frac{\bar{r}_\perp}{z_2}\right|$; α is the angle between vectors $\bar{r}_\perp^{in}$ and $\bar{r}_\perp$; $J_1(x)$ is the Bessel function of the first kind, first order.

The resulting electric field in the image plane, starting from a Dirac delta impulse ($E_{in}(r_\perp^{in}) = \delta(\bar{r}_\perp^{in} - \bar{r}_{\perp,0})$) is:

$$E_{out}(\bar{r}_\perp) = \int_{\mathbb{R}^2} h(\bar{r}_\perp, \bar{r}_\perp^{in})\delta(\bar{r}_\perp^{in} - \bar{r}_{\perp,0})\, d^2\bar{r}_\perp^{in}$$
$$= h(\bar{r}_\perp, \bar{r}_{\perp,0}) \tag{3.10}$$

This expression is called *point spread function (PSF)* and it quantifies the smearing effect of the optical system on the spatial distribution of the electric field in the image plane. Due to the convolutional action of the point spread function, its representation results evident in case of the input Dirac delta field.

Remembering how $h(\bar{r}_\perp, \bar{r}_\perp^{in})$ acts in the context of the non-coherent imaging (Equation 1.18), it is possible to write the intensity version of the point spread function

$$|h(\bar{r}_\perp, \bar{r}_\perp^{in})|^2 = \frac{1}{4\pi^2}\left(\frac{k^2 R^2}{z_1 z_2}\right)^2 \cdot \frac{J_1^2\left(kR \cdot q\right)}{(kR \cdot q)^2} \tag{3.11}$$

So that:

$$I_{out}(\bar{r}_\perp) = \int_{\mathbb{R}^2} |h(\bar{r}_\perp, \bar{r}_\perp^{in})|^2 \delta(\bar{r}_\perp^{in} - \bar{r}_{\perp,0})\, d^2\bar{r}_\perp^{in}$$
$$= |h(\bar{r}_\perp, \bar{r}_{\perp,0})|^2$$

By comparing Equation 3.6 and Equation 3.10 we see that finite lens transfer function extends over the space, forming the Airy disk pattern; this leads to the lose of resolution, which is the capacity of the system to separate sources of fields, seen in the image plane, at a certain distance one from the other.

The *resolution* along the xy-plane of an optical system is defined as the distance between the center and the first zero of the field in the object plane, which is the minimum distance that allows to image separately two point-like light sources with that system.

Considering the finite lens we write the field in the center of the image plane generated by a delta source in the center of the object plane:

$$h(\bar{0}, \bar{r}_\perp^{in}) = -\frac{1}{2\pi} \frac{kR}{z_1 z_2} \left|\frac{z_1}{\bar{r}_\perp^{in}}\right| \exp\left(-jk\frac{|\bar{r}_\perp^{in}|^2}{2z_1}\right) \cdot J_1\left(kR \cdot \left|\frac{\bar{r}_\perp^{in}}{z_1}\right|\right)$$

the source is displaced ($\bar{r}_\perp^{in}$) until a first zero of the field in the image plane ($\bar{r}_\perp = \bar{0}$) is found, which equivalently corresponds to solve to condition $h(\bar{0}, \bar{r}_\perp^{in}) = J_1(v) = 0$ in v; this gives the limit on the resolution of the system:
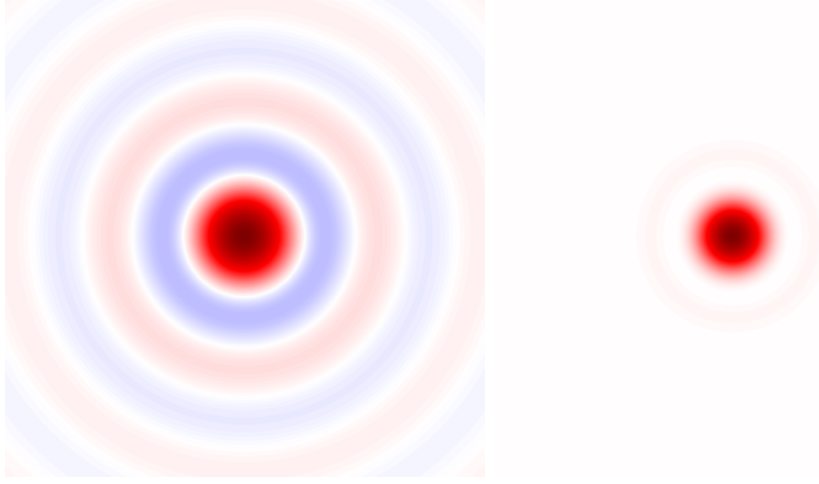
Figure 3.1: The point spread function of a diffraction-limited image is the *Airy disk* pattern; the value of the function $(h(\bar{0}, \bar{r}_\perp^{in}))$ is presented in the left figure, with the additional quadratic phase terms discarded; the intensity version for non-coherent imaging $(|h(\bar{0}, \bar{r}_\perp^{in})|^2)$ is on the right. First 3 maxima are visualized in the figure.

$$v = kR \left| \frac{\bar{r}_\perp^{in}}{z_1} \right| = 3.832$$

$$|\bar{r}_\perp^{in}| = \frac{v\lambda}{2\pi R} \cdot |z_1| = 0.610 \cdot \frac{\lambda}{NA} \tag{3.12}$$

with NA the numerical aperture of the objective, which is definited as:

$$NA = n \sin(\alpha) \tag{3.13}$$

where n is the refractive index between the object and the first optical element of the system; $\sin \alpha = D/(2f)$ where D is the diameter of the light accepting region of the objective and f the lens' focal length.

3.3 Collimated wavefront at the focal plane of the lens

Let's analyze the case the image plane distance from lens is its focal distance F; the input wavefront is calculated from the pupil.

For this calculation the direct Fresnel propagation formula (Equation 1.12) is used.

The initial electric field $E(\bar{r}_\perp^{in})$ is modelled as a plane wavefront passing through the aperture C_R; for multiplication by a quadratic phase term translates the action of the lens with focal length F in analytic form; the result can be expressed as follows:

$$E(\bar{r}_\perp^{in}) P(\bar{r}_\perp^{in}) = 1 \cdot e^{-jk|\bar{r}_\perp^{in}|/2F} \cdot u_R(\bar{r}_\perp^{in})$$

where

$$u_R(\bar{r}_\perp^{in}) = \begin{cases} 1 & \text{if } |\bar{r}_\perp^{in}| \le R \\ 0 & \text{otherwise} \end{cases}$$

The required expression is consequently:

$$E(\bar{r}_\perp, z) = \frac{jk}{2\pi z}e^{-jkz} \int_{\mathbb{R}^2} e^{-jk|\bar{r}_\perp - \bar{r}'_\perp|^2/2z} \cdot e^{-jk|\bar{r}_\perp^{in}|/2F} u_{C_R}(\bar{r}'_\perp) \, d^2\bar{r}'_\perp$$

By setting the image plane in the back-focal plane of the lens $z = F$, and by using explicit cartesian coordinates, the expression is simplified with the cancellation of the quadratic factor of the Fresnel propagation term:

$$E(x, y, z) = \frac{jk}{2\pi F}e^{-jkF}e^{-jk(x^2+y^2)/2F} \int_{\mathbb{R}^2} e^{-jk(x'^2+y'^2)/2F} u_{C_R}(x', y')e^{jk(x'^2+y'^2)/2F}e^{-jk\left(\frac{x}{F}x'+\frac{y}{F}y'\right)} \, dx'dy'$$

$$= \frac{jk}{2\pi F}e^{-jkF}e^{-jk(x^2+y^2)/2F} \int_{\mathbb{R}^2} u_{C_R}(x', y') \exp\left[-jk\left(\frac{x}{F}x' + \frac{y}{F}y'\right)\right] \, dx'dy' \tag{3.14}$$

which is the Fourier transform of the aperture, apart from some multiplicative phase terms.

The integration strategy is the same of section 3.2, after recasting the expression in polar coordinates.

The resulting field $E(\bar{r}_\perp, F)$ is the diffraction limited Airy disc function:

$$E(\bar{r}_\perp, F) = \frac{jR}{|\bar{r}_\perp|}e^{-jkF}e^{-jk\frac{|\bar{r}_\perp|^2}{2F}} \cdot J_1\left(\frac{kR}{F}|\bar{r}_\perp|\right) \tag{3.15}$$

3.4 Zernike polynomials

Optical systems are affected by distortions that degrade the resulting images; this can happen due to a variety of causes that include low-performance optics, misalignment of elements as well as external sources that induce alterations of the refractive index along of the path followed by light rays, such as temperature; the accumulation of these distortions produce relevant relative phase changes among the light rays travelling through the system.

The measurement of of these distortions is usually performed on a collimated wavefront and at the pupil plane of the system, which corresponds to the back focal plane of the objective; in particular, the object plane results to be Fourier-transformed in this plane, as discussed in section 3.3 by applying Fresnel propagation methods.

The wavefront in the pupil plane $\Phi(\bar{r}_\perp)$ can be separated in amplitude and phase terms of the incoming electric field $E(\bar{r}_\perp)$:

$$E(\bar{r}_\perp) = A_{exit}(\bar{r}_\perp) \cdot \exp\left(j\Phi(r_\perp)\right) \tag{3.16}$$

it's important to notice the phase value can depend on the wavelength of the incoming light rays $\Phi(\lambda)$, which in bright-field microscopy is not monochromatic; due to the microscope design (achromatic objectives and low n-dependence of the tube lens) it is possible to neglect the dependency over the area of the image.

The wavefront is decomposed as:

$$\Phi(r, \theta) = \sum_{q=0}^{\infty} a_q Z_q(r, \theta) \tag{3.17}$$

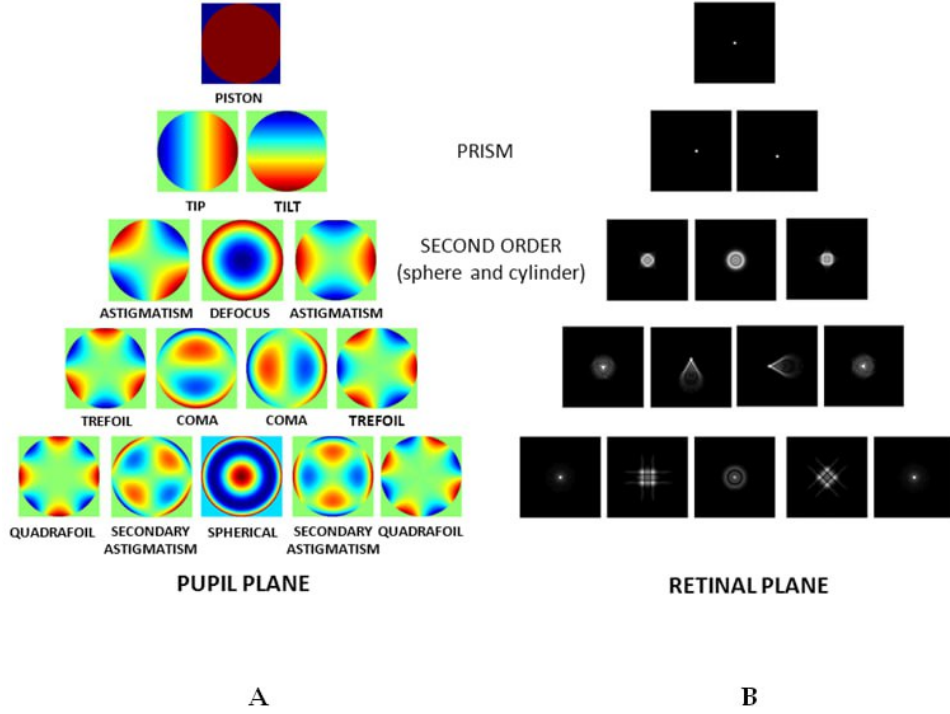using an orthogonal set of functions defined over a unitary circle and called *Zernike polynomials* set:

Figure 3.2: Zernike modes us to 4th order (left) with the relative PSF (right)

$$Z_q(r, \theta) = Z_n^m(r, \theta) = \begin{cases} N_n^m R_n^{|m|}(r) \cdot \cos(m\theta) & \text{if } m \geq 0 \\ N_n^m R_n^{|m|}(r) \cdot \sin(|m|\theta) & \text{if } m < 0 \end{cases} \tag{3.18}$$

$$R_n^{|m|}(r) = \sum_{s=0}^{(n-|m|)/2} \frac{(-1)^s (n-s)!}{s! \left(\frac{n+|m|}{2} - s\right)! \left(\frac{n-|m|}{2} - s\right)!} r^{n-2s} \tag{3.19}$$

$$N_n^m = \sqrt{\frac{2(n+1)}{(1 + \delta_{m,0})}} \tag{3.20}$$

with $q \in \mathbb{Z}, q \geq 0$; $n \in \mathbb{Z}, n = \lfloor(\sqrt{2q-1} + 1/2) - 1\rfloor$ and $m \in \mathbb{Z}, |m| \leq n, m = n \mod 2$.

In this work the OSA/ANSI/ISO 24157 notation is used, but the other different conventions on indexes can be chosen [12].

The orthonormality condition can be verified by integrating the modes over the unit circle domain:

$$\int_0^1 \int_0^{2\pi} Z_n^m(r, \theta) Z_{n'}^{m'}(r, \theta) \, r \, dr \, d\theta = \delta_{n,n'} \delta_{m,m'} \tag{3.21}$$

Let the wavefront $W(r, \theta) = \sum_{q=0}^{\infty} a_q Z_q(r, \theta)$, then the following relationship holds:

$$RMS = \sqrt{\left[\frac{1}{\pi} \int_0^{2\pi} \int_0^1 (W(r, \theta) - W_{mean})^2 \, r \, dr \, d\theta\right]} = \sqrt{\sum_{q=0}^{\infty} |a_q|^2} \tag{3.22}$$

where $W_{mean} = \frac{1}{\pi} \int_0^{2\pi} \int_0^1 W(r, \theta) \, r \, dr \, d\theta$; this relationship defines the *root mean squared (RMS)* value of the wavefront; specifically, RMS grows only with the growth of aberration coefficients and its calculation can be performed in a simple manner.

The Figure 3.2 graphically shows Zernike modes up to 4th order.

3.5 Typical aberrations in bright-field microscopy

Even a well designed microscopy setup can suffer from aberrations; some of common bright microscopy aberrations are presented below:

- *spherical aberration* (Z_4^0): this aberration is related to the mismatch between the refractive index of sample immersion medium and the objective refractive index (for example a water-based sample with an oil-immersion objective); another cause of the matmatch can be the use of a coverslip that produces an additional optical path modification that gives rise to this aberration; temperature and sample thickness are other causes for this aberration. It can be corrected using an objective correction collar, but not all objectives provide this option;

- *astigmatism* ($Z_2^{\pm2}$): this aberration creates a focus mismatch along the perpendicular axes of the image plane, resulting in two different focus positions for each axis; this results in a degraded resolution of the image at the best focus position;

- *coma* ($Z_3^{\pm1}$): it arises from not perfectly aligned or tilted lenses, it creates a comet-like shaped PSF in the image plane of the system.

Among wide-field aberrations the following present:

- *barrel / pin-cushion distortions*: these distortions globally modify the image, with resulting stretching or compression of the observed field of view;

- *Petzval field curvature*: this wide-field aberration is generated due to the fact the image cannot be generated on a planar detector, but rather a spherical surface; this results in a radially-increasing defocus aberration in the wide field of view;

- *anisoplanatic aberrations*: a non-uniform depth of the sample induces additional aberrations that decrease the resolution; being these aberrations dependent on the sample extension, the resulting image has a worsened quality in a position-dependent way.

Chromatic aberrations become relevant in case when using a wide range of the spectrum, in this case using the microscope designs and objectives that minimize chromatic aberrations is suggested.

3.6 Image quality estimation

In the context bright-field microscopy, the quality of an image is directly related to its sharpness; consequently, informations about its spatial properties become critical. A method that helps to separate large and small-scale features is provided by Fourier optics (as in Goodman [6], sections 6.3 and 6.4).

The intensity distribution through an incoherent system can be represented as seen in Equation 1.18:

$$I_{out}(\bar{r}_\perp) = \int_S |h_{sys}(\bar{r}_\perp, \bar{r}'_\perp)|^2 I_{in}(\bar{r}'_\perp) \, d^2\bar{r}'_\perp$$

which can be translated into Fourier domain, by making use of the convolution theorem:

$$\mathcal{G}_{out}(f_x, f_y) = \mathcal{H}(f_x, f_y) \cdot \mathcal{G}_{in}(f_x, f_y) \tag{3.23}$$

so that

$$\mathcal{H}(f_x, f_y) = \frac{\iint_{\mathbb{R}^2} |h_{sys}(x, y)|^2 e^{-2\pi j(f_x x + f_y y)}\, dx\, dy}{\iint_{\mathbb{R}^2} |h_{sys}(x, y)|^2\, dx\, dy} \tag{3.24}$$

$$\mathcal{G}_{in}(f_x, f_y) = \frac{\iint_{\mathbb{R}^2} I_{in}(x, y) e^{-2\pi j(f_x x + f_y y)}\, dx\, dy}{\iint_{\mathbb{R}^2} I_{in}(x, y)\, dx\, dy} \tag{3.25}$$

$$\mathcal{G}_{out}(f_x, f_y) = \frac{\iint_{\mathbb{R}^2} I_{out}(x, y) e^{-2\pi j(f_x x + f_y y)}\, dx\, dy}{\iint_{\mathbb{R}^2} I_{out}(x, y)\, dx\, dy} \tag{3.26}$$

$\mathcal{H}(f_x, f_y)$ is an important quantity for the characterization of quality of an optical system, which is called *optical transfer function (OTF)* and specifies the response of the system in terms of spatial frequencies f_x, f_y, normalized to the zero-frequency term. Its modulus $|\mathcal{H}(f_x, f_y)|$ is called *modulation transfer function (MTF)*.

Remembering the Fourier-transforming relationship between the aperture transmission $T(\bar{r}_\perp)$ and the transfer function $h(\bar{r}_\perp, \bar{r}_\perp^{in})$ from section 3.2 as well as section 3.3 it is possible to write:

$$h(f_x, f_y) = c \cdot \mathcal{F}\{T(x, y)\}(f_x, f_y)$$

The application of Wiener-Khinchin (on the numerator) and Plancherel theorem (on the denominator) on Equation 3.24 results in:

$$
\begin{aligned}
\mathcal{H}(f_x, f_y) &= \frac{\iint_{\mathbb{R}^2} |h_{sys}(x, y)|^2 e^{-2\pi j(f_x x + f_y y)}\, dx\, dy}{\iint_{\mathbb{R}^2} |h_{sys}(x, y)|^2\, dx\, dy} \\
&= \frac{\iint_{\mathbb{R}^2} T(f_x', f_y') T^*(f_x' + f_x, f_y' + f_y)\, df_x'\, df_y'}{\iint_{\mathbb{R}^2} |T(f_x', f_y')|^2\, df_x'\, df_y'}
\end{aligned}
\tag{3.27}
$$

which is the autocorrelation of the point spread function relative to the system.

In case of simple systems with an exit pupil, the transmission function has a trivial form, as in Equation 1.19; in this case the autocorrelation is trivially proportional to the overlap between the aperture surfaces.

The normalized geometrical overlap area for a circular aperture can be expressed (Goodman [6], eq. 6-32) as:

$$\frac{A_{overl}}{A_{tot}} = \frac{2}{\pi} \left[\arccos u - u \sqrt{1 - u^2} \right]$$

with $u = \frac{r}{2R}$, r is the distance from two centers and R the circle radius.

The calculation is related to the diffraction-limited system by selecting its spatial cutoff frequency $f_{cutoff} = \frac{2R}{\lambda F}$, which corresponds to the zero point of the optical transfer function.

Aberrations worsen the quality of the output image, lowering the optical transfer function over a range of frequencies. It can be demostrated that that the modulation transfer function (MTF) in presence of aberrations is always suboptimal compared to the diffraction limited one.

Let the aperture transmission function be written by composing the aperture and the aberration contributions (Equation 1.22) together, $T_{ab}(\bar{r}_\perp) = T(\bar{r}_\perp) \cdot e^{jk\Phi(\bar{r}_\perp)}$); the OTF in this case can be
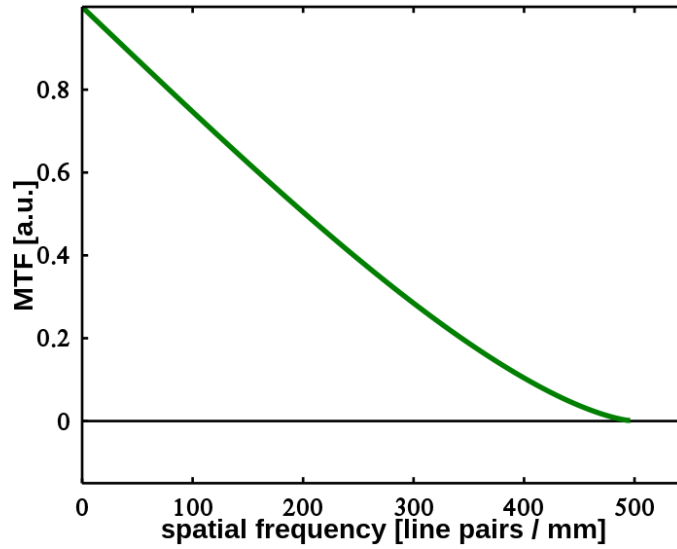
Figure 3.3: Modulation transfer function (MTF) of an ideal diffraction-limited system with a circular aperture.
Source: https://commons.wikimedia.org/wiki/File:1D_diffraction_limited_ optical_transfer_function..svg, media by Tom.vettenburg, CC BY-SA 3.0 License

written following Equation 3.27:

$$\mathcal{H}(f_x, f_y) = \frac{\iint_{\mathbb{R}^2} e^{jk\Phi(f_x', f_y')} u_{C_R}(f_x', f_y') \cdot e^{-jk\Phi(f_x'+f_x, f_y'+f_y)} u_{C_R}(f_x' + f_x, f_y' + f_y) \, df_x' df_y'}{\iint_{\mathbb{R}^2} u_{C_R}(f_x, f_y) df_x df_y}$$

$$= \frac{1}{a} \iint_{\text{overlap}(f_x, f_y)} e^{jk(\Phi(f_x', f_y') - \Phi(f_x'+f_x, f_y'+f_y))} \, df_x' df_y'$$

where overlap(f_x, f_y) indicates the overlap region between the two circular regions whose centers are separated by a vector (f_x, f_y).

Calculating MTF squared:

$$|\mathcal{H}(f_x, f_y)|^2 = \frac{1}{a^2} \left| \iint_{\text{overlap}(f_x, f_y)} e^{jk(\Phi(f_x', f_y') - \Phi(f_x'+f_x, f_y'+f_y))} \, df_x' df_y' \right|^2 \leq$$

with the use of Cauchy-Schwartz inequality:

$$\leq \left(\iint_{\text{overlap}(f_x, f_y)} \left| e^{jk(\Phi(f_x', f_y'))} \right|^2 \, df_x' df_y' \right) \cdot \left(\iint_{\text{overlap}(f_x, f_y)} \left| e^{-jk\Phi(f_x'+f_x, f_y'+f_y)} \right|^2 \, df_x' df_y' \right)$$

$$= \left(\iint_{\text{overlap}(f_x, f_y)} 1 \, df_x' df_y' \right)^2 = |\mathcal{H}_0(f_x, f_y)|^2$$

proves the optimality of MTF with no phase aberrations $\forall (f_x, f_y)$ which allow overlaps.

Chapter 4

Adaptive optics methods

As seen in the previous sections, the key to archive the maximum resolution in the image plane consists in shaping the wavefront of the incoming light in such a way that the root mean square (RMS) of the wavefront at the exit pupil is minimized; equivalently this means to minimize the extension of the PSF in the image plane of the system by removing the aberrations.

This can be done using a technology which can shape the light wavefronts on the optical path in a controllable way which takes the name of *adaptive optics (AO)*.

The first scientific application of the adaptive optics has been in the astronomy, where the most limiting disturbance comes from the atmospheric turbolence; the optical path of the observed objects is modified in a time-dependent way, resulting in a non-trivial image degradation. Adaptive optics methods has been applied in multiple astronomical experiments giving a relevant improvement in terms of angular resolution and detection signal [2, 17].

Adaptive optics methods has brought advantages in terms of improvement of the image contrast as well as image sharpness in a variety of microscopic configurations such as bright field, light-sheet, multi-photon [1, 14, 19], structured light microscopy [10], as well as opthalmologic instrumentation [22].

4.1   Tools and instrumentation

There are three classes of instruments that practically implement the adaptive optics methods:

- spatial light modulators (SLM): this technology uses layered liquid crystals which orientation allows to modify properties of the optical path like amplitude, phase and polarization by applying an external electric field. The control can be performed down to a single pixel, though their cross-talk make SLMs them less practical to operate with for the correction of aberrations; another disadvantage is the necessity to work with the light polarization, which results inconvenient when operating in microscopy (especially in fluorescence microscopy);

- deformable mirrors (DM): where the reflective surface is deformed using MEMS or piezoelectric actuators; there is a variety of deformable mirror designs that range from two mode tip-tilt mirrors, to a high number of actuators (typically around 100, up to 1000); high-performance actuators are able to handle more than 100 Zernike modes;

- deformable lenses (DL): are able to shape the wavefront transmissively; the deformation of the lens surface is practiced by using piezoelectric actuators resulting in the curvature of the glass
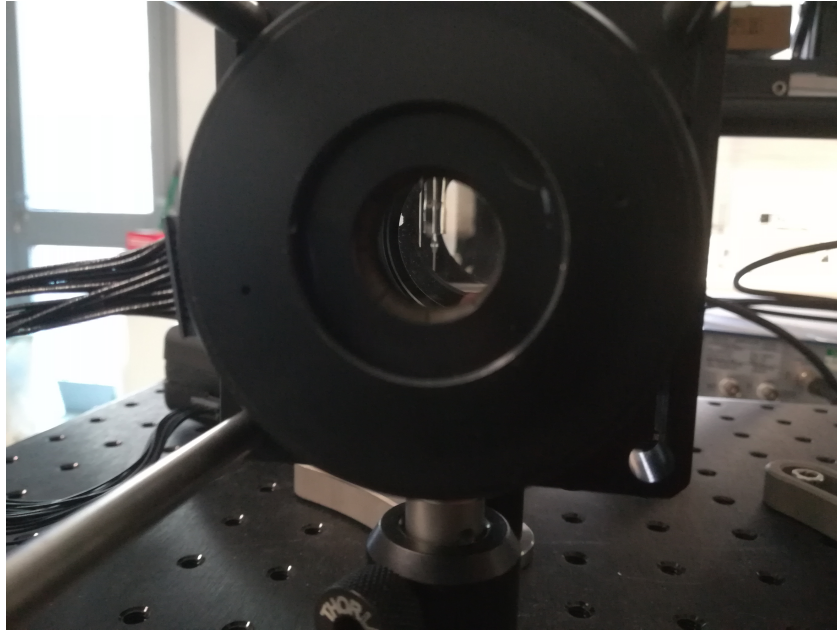
Figure 4.1: One of two deformable lenses used in this work ($16\,$mm diameter, 18 actuators)

surface; the medium between two glass surfaces adapts consequently; this effect produces a continuous optical path variation over the plane of the lens; currently lenses are able to correct Zernike modes up 4th order.

In this work two deformable lenses have been used. There are practical advantages for this choice for the microscopy setup: the transmissive action of lenses on the wavefront allows to correct aberrations without modifying the original optical path inside the optical setup; this allows an almost non-invasive method for the implementation of the adaptive optics framework as usually the modification of the already designed optical path is a difficult and delicate operation if performed on the complex commercial microscopes which can be impossible to realize in some cases.

4.2   Direct method

In order to perform the correction in the system that employs adaptive optics, the characterization of aberrations is required; this step is performed by instruments which measure and reconstruct the wavefront generated by a light source and are called *wavefront sensors*.

One of the most common types is the *Shack-Hartmann sensor*, which uses a wavefront coming from an almost collimated light beam; the wavefront travels along the optical axis and traverses an array of microlenses (*lenslet array*), which results in a partition of the wavefront; each partition is focalized by each lenslet on a sensor. It should be noticed the sensor is an intensity-detection type and doesn't use any kind of wavefront phase information.

The resulting spot centers allow to reconstruct the local gradient of the wavefront, as explained in the subsection 4.2.1 (Phase gradient reconstruction).

Once the wavefront is reconstructed it is sufficient to control the actuators of the adaptive optics element in such way that the detected wavefront aberrations are compensated. The real-time application of the corrections is also called closed-loop compensation. The method is fast as it requires a single measurement to completely characterize the aberrations of the system.
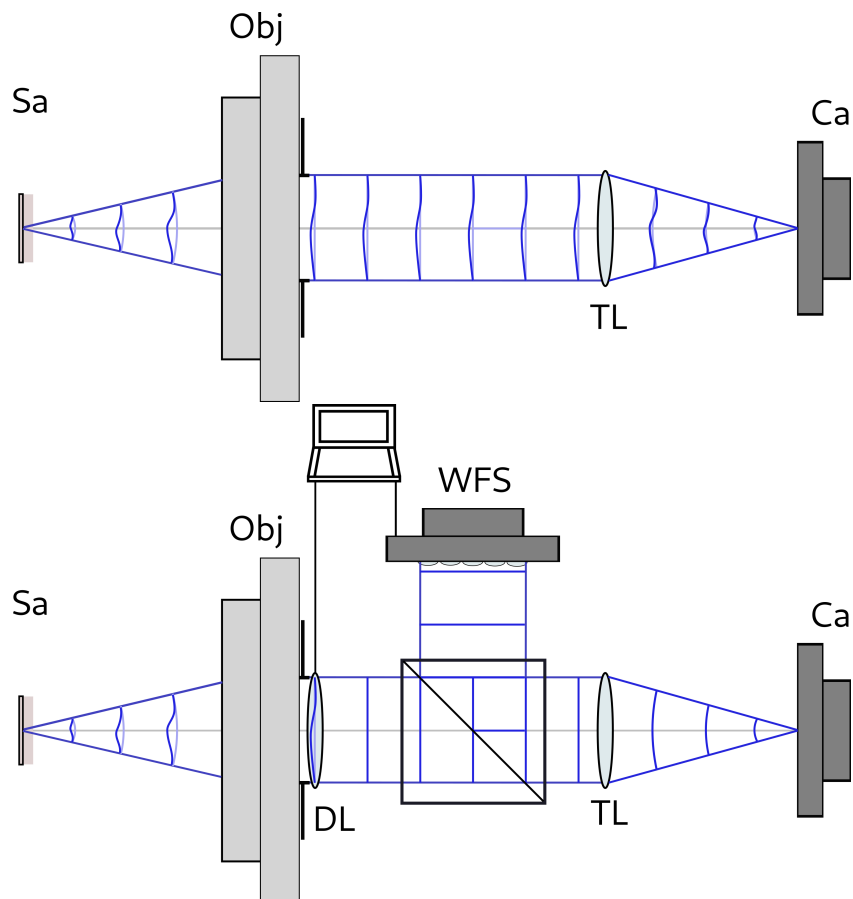
Figure 4.2: Simplified microscopy direct method setup;
in the direct microscopy case the spherical waves travel to the camera while retaining optical aberrations in the sample (Sa) stage, due to the intrinsic refractive characteristics of the sample (above);
the direct method uses the Shack-Hartmann wavefront sensor (WFS) to detect the aberrations; this information is used to drive an AO element (deformable lens, DL) to correct the wavefront and improve the quality of the resulting image in real-time (direct closed-loop method) (below).
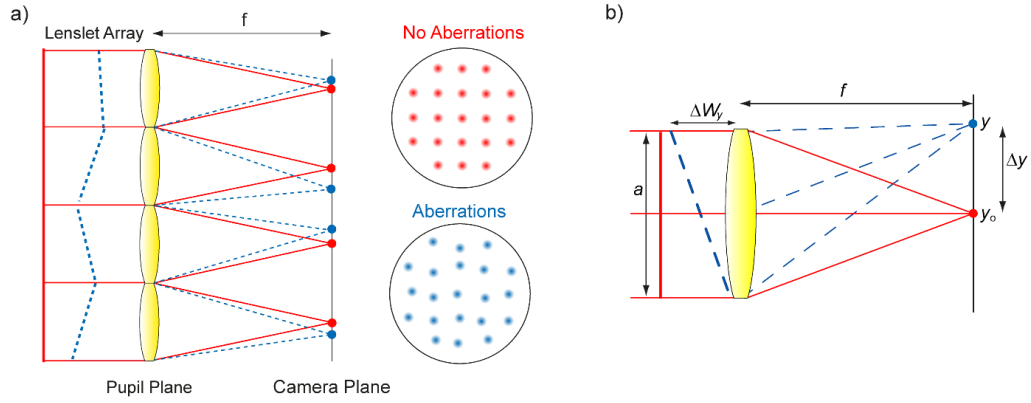
Figure 4.3: Shack-Hartmann wavefront sensor working principle illustration. a) the wavefront is partitioned by a lenslet array, then each wavefront region is collimated to an imaging sensor; by identifying each misplaced spot position it is possible to reconstruct the local wavefront gradient; b) schematic determination of the wavefront gradient given the spot displacement from the reference position.
Image source: `https://aomicroscopy.org/dm-calibration-direct-sensing`

A huge disadvantage of using a wavefront sensor is that the measurement of the spot position on the sensor relies on the assumption the source is a point-like generator of spherical light wavefronts; in the context of microscopy, where aberrations are due to sample-related refractive characteristics and positioning, the measurement of the wavefront and consequently of aberrations require an invasive intervention on the sample itself, by requiring the insertion of microscopic star-guides that necessitate of a additional preparation of the sample (which exposes the sample to a different chemical environment), which results impractical or impossible in some cases.

4.2.1   Phase gradient reconstruction

The actuators of the AO element are controlled via a control signal which is assumed to be voltage-proportional. The actuation causes deformation of the AO element surface and a consequent variation of the optical path of the light with a change of the phase on the optical plane; the variation of the phase is readily registered by the wavefront sensor.

By considering a quasi-collimated beam incidence on the wavefront sensor lenslet array area and using the ray optics description, the relationship $\tan \alpha = \frac{\Delta x}{f} \approx \alpha$ holds; α is the angle between the beam direction and the optical axis before the lens. Since the displacement on the lenslet area is much smaller than the focal distance ($\Delta x \ll f$) of lenslets, the paraxial approximation is used, describing the system with the transfer optics method; also the approximation $\tan \alpha \approx \alpha$ is justified for this reason. The system is a collimated beam at the angle α and a lenslet with the focal distance f.

The calculation involves the propagation of the beam for the distance $z = f$ after the lenslet, which, using the ABCD matrices formalism, results in:

$$\begin{bmatrix} \Delta x_f \\ \alpha_f \end{bmatrix} = \begin{bmatrix} 1 & z \\ 0 & 1 \end{bmatrix} \begin{bmatrix} 1 & 0 \\ -1/f & 1 \end{bmatrix} \begin{bmatrix} h \\ \alpha \end{bmatrix} \bigg|_{z=f} = \begin{bmatrix} h - z/f \cdot h + z\alpha \\ -h/f + \alpha \end{bmatrix} \bigg|_{z=f} = \begin{bmatrix} \alpha f \\ -h/f + \alpha \end{bmatrix}$$

$$= \begin{bmatrix} \Delta x \\ -h/f + \alpha \end{bmatrix} \tag{4.1}$$

From the equation results that the focalized beam has a displacement $\Delta x = \alpha f$, while its angle is α

(for $h \approx 0$, the beam passes through the center of the lenslet). This result can be directly related to the displacement of the optical path ΔW of the wavefront incident on the lenslet:

$$\Delta W(\bar{x}) = \bar{\alpha}\bar{x} = \frac{\Delta \bar{x}}{f}\bar{x}, \quad \Delta W = \frac{\Delta \phi}{k}$$

$$\Delta \phi(\bar{x}) = k\frac{\Delta \bar{x}}{f}\bar{x} \ \rightarrow \ \bar{\nabla}\phi(\bar{x}) = k\frac{\Delta \bar{x}}{f} \tag{4.2}$$

where $\bar{x}$ is the position displacement on the wavefront plane compared to the center of the whole Shack-Hartmann area; $\Delta \bar{x}$ is the position displacement of the focalized light spot inside the sensor area relative to a specific lenslet (selected by the vector $\bar{x}$); $\bar{\alpha} = \bar{x}/f$ for vector compatibility of the notation. $\bar{\nabla}\phi(\bar{x})$ is defined on the square with the side equal to the lenslet diameter, with $\bar{x} = \bar{0}$ on its center.

It is useful to define a *slope* $\bar{S}_i$ detected by each wavefront sensor lenslet i:

$$\bar{S}_i = \frac{\Delta \bar{x}_i}{f} = \begin{bmatrix} S_{i,x} \\ S_{i,y} \end{bmatrix} \tag{4.3}$$

which will be used as a set of coordinates in the adaptive optics element control description later.

The Equation 4.2 tells that the local phase gradient can be obtained by measuring the displacement of the focalized spot rispect to the center of the lenslet.

The spot position on the sensor can be found by evaluating the mean position using the intensity of each pixel as weight:

$$\begin{bmatrix} x_m \\ y_m \end{bmatrix} = \begin{bmatrix} (\sum_i x_i I_i)/(\sum_i I_i) \\ (\sum_i y_i I_i)/(\sum_i I_i) \end{bmatrix} \tag{4.4}$$

a threshold filter can be used to decrease the measurement noise and improve the centroid calculation.

4.2.2 Influence function and Zernike actuation matrices

In order to operate an adaptive optics element, it is necessary to establish a relation between a control space of coordinates $\bar{C}$ (voltage-like actuation space) and a signal space of coordinates $\bar{S}$ (AO element deformation space).

The dependence between these sets of coordinates is treated with a linearized model:

$$\bar{S}(\bar{C}) = \bar{S}(\bar{0}) + \frac{d\bar{S}}{d\bar{C}}(\bar{0}) \cdot \bar{C} + \dots$$

under assumption that the input signal in the current actuation space limits will not act "too strongly" on the system, so that the non-linear couplings can be discarded.

The matrix that relates input and output spaces is called *influence function matrix*:

$$IFS = \frac{d\bar{S}}{d\bar{C}}(\bar{0}) \tag{4.5}$$

In a more specialized context, where the signal is associated with the deformation on the AO element, the quantities of interest can be defined as follows:

$$\bar{S} = \begin{bmatrix} S_{0,x} & S_{1,x} & \dots & S_{0,y} & S_{1,y} & \dots \end{bmatrix}^T$$
$$\bar{C} = \begin{bmatrix} C_0, C_1, \dots \end{bmatrix}^T$$

where $S_{i,x/y}$ are slopes, as defined in Equation 4.3 and C_i are voltage or voltage-normalized quantities that control each actuator i.

The influence function matrix related to these quantities can be experimentally calculated by relying on the assumed linear nature of the system:

$$IFS = \begin{bmatrix} \frac{S_{0,x}^{+C}-S_{0,x}^{-C}}{2C} & \frac{S_{0,x}^{+C}-S_{0,x}^{-C}}{2C} & \cdots \\ \frac{S_{1,x}^{+C}-S_{1,x}^{-C}}{2C} & \frac{S_{1,x}^{+C}-S_{1,x}^{-C}}{2C} & \cdots \\ \cdots & \cdots & \end{bmatrix}$$

the quanties $+S_{i,x/y}^{\pm C}$ correspond to slopes at maximum / minimum actuation voltages $\pm C$ for each actuator, which approximate well the derivative between the input and output spaces over the whole range of control of the i-th actuator.

The resulting control of the system can be written in the matrix form, ignoring the constant zero-voltage term:

$$\bar{S} = IFS \cdot \bar{C}$$

Another useful representation maps the actuator voltage space $\bar{C}$ to the physical deformation AO element deformation, seen in Zernike mode representation using a wavefront sensor. The wavefront measured by the Shack-Hartmann sensor is decomposed in Zernike modes (truncated up to a certain mode) $\Phi(x,y) = \sum_{q=0}^{Q} a_q Z_q(x,y)$; its representation can be related to the slopes seen by each lenslet of the sensor as:

$$\bar{a} = Z^{-1}\bar{S}, \quad Z = \begin{bmatrix} \frac{\partial Z_0(x_1,y_1)}{\partial x} & \frac{\partial Z_1(x_1,y_1)}{\partial x} & \cdots \\ \frac{\partial Z_0(x_2,y_2)}{\partial x} & \frac{\partial Z_1(x_2,y_2)}{\partial x} & \cdots \\ \cdots & \cdots & \end{bmatrix}, \quad \bar{a} = \begin{bmatrix} a_0 \\ a_1 \\ \cdots \end{bmatrix} \tag{4.6}$$

by always retaining to assumption of the linear behaviour of the system under the actuation variables.

The relation

$$\bar{a} = IFZ \cdot \bar{C} = (Z^{-1})(IFS) \cdot \bar{C} \tag{4.7}$$

consequently holds; Z^{-1} is calculated as a Moore-Penrose pseudoinverse matrix.

With this description it is possible to control any AO device while obtaining a device-independent representation of the effects on the wavefront optical path.

The IFZ matrix is decomposed by means of singular value decomposition (SVD) and gives the representation of orthogonal modes in sensor space (U) coupled to the orthogonal modes of the actuation space (V) through the diagonal matrix of singular values (D):

$$(IFZ) = UDV^T$$

this representation conveniently encodes the effects of the AO element coupling on each mode via the singular values matrix D; also the calculation of the inverse becomes a trivial operation:

$$(IFZ)^{-1} = VD^{-1}U^T$$

4.3 Indirect method

In absence of a wavefront sensor, the direct estimation of aberrations induced in an optical system is a difficult problem in the context of microscopy: given a general image, isolated point-like structures are rare, which makes it hard to identify reference points to operate with; the analysis of the extended objects makes the wavefront sensing hard in a general sense; Fourier analysis of images is difficult due to unknown optimal experimental conditions of the setup to reference with, as well as the noise presence.

In order to overcome limitations of the direct method, another type of aberration correction approach is employed. The core idea is to use a detection-compensation feedback loop that directly works on the experimental image in real-time; an exploration algorithm selects the actuators configuration of the AO element which seeks to improve the image quality at each step, after measuring the effect on the image quality for each variation.

Since the identification of aberration modes is not measured, but rather deduced using a feedback system, it is called *indirect method*.

The main concepts that allow the accomplishment of the method are:

- the AO element control system;

- the image quality function;

- the algorithm that controls the actuators and decides how to set them to increase the image quality function value.

Both the image quality function and the algorithms should be general enough to operate under a wide class of experimental conditions; an especially important criterion is that they should be independent from the type and the position of the sample and make the system converge towards a maximally unaberrated image.

4.3.1 AO device control

As seen in subsection 4.2.2 (Influence function and Zernike actuation matrices), the set of voltage-proportional coordinates (as control coordinates) and the set of Zernike modes that influence the phase of the incoming light wavefront (sensor coordinates) are a good choice for a control coordinates of the AO device.

The is archived by introducing by a procedure that populates the Influence function matrix (Zernike modes version) IFZ by performing the calibration of the AO device, with aid of a Shack-Hartmann sensor.

A more detailed explanation of the calibration procedure will be given in the section 5.2 of experimental part of this work.

This procedure allows, in experimental conditions, to find Zernike orthonormal modes generated by the device by keeping into account its constructive limitations (*mirror modes*), which will be reflected on the reconstruction on higher modes; in this sense, the number of actuators involved in the AO device deformation will always produce a lower number to reliably usable Zernike modes; this can occur due to a non-full orthogonality of the generated modes, due to non-linearities non included in the model, as well as the limitations due the suboptimal calibration procedure (for example: non-optimal source collimation, non-pointlike source, increased noise).

4.3.2   Image metric function

Informations about to aberrations are induced over the real-time collected images.

Due to the Fourier transforming (convolutional) action of aberrations in the pupil of the system, sharper (in same experimental cases also brighter) images indicate the optical system has accumulated minor aberrations. Ideally, the features of the image are diffraction-limited.

This characteristic is used to establish a metric in the space of possible images of the experiment; increasingly better values along the metrics translate into increasingly better images until the best correction of the aberrations.

This can be done by relating the images to the control space of Zernike mode coefficients (see subsection 4.2.2 (Influence function and Zernike actuation matrices)). The modification of the current control variables is directly reflected by the modification of the sample image; the sample itself should mantain static experimental conditions in time: for example the illumination should be statically mantained, the sample position shouldn't vary, internal parts should be static during the indirect sensing procedure.

The metric is a *(metric) function* that maps the space of images, restricted to the control space of the AO device, to a real number.

There isn't a single optimal choice for the metric function, but it is required to be general enough for a variety of experimental conditions (for example: independence from the sample type or its position in the experiment).

Examples of possible metric functions are presented below:

- Total intensity of the image:

$$f_m = \sum_{xy} I_{xy}$$

- Total intensity squared of the image:

$$f_m = \sum_{xy} I_{xy}^2$$

- Variance of the image:

$$f_m = \sqrt{\frac{1}{N} \sum_{xy} (I_{xy} - I_{mean})^2}$$

   with N is number of pixels xy of the image.

- More sophisticated metrics can be used [3, 4, 20].

In case of a bright-field microscopy experiment metric functions that optimize the sharpness of the image (like the variance of the image) are prefered; fluorescence microscopy experiments mostly benefit from functions related to the collected signal (like the total intensity or total intensity squared).

4.3.3 Convergence algorithm

A procedure that selects the optimal configuration in the control space of the given AO device is the algorithm of the sensorless method.

Usually mathematical assumptions are done through a model-based approach, which gives a form to the metric function within the actuation space.

In this work two possible approaches are considered: the quadratic model algorithm and a more sophisticated DONE algorithm.

Quadratic model optimization

One of the simplest approaches is to assume a quadratic model of the metric function over the space of the control variables [4].

By considering f the value of the metric function:

$$f \approx f_0 - \sum_{i,j} \alpha_{ij} x_i x_j = f_0 - \bar{x}^T M \bar{x} \tag{4.8}$$

where f_0 is the metric function value in presence of zero aberrations and $\bar{x}$ is the space of control space variables; here A is a semi-definite positive matrix, since the $\bar{x}^T M \bar{x} > 0$ for $\forall \bar{x} \neq \bar{0}$.

An optimal $M' = U^T M U$ (U unitary) matrix allows to write Equation 4.8 using a diagonalized set of coordinates, $\bar{x}' = U^T \bar{x}$:

$$f \approx f_0 - \sum_{i} \alpha_i' x_i'^2 \tag{4.9}$$

This optimal condition is approximated using an orthogonal set of Zernike polynomial modes over the control space; in particular, the assumption the maximum of the metric function coincides with the zero-aberrations configurations state in the control space is acting.

At this point, each mode can be treated independently; the estimation of the maximum for each mode can be performed by fitting values of the metric function with two, three or more points (respectively called $2N + 1$, $3N$ or kN algorithms) and identifying the maximum of the given parabola; the imperfect parabolic fit can be improved by iterating the algorithm at cost of speed.

DONE algorithm

DONE is a model-based algorithm, formulated by Verstraete [23], that takes its origin from the kernel machine formulation used in machine learning [15].

Specifically, the algorithm has been implemented in the context of measurements being expensive to obtain, noisy and a priori non-specified number; the cost of the measurements is an important limitation as it makes the computation of the derivatives numerically-intractable and consequently denying the usage of the Newton-like methods to solve the minimization problem.

The main idea of the algorithm is to construct a model function that approximates the unknown metric function while collecting new measurements; the algorithm integrates new measurements while preseving the previous ones, this while trying to be fast.
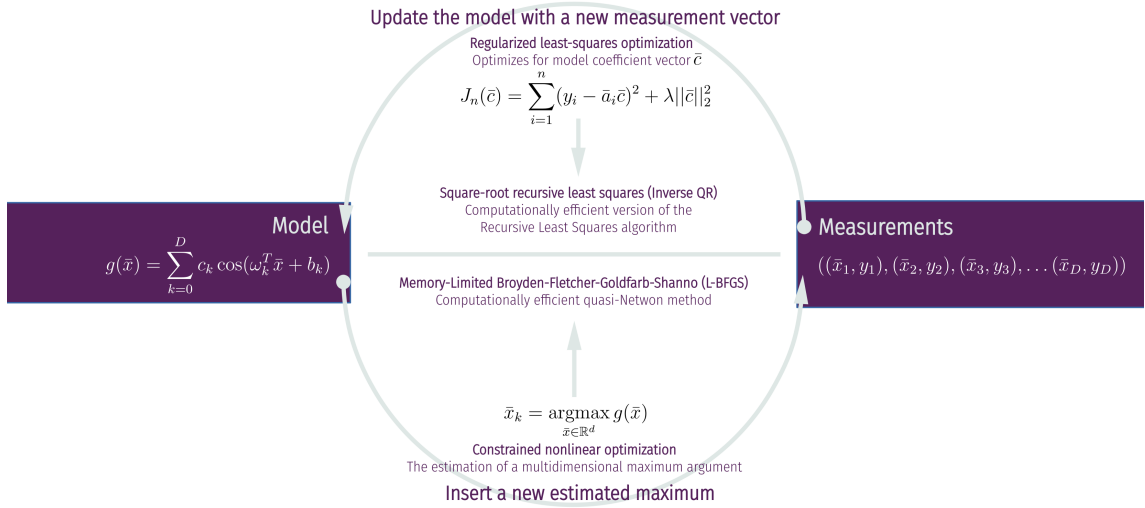
Figure 4.4: Schematic DONE algorithm loop

- the measurement data

$$((\bar{x}_1, y_1), (\bar{x}_2, y_2), \dots)$$

is a list made of the control space states $\bar{x}_i$ and the metric function value relative to that state $\bar{y}_i$;

- the model constructed by DONE algorithm

$$g(\bar{x}) = \sum_{k=1}^{D} c_k \cos(\omega_k^T \bar{x} + b_k)$$

is a sum of cosines with randomly initialized frequencies ω_k and phases b_k; in particular $\omega = (\omega_1, \omega_2, \dots)$ is an $N \times D$ matrix (N is the dimension of the input space, while D the number of cosines expansion terms) with random generated terms taken from the algorithm-specified random distribution; $b = (b_1, b_2, \dots)$ is a $1 \times D$ vector, where b_k is initialized with scalar values from a uniform random $\mathbb{U}_{[0,2\pi)}(x)$ distribution.

- the model update part with a new measurement is based on the solution of the Tikhonov regularized least squares problem

$$J_n(\bar{c}) = \sum_{i=1}^{n} (y_i - \bar{a}_i \bar{c})^2 + \lambda ||\bar{c}||_2^2 \tag{4.10}$$

with $\bar{a}_n = [\cos(\omega_1^T \bar{x}_n + b_1), \cos(\omega_2^T \bar{x}_n + b_2), \dots, \cos(\omega_D^T \bar{x}_n + b_D)]$; the solution with n available measurements is $\bar{c}_n = \text{argmax}_{\bar{x} \in \mathbb{R}^d} J_n(\bar{c})$, which corresponds to the list of the optimal model coefficients, is found; the regularization of least squares prevents the overfitting as well stability problems of the solution.

The author proposes to use the square-root Recursive Least Squares algorithm (based on Inverse QR algorithm); an efficient numerical version of the recursive least-squares (Verstraete

[23], section 4.3.1) is reported below:

$$\gamma_n = 1/(1 + \bar{a}_n P_{n-1} \bar{a}_n^T)$$
$$\bar{g}_n = \gamma_n P_{n-1} \bar{a}_n^T$$
$$\bar{c}_n = \bar{c}_{n-1} + \bar{g}_n (y_n - \bar{a}_n \bar{c}_{n-1})$$
$$P_n = P_{n-1} - \bar{g}_n \bar{g}_n^T / \gamma_n$$

with $\bar{c}_0 = \bar{0}, P_0 = \lambda^{-1} \mathbb{I}_{d \times d}$.

The author uses a numerically stable square-root version of the algorithm which finds a rotation matrix Θ_n so that the left-hand side upper-triangular matrix is lower-triangularized:

$$\begin{bmatrix} 1 & \bar{a}_n P_{n-1}^{1/2} \\ 0 & P_{n-1}^{1/2} \end{bmatrix} \Theta_n = \begin{bmatrix} \gamma_n^{-1/2} & 0 \\ \bar{g}_n \gamma_n^{-1/2} & P_n^{1/2} \end{bmatrix}$$

- the measurement update part employs the memory-limited version of Broyden–Fletcher–Goldfarb–Shanno (BFGS) algorithm; this is a quasi-Netwon algorithm that solves the nonlinear multidimensional maximum seeking problem

$$\bar{x}_k = \operatorname*{argmax}_{\bar{x} \in \mathbb{R}^d} g(\bar{x}) \tag{4.11}$$

while keeping under control both time and memory constraints with the growth of dimension d.

The Newton algorithm in a multidimensional space solves the minimum seeking problem with a quadratic rate of convergence:

$$\bar{x}_{n+1} = \bar{x}_n + (H_n g_n)^{-1} \nabla g_n$$

where $H_n = \begin{bmatrix} \partial_{x_1,x_1} & \partial_{x_1,x_2} & \ldots \\ \partial_{x_2,x_1} & \partial_{x_2,x_2} & \ldots \\ \ldots & \ldots & \ldots \end{bmatrix}$ is the Hessian matrix over the control space variables. The issue with this approach is the necessity to update and store the Hessian matrix H_n which scales as $O(d^2)$ in memory, which is going to be inverted with an $O(d^3)$ cost in time; for a growing number of dimensions d this approach becomes intractable soon.

A less costly method relies on the method by Davidson, Fletcher, Powell (DFP) that constructs a pseudo-Hessian matrix based on the quadratic model of the objective function g. Given the estimated the point f_k, its gradient $\bar{\nabla}_{\bar{x}} f_k = g_k$ and the estimate H_k, its possible to find the direction to approach to minimum $p_k = H_k^{-1} g_k$ with a correct step for the converge (Wolfe conditions) $x_{k+1} = x_k + \alpha_k p_k$; once this done, it is possible to set the secant equation $H_{k+1} s_k = y_k$, where $s_k = x_{k+1} - x_k$; the remaining degrees of freedom on H_{k+1} are locked by imposing the symmetry and the positive definiteness (this condition can be equivalently can be written as $s_k^T y_k > 0$) as well as by minimizing the distance from the current iterate of the matrix (via weighted Froebenius norm in the matrix space), so:

$$\min_{H_{k+1}} ||H_{k+1} - H_k||$$
$$H_{k+1} = H_{k+1}^T, \ H_{k+1} s_k = y_k$$

which results in:

$$H_{k+1} = \left(\mathbb{1} - \frac{y_k s_k^T}{y_k^T s_k}\right) H_k \left(\mathbb{1} - \frac{s_k y_k^T}{y_k^T s_k}\right) + \frac{y_k y_k^T}{y_k^T s_k}$$

To avoid dealing with the inversion as an extra computational step, it is possible to directly minimize the distance between successive iterates of the inverse matrix $J_k = H_k^{-1}$ by setting $\min_{J_{k+1}} ||J_{k+1} - J_k||$, $\quad J_{k+1} = J_{k+1}^T$, $\quad J_{k+1} y_k = s_k$ which gives the solution the dual solution in variables s_k, y_k of the previous version:

$$J_{k+1} = \left(\mathbb{1} - \frac{s_k y_k^T}{s_k^T y_k}\right) J_k \left(\mathbb{1} - \frac{y_k s_k^T}{s_k^T y_k}\right) + \frac{s_k s_k^T}{s_k^T y_k}$$

The memory-limited version makes another step and doesn't store the matrix J_k for the computation at all, the minimization step is performed using the history vector of iterates $(\{s_{n-l}, s_{n-l+1}, ..., s_n\}, \{y_{n-l}, y_{n-l+1}, ..., y_n\})$ [11].

- the DONE algorithm makes use of hyperparameters that need to be tuned for the specific domain of operations [23]

    - The optimal probability distribution $p_\Omega(\omega)$ used to set the frequencies of cosine features can be calculated by minimizing the variance of the estimator $\tilde{G}(x) = \sum_{k=1}^{D} \tilde{C}_k e^{j\bar{\Omega}_k^T \bar{x} + B_k}$ such that $\tilde{G}(\bar{x})$ is unbiased estimator of $f(\bar{x})$: $f(\bar{x}) = E[\tilde{G}(x)]$ (Ω_k is an i.i.d. variable), with $f(\bar{x})$ is the ideal model function on the measurements written as sum of indefinite cosine features: $f(\bar{x}) = \sum_{k=1}^{\infty} c(\omega_k, b_k) \cos(\omega_k^T \bar{x} + b_k)$. So, the unbiasedness is satisfied by requiring:

$$\tilde{C}_k = \frac{\tilde{f}(\bar{\Omega}_k) e^{-jB_k}}{D(2\pi)^d \tilde{p}_\Omega(\bar{\Omega}_k)}$$

    setting $p_\Omega(\omega) = |\hat{f}(\bar{\omega})| / \int_{\mathbb{R}^d} |\hat{f}(\bar{\omega}')| \, d\bar{\omega}'$ which minimized the variance of the estimator.

    Experimentally, the problem lies in the fact $\hat{f}(\bar{\omega})$ is unknown in most situations; the choice of the distribution has conquently to be guessed, estimated theoretically or be tuned by hand by running tests that approximate the experiment. The author suggests to guess $p_\Omega(\omega)$ as $p_\Omega(\omega) = \mathcal{N}(0, \sigma^2 \mathbb{1}_{d\times d})$, by selecting the appropriate variance σ^2 so that it fairly approximates $p_\Omega(\omega) = |\hat{f}(\bar{\omega})| / \int_{\mathbb{R}^d} |\hat{f}(\bar{\omega}')| \, d\bar{\omega}'$.

    - λ is the parameter that sets the Tikhonov regularization part in the model update procedure. The maximum λ for which the convergence of the least-squares $J_N(\bar{c}) = ||\bar{y}_N - A_N \bar{c}||_2^2 + \lambda ||\bar{c}||_2^2$, $\quad \bar{c} = \text{argmin}_{\bar{c}} J_N(\bar{c})$ is guaranteed by satisfying the condition (Verstraete [23], sec. 4.5):

$$||(A_N^T A_N + N\lambda \mathbb{1}_{D\times D})^{-1} A_N^T y_N||^2 = M^2$$

    where the optimal $M = M_a$ is given by

$$\frac{\sqrt{2}}{(2\pi)^d \sqrt{D}} \int |\hat{f}(\omega)| \, d\omega = M_a$$

- the number of random features D improves the approximation of the model function by decreasing the distance Q_n between the true function measurements y_n and its estimates via random features:

$$Q_n(\bar{c}) = \frac{1}{N} \sum_{n=1}^{N} \left(y_i - \sum_{k=1}^{D} c_k \cos(\bar{\omega}_k^T \bar{x}_n + b_k) \right)^2 \qquad (4.12)$$

  the use of more features results in a less computationally efficient, but better fitting algorithm over an increasing number of measurements.

- the solution of the model minimization step is followed by a random Gaussian pertubation of the solution itself, in order to avoid getting stuck in the local minimum of the estimated model function; the same procedure is done for the measurements before the estimation of the model function. The amplitude of the perturbation is a hyperparameter that can be tuned, to tradeoff between the speed of the convergence of the minimum and the exploration possibilities of the algorithm.

4.4 Multi-coniugated adaptive optics
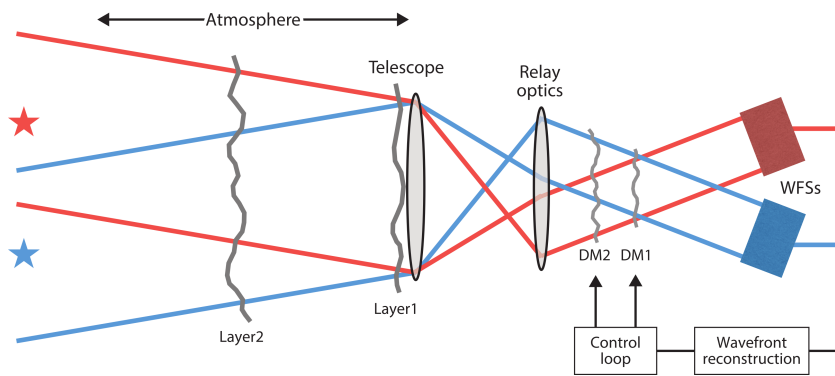
Figure 4.5: An example of MCAO configuration used in astronomy; the AO device positioned in the pupil plane of the system (DM1) corrects common path aberrations, while the more extended (DM2) AO device provides the correction over the wide field of view.
Source: Rigaut et al. (2018), figure 3 [18]

While the adaptive optics methods are able to minimize aberrations around a specific point in the image, it is desirable to be able to correct aberrations over a wide region of the resulting image.

The adaptive optics technique that allows this type of improvement, already successfully employed in the field of astronomy [17], is the Multi-conjugated Adaptive Optics (MCAO) correction; the technique makes use of multiple AO devices, which, with a proper positioning and control allow to correct over an extended region.

A typical astronomical MCAO configuration uses two AO elements. The first AO device is placed in the pupil plane of the system to correct the aberrations over in common path of all points of the field of view (FOV). The second AO device is able to correct the aberrations over different FOV points; independent FOV region rays pass through different portions of the AO device, allowing the modification of the optical path over an extended region of the FOV; consequently a different degrees of aberrations can be compensated on different regions of the resulting image. Two wavefront sensors are referencing two separate guide stars, which correspond to different points the field of

view; using the real-time direct sensing method and the continuity of aberrations over the field of view the resulting wide-field aberration correction is improved.

The MCAO procedure doesn't change in case of the indirect method in the context of microscopy; the wavefront sensor aberrations correction is replaced by the optimization of the metric function over the image where the control space involves two independent sets of variables.

Part II

Experimental activity

Chapter 5

Experimental setup

5.1 Experimental setup

5.1.1 Setup description

The setup uses a three-dimensional micrometric translational stage (Thorlabs PT3, XYZ Translation Stage, $25\,\text{mm}$) which holds a kinematic mount as a tip-tilt stage (Thorlabs VM1/M, Kinematic Mirror Mount); the sample itself is placed on tip-tilt stage. These parts allow to control the translation of the sample with an error of $\Delta x \lessgtr 10\,\text{µm}$ over an x-range of $25\,\text{mm}$; same considerations hold for y and z axes; the x-axis stage can also act as an independent sample defocuser.

The entire sample can be tip / tilted up to a $\Delta\theta = 80\,\text{µrad}$ angle with a range of $\approx 110\,\text{mrad}$ ($\approx 6.2°$), which corresponds to a rotation of about 27 turns of the stage knob. The role of the tip-tilt stage in the system is to allow a controllable introduction of low-order aberrations over a wide-field in the sample ($F.O.V. = 1.134\,\text{mm} \times 0.713\,\text{mm}$). The use of the tip-tilt stage also introduces a significant translation of the field of view. As result the comparison of aberrations is less reliable, as the features in the image change. The translation stage is used to compensate this effect.

An illuminator built using a blue LED ($\lambda = 480\,\text{nm}$), a diffusive filter and a collimating lens is used to generate a uniform light source.

The setup uses a Mitutoyo M Plan APO objective ($10\times$, $NA = 0.28$, $WD = 34\,\text{mm}$, $f = 20\,\text{mm}$). A custom-made adaptive optics deformable lens ($d = 10\,\text{mm}$) is placed in the objective back-aperture and acts as the pupil of the system. A second deformable lens ($d = 16\,\text{mm}$) is placed at a distance of ($\rho = (210 \pm 2)\,\text{mm}$) from the first lens; the wavefront outgoing from the second deformable lens is focused using a tube lens ($f = 165\,\text{mm}$) mounted immediately after.

A CMOS camera (IDS UI306xCP-M) with a sensing surface of $S = 11.345\,\text{mm} \times 7.126\,\text{mm}$ and a pixel size of $5.86\,\text{µm}$ is used for the experiment.

The setup allows to remove the translation block with the illuminator and to interchange them with a laser source for alignment and testing.

5.1.2 Estimation of the non-pupil lens position for widefield setup

In order to make use of full capabilities of the widefield correction, an optimal position of the non-pupil deformable lens is estimated. If the lens is too close to the objective, the lens surface is not fully used and the correction results limited by maximum deformation capabilities of the lens;
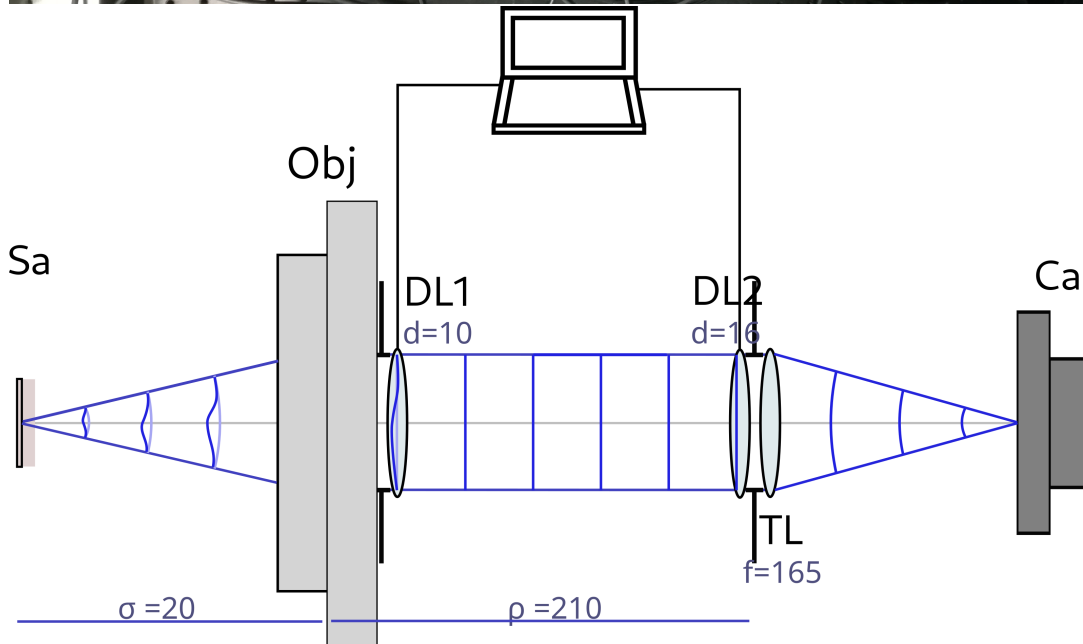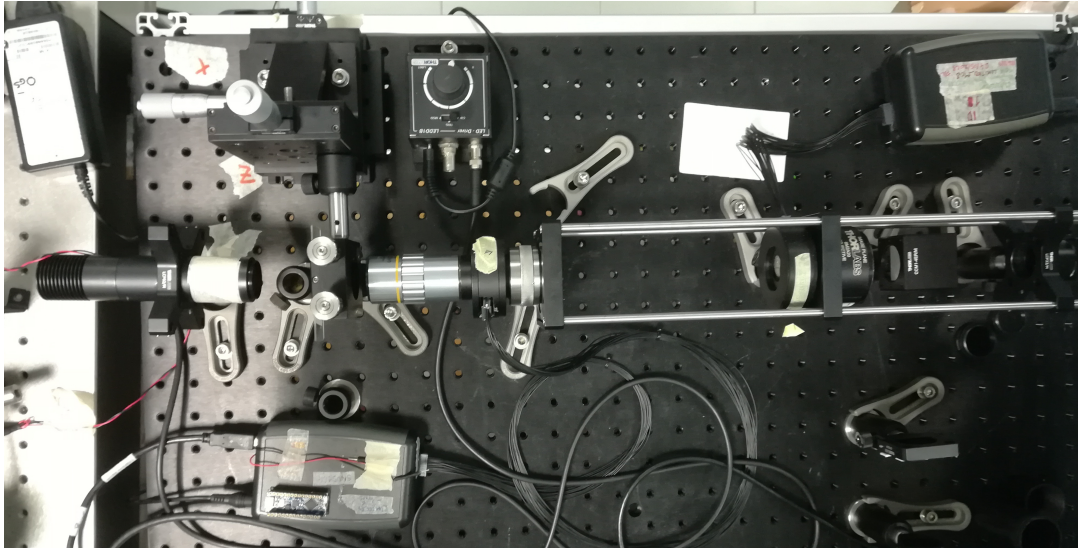
Figure 5.1: Experimental adaptive optics setup; photography of the setup (above) and a briefly described schematics (below).

viceversa, in case the lens is too far then not all rays coming from the widefield regions of the sample reach the camera due to the finite diameter of the deformable lens; the effective field of view is cut.

The estimation is done using the ray transfer matrix formalism; this method allows to calculate the position and the angle respect to the optical axis, assuming the cilindrical symmetry of the system and the paraxial approximation of the light propagation (aberrations are ignored). A system can described as a real 2×2 matrix that tells the position x_f and the exit angle respect to the optical axis θ_f of a geometrical optical ray, given the initial position x_i and angle θ_i:

$$\begin{bmatrix} x_f \\ \theta_f \end{bmatrix} = \begin{bmatrix} A & B \\ C & D \end{bmatrix} \begin{bmatrix} x_i \\ \theta_i \end{bmatrix}$$

The calculation uses the matrix representation of the translation of the ray after a distance z, T_z,
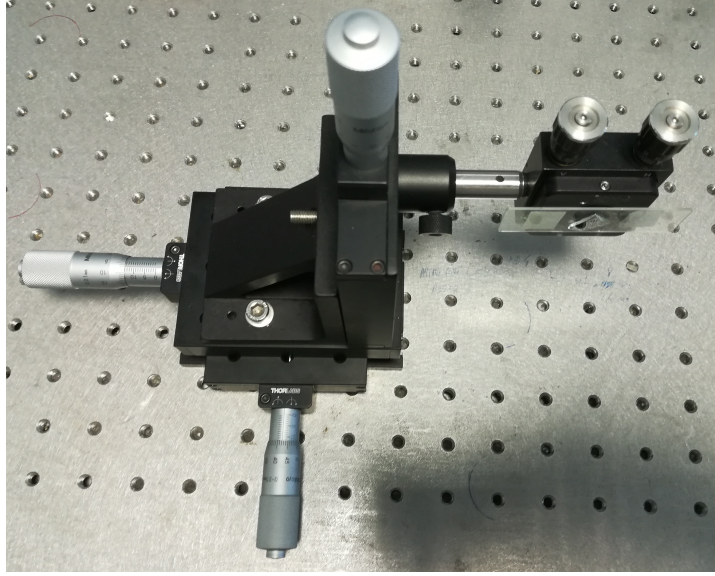
Figure 5.2: Translational stage, tip / tilt stage and the sample.

and the effect after a thin lens with a focal length f, L_f:

$$T_z = \begin{bmatrix} 1 & z \\ 0 & 1 \end{bmatrix}, \quad L_f = \begin{bmatrix} 1 & 0 \\ -1/f & 1 \end{bmatrix}$$

The full system can be described by the transfer image-forming matrix M:

$$M = T_\zeta L_{Mf_1} T_\rho L_{f_1} T_\sigma = \begin{bmatrix} M_A & 0 \\ M_C & M_D \end{bmatrix}$$

where L_{f_1} describes is the net focal distance of the objective lens system, L_{Mf_1} is focal length of the tube lens and σ, ρ, ζ are respectively sample-objective, objective-tube lens, tube lens-camera distancies.

In order to obtain conditions on the non-pupil adaptive optics lens position, the propagation is considered up to the tube lens (M_P matrix), which position coincides with the AO lens:

$$\begin{bmatrix} x_f \\ \theta_f \end{bmatrix} = M_P \begin{bmatrix} x_i \\ \theta_i \end{bmatrix} = T_\rho L_{f_1} T_\sigma \begin{bmatrix} x_i \\ \theta_i \end{bmatrix}$$

$$= \begin{bmatrix} 1 & \rho \\ 0 & 1 \end{bmatrix} \begin{bmatrix} 1 & 0 \\ -1/f & 1 \end{bmatrix} \begin{bmatrix} 1 & \sigma \\ 0 & 1 \end{bmatrix} \begin{bmatrix} x_i \\ \theta_i \end{bmatrix}$$

$$= \begin{bmatrix} 1 - \rho/f & \sigma - \frac{\sigma\rho}{f} + \rho \\ -1/f & -\frac{\sigma}{f} + 1 \end{bmatrix} \begin{bmatrix} x_i \\ \theta_i \end{bmatrix}$$

The maximum displacement from the optical axis on the non-pupil lens plane is fixed by the diameter of the non-pupil AO lens ($x_f = 8\,\text{mm}$). The angular relation $\theta_i = \frac{r_1 - x_i}{\sigma}$ determines the maximum allowed angle in the widefield configuration ($r_1 = 5\,\text{mm}$, the diameter of the pupil). The equation with x_f term is solved to obtain:

$$\frac{\rho}{f} = \frac{r_1 - x_f}{\frac{r_1 + x_i}{\sigma} f - r_1}, \quad \text{using } \sigma = f$$

$$\rho = \frac{r_1 - x_f}{x_i} f = \frac{-3\,\text{mm}}{-0.37\,\text{mm}} \cdot 20\,\text{mm} = 160\,\text{mm}$$

In the experimental configuration the non-pupil lens is set at the distance $\rho = 210$ mm, which is suboptimal; one of reasons to perform this change is to balance the vignetting of the background illumination.

5.1.3   Setup construction and alignment steps

We proceed with the construction and the alignment of the optical setup needed for testing of the adaptive optics framework for the widefield correction.

The alignment procedure is done using a laser diode ($\lambda = 640$ nm). A cage design has been used for the aligment of the objective, the tube lens, two deformable lenses and the imaging camera. Other parts are positioned independently.

The laser beam is sent into the objective with the deformable lens attached on its back aperture. The collimation of the exiting beam is required and is checked using a shearing interferometer; it is done by moving the laser position along the optical axis until the figure on the interferometer indicates the collimation. A second lens is put in place while the laser is projected through it. A beamsplitter is positioned to send the laser beam on the second path. This setup is constructed to verify the height of the beam and to assure it remains constant over long distances; a beamsplitter is put to separate the optical paths and use the reflection path to pointpoint the focalization position of the laser, which is useful to know in case of adjustments of the setup; the point is determined with the use of an iris.

The alignment of the beam through the second deformable lens is critical for the correction in widefield and is done carefully. On the other hand the alignment of the first deformable lens is easier because of the possibility to adjust of position of the sample because of a much minor sensibility to the translation of a laser respect to the optical plane.

Once both laser and second deformable lens match the laser position at the iris, the alignment of lenses is completed.

At this point the CMOS camera is moved until the laser spot is focalized on it. In particular, since small aberrations are present due to two deformable lenses, the region of least confusion is chosen as the best image plane estimate.

5.2   Calibration of deformable lenses

The calibration procedure is required in order to associate the input voltages used to move each deformable lens actuator with the Zernike coefficients that are used as control space coordinates. For this goal, we construct and align the calibration setup; then, use an already prepared software to calibrate and obtain necessary data for the experimental activity.

The setup comprises a diode laser ($\lambda = 640$ nm), a telescope system of three lenses and a wavefront sensor (Shack-Hartmann type); a mounting cage has been used to maintain the setup alignment along the optical axis.

As first step the laser source is set along the optical axis; a lens ($f = 150$ mm) is subsequently placed in order to produce collimated beam, which is verified using a shearing interferometer; the mounting point for the adaptive lens is placed subsequently. The wavefront sensor cannot be used at this point due to a large diameter of the beam compared to the wavefront sensor diameter; in this case a relay $f_1 + f_2$ configuration has been used with the entrance lens of $f_1 = 200$ mm and an $f_2 = 60$ mm, with the resulting beam magnification factor of $M = \frac{3}{10}$. The position of the last lens has been adjusted by positioning the wavefront sensor as the next element and by measuring the
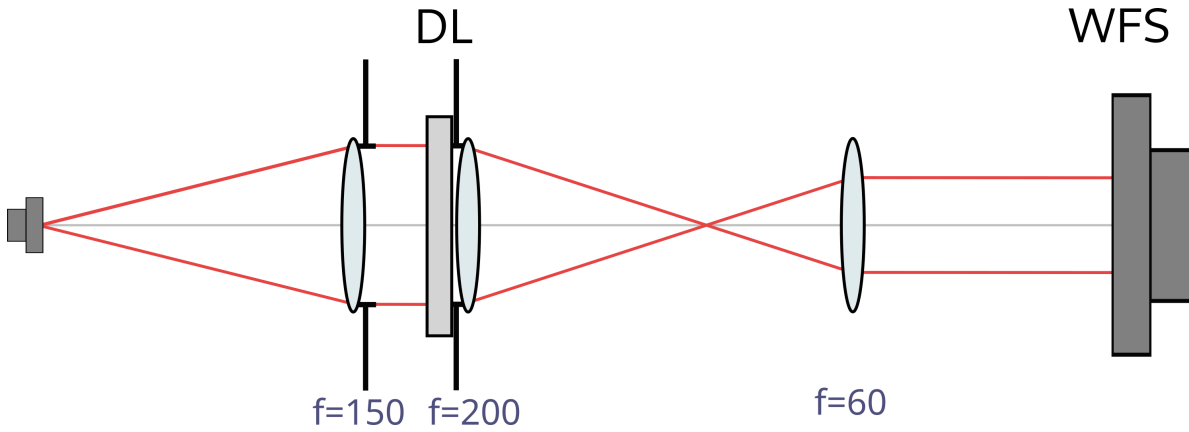
Figure 5.3: Calibration setup schematics. The deformable lens (DL) is placed where the laser beam is collimated. A telescope configuration is used to adjust the magnification of the beam, properly sizing it to the Shack-Hartmann wavefront sensor.
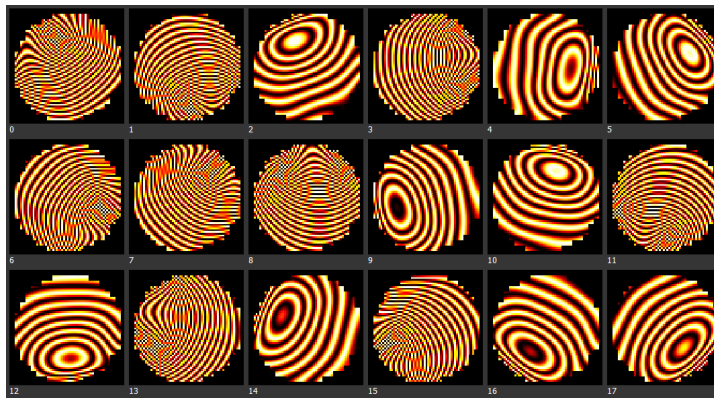

Figure 5.4: Example of actuation modes in Photonloop, performed by the calibration procedure; the figure shows the position and the amplitude of the actuators when acting on the wavefront detected by the wavefront sensor.
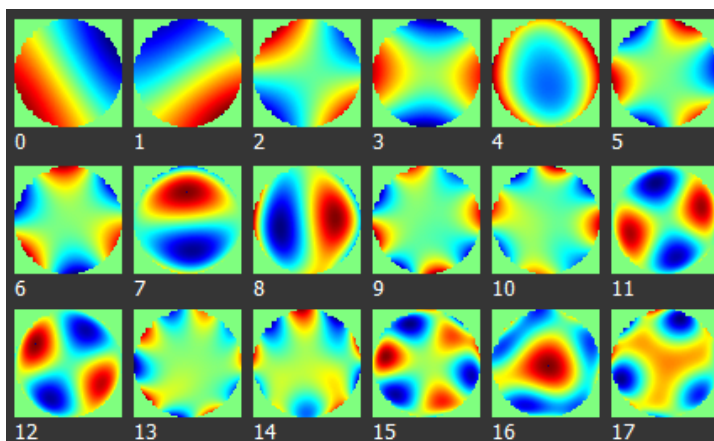

Figure 5.5: Example of lens modes in Photonloop, performed by the calibration procedure; the figure shows the orthonormal lens modes that closely resemble Zernike modes. The orthonormalization favours lower order modes, by sending distortion effects on higher order lens modes.
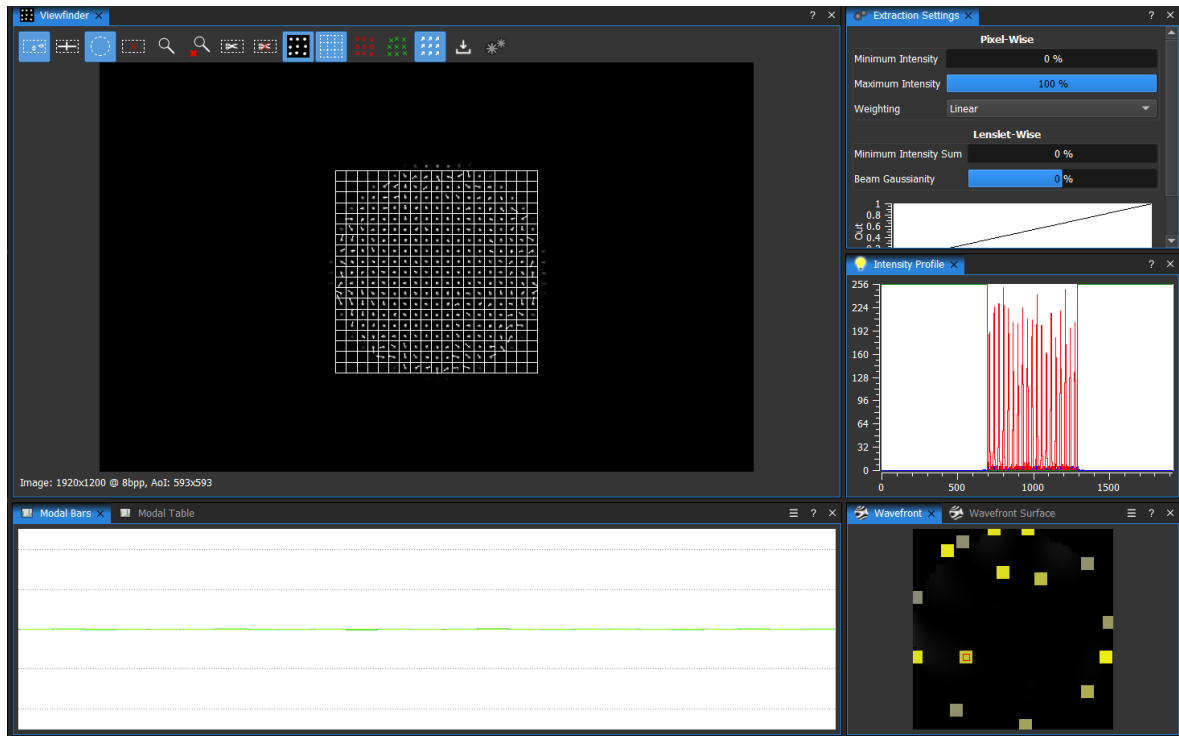
Figure 5.6: Example of Photonloop wavefront detection, performed in the calibration proce-
dure; blurry spots are the effective signal collected by the lenslet array. Using the wavefront
sensor physical distance informations, the grid is set so that the relative distance of spots from
the square center can be calculated; once centroids of spots are known, the wavefront recon-
struction can be done; the vector escaping from each spot graphically indicates the deviation
from the center.

aberrations of the resulting wavefront; the lens position is adjusted by hand until the nullification
of the defocus (Z_2^0) mode. The wavefront sensor is then set in the final position, so that its optical
plane is conjugated with the pupil plane; the pupil plane itself coincides with the aperture stop
provided by the deformable lens. Absortive neutral density filters have been used ($20\,\mathrm{dB}$ or $30\,\mathrm{dB}$
intensity attenuation) to avoid the saturation of the sensor.

Once the deformable lens is positioned, the calibration procedure is performed using a program,
developed and curated by Dynamics Optics and Padua's IFN Adaptive Optics laboratory, called
PhotonLoop. The software, for the purpose of this part, interfaces the wavefront sensor output
data with the actuation system of a deformable lens.

The first step is to ensure the wavefront sensor is effectively conjugated with the deformable lens.
In this configuration, when the deformable lens actuators are driven, the resulting number of spots
produced by the wavefront sensor shouldn't change; experimentally, the wavefront sensor is moved
along the optical line until the optimal condition is obtained.

At this point, the calibration procedure of lens is performed, by driving each actuator over its stroke
range and register the configuration of the wavefront change; using this procedure, calibration
data necessary to reconstruct the slope influence matrix are obtained; Photonloop automatically
interpolates Zernike polynomial coefficients associated with the actuators and provides the Zernike
mode influence matrix (section 4.2).

Photonloop is also used to obtain the flat lens configuration; in this case the software uses the

influence matrix informations to drive to lens' to the configuration that actively flattens the wave-front; this configuration is successively used as the default correction state of the lenses during the experimental activity.

5.3   Adaptive optics two lenses control setup
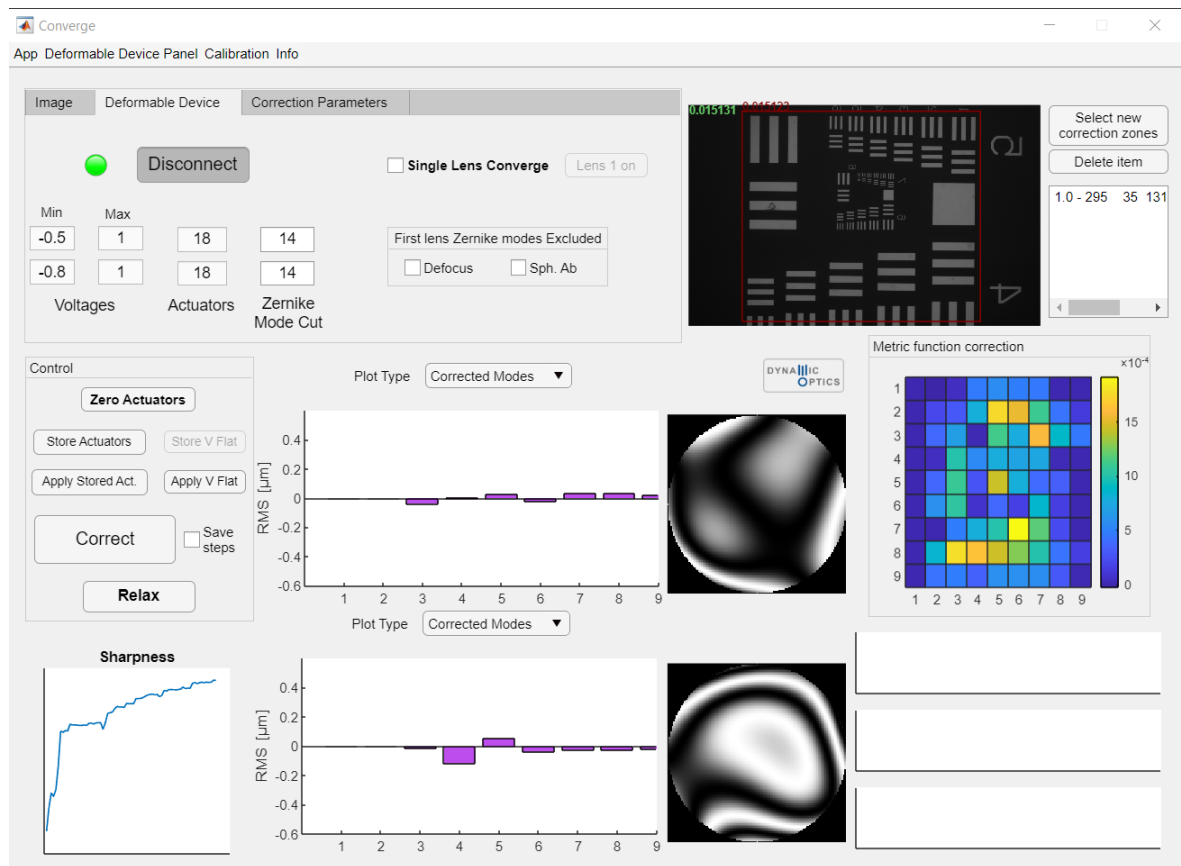
Figure 5.7: Control software interface Converge. The modified version of the software works in widefield configuration using two deformable lenses. It is possible to specify zones where the correction algorithm should act while observing the widefield effect of the correction on the 9×9 matrix. The correction algorithm keeps track of Zernike modes generated by the lenses and shows them on an interferogram.

The software part is necessary to combine the control and the sensing part of the experimental setup. The starting point for this part is the control software developed by Padua CNR IFN Adaptive Optics group, written in MATLAB, called Converge. The software executes the quadratic model optimization (section 4.3.3) given a camera stream considering whole image for the estimation of the metric function (subsection 4.3.2); parameters allow the tune the behaviour of the algorithm in terms of amplitude, number of cycles and number of considered Zernike modes; the calibration of lenses from the previous section is used in order to reliably estimate actuators state change in terms of Zernike mode coefficients. The metric function values are tracked in order to confirm the correct convergence of the indirect method algorithm.

For the scope of this thesis work, we study and extend Converge in order to support the operation in widefield using two deformable lenses. The programming interface to the second lens is provided via a custom API; we verify that the software input signal corresponds to the expected voltage signal of the electronics that controls the lens as a checking step. We modify the image quality using metric function in order to support the widefield configuration; we estimate the total image quality using a linear combination of user-provided weights with values of metric function applied to partial and multiple regions of the image. We implement the local image metric function variation as a grid
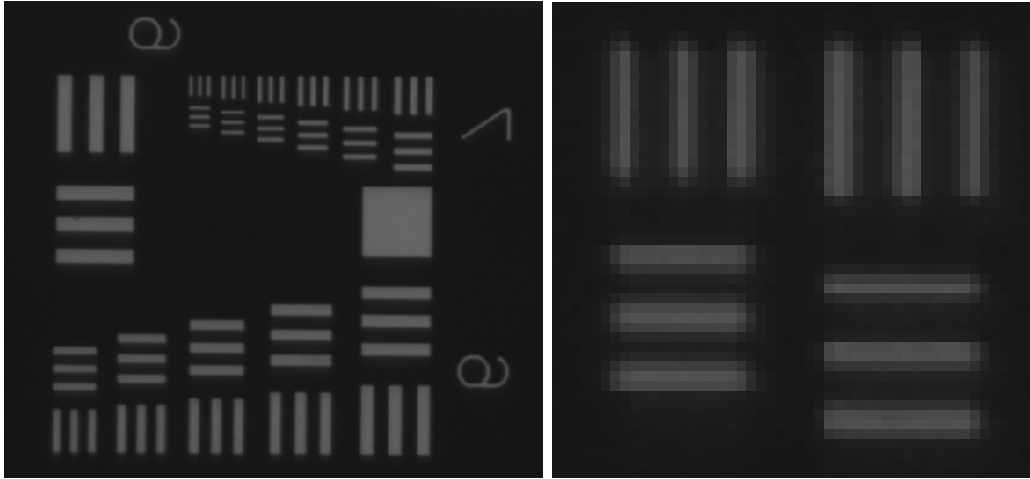
Figure 5.8: Experimental imaging example, zoom on the USAF-1951 target groups 6, 7; deformable lenses are in the calibration flattened position (left). Increased zoom on the highest resolution features shows they are clearly resolved (right).

of 9×9, on order to qualitatively estimate the local change of the image quality. We change the quadratic algorithm in order to support operation over two lenses. Specifically, the quadratic model algorithm repeats three times with exponentially decreasing interval lengths for the seeking of the maximum, iterating over successive Zernike modes of the first and second lenses; the algorithm is a $2N + 1$-type search. We also adapt functions that generate output data in our to support the second lens.

5.4 Preliminary considerations

We proceed with preliminary measurements of the current setup to precisely evaluate some of useful quantities that characterize it.

5.4.1 Magnification and resolution limits

The actual magnification of the system can be estimated by making use of the USAF 1951 target resolution standard. We do it by estimating the USAF target line distancies of a specific set of lines; in this case group 4 is experimentally used due to being the largest and best fitting target capturable in the field of view. The physical calibration resolution of a USAF target between two lines of a specific (group, element) couple is given by the standard:

$$\text{resolution} \left[\frac{\text{lp}}{\text{mm}} \right] = 2^{\text{group}+\left(\frac{\text{element}-1}{6} \right)}$$

in this case, the inverse of the resolution results in the physical distance between two lines.

We create a Python script in order to evaluate the line pair distance of the magnified USAF 1951 target. By using ImageJ to obtain intensity data along the group 4 of USAF 1951 target (Figure 5.9), we calculate the intensity-weighted position of each line after clipping intensity values, as an intensity-weighted position; the halved difference between the first and the third line positions for each USAF element number allows to obtain the distance in pixels; at this point, using the standard:

$$\text{res}_{USAF,meas,i} = \text{resolution}_i \left[\frac{\text{lp}}{\text{mm}} \right] \cdot \text{line pair distance}_i \left[\frac{\text{px}}{\text{lp}} \right] \tag{5.1}$$
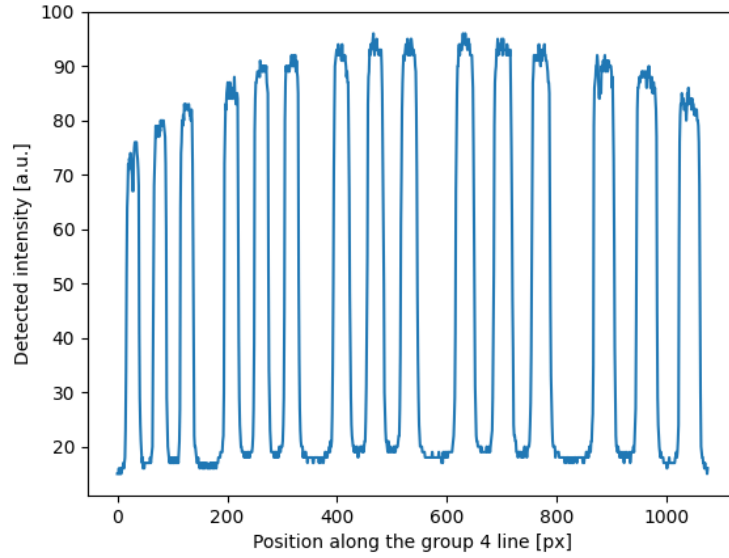
Figure 5.9: Experimental intensity profile along the group 4 of USAF 1951 target used for the estimation of the system magnification.

and averaging we obtain the estimate of the imaged target resolution.

By dividing by the resolution of the camera the magnification is obtained:

$$M = \frac{\text{res}_{USAF,meas}}{\text{res}_{camera}} = \frac{(1395 \pm 3)\frac{\text{px}}{\text{mm}}}{170.65\frac{\text{px}}{\text{mm}}} = (8.18 \pm 0.02)$$

The resolution of the field can be limited by three causes: camera spatial resolution, aberrations and the diffraction limit of the microscope.

The theoretical resolution of the system can be estimated using the Rayleigh resolution criterion (section 3.2):

$$|\bar{r}_{\perp}^{in}| = 0.610 \cdot \frac{\lambda}{NA} = 1.0\,\mu\text{m}$$

in this experimental setup the illumination $\lambda = 480\,\text{nm}$ and the objective $NA = 0.28$.

The camera allows the separation of features when they are positioned with a distance of at least 2 pixels one to each other; this corresponds, with the current magnification, to:

$$\Delta x_{min,obj} = 2 \cdot \frac{\text{px size}}{M} = 1.4\,\mu\text{m}$$

considering the actual pixel size of the camera is px size $= 5.86\,\mu\text{m}$.

This results to be resolution limit in the best aberration-corrected conditions.

5.4.2 Tip-tilt stage calibration

We perform the calibration procedure on the cinematic mount (VM1, Thorlabs) in order to accurately estimate the tilting angle of the sample placed on the stage during the tip-tilt experimental measurements.
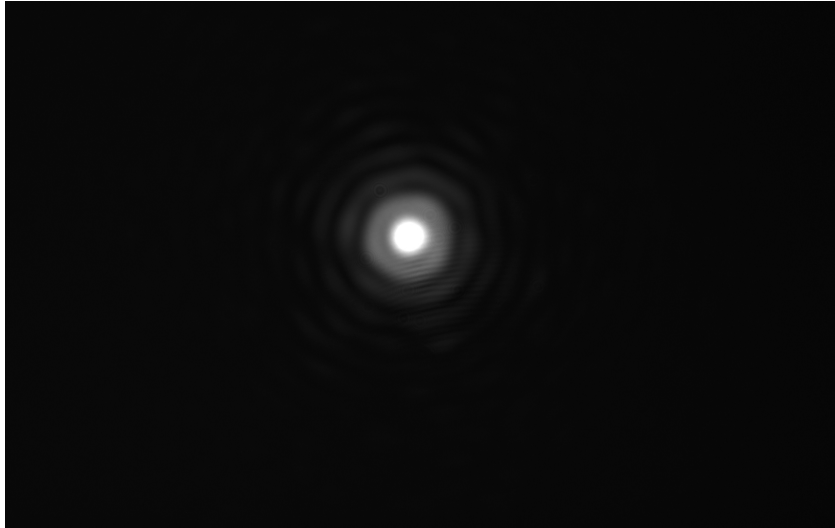
Figure 5.10: Example of the collimated laser beam restricted by an iris, during the cinematic mount calibration; the central brightest spot is used to determine the effective position deviation due to the tip/tilt rotation of the mount.

The calibration stage setup (section 5.2) been modified by replacing the wavefront sensor with a mirror mounted on the cinematic stage; an iris has been placed in between for a clear estimation of the center. The mirror is positioned with a tilt angle to the optical axis so that the laser beam could continue to travel; a camera (IDS UI306xCP-M) has been placed on the end of the setup, with the distance $L = (255 \pm 5)$ mm from the mirror.

We take a sequence of measurements after the application of linearly increasing tilt angles.

At this point, we process the sequence of images by writing a Python analysis program and find the centroids: discarding the noise and the diffraction rings around the central spots by clipping intensity at lower values, identifying the centers by estimating the mean position of the valid spot points; the linear interpolation of distancies between the initial and the current centroid provides an estimate of the distance (in pixels) as function of stage rotations; the conversion to angular distancies is found using the mirror-camera distance $L = (255 \pm 5)$ mm; the angular measurement is performed using a mirror, while the stage itself is used in a transmissive configuration; this results in an extra factor two in the angular estimation which is taken away.

The procedure, repeated for the vertical and horizontal stage action, provides following estimation of tip/tilt angles per mount rotation:

$$\eta_V = (0.195 \pm 0.004) \, \frac{^\circ}{\text{turn}}$$

$$\eta_H = (0.232 \pm 0.005) \, \frac{^\circ}{\text{turn}}$$

Chapter 6

System simulations

6.1 Simulation software

We perform simulations of the microscopy setup based on two deformable lenses using the MATLAB application written by Padua CNR IFN Adaptive Optics group.

The system is simulated as a four-plane optical chain, formed by the object plane, the pupil lens plane, the non-pupil lens plane and the image plane. Informations about aberrations are encoded in terms of circular wavefronts decomposed on the basis of Zernike polynomials. The propagation though deformable lenses is described in terms of circular phase screens decomposed over the Zernike basis; aberrations in the object and image spaces are represented as the wavefront over a circle rather than physically focalized (and consequently Fourier transformed) points.

Aberrations in the object plane (input) and the image plane (output) are represented over a 9×9 matrix; the effective circular field of view takes into exam only 49 elements of the matrix. The position on the matrix corresponds to the position over the field of view in the physical setup.

The simulation software allows to specify pupil as well as non-pupil lens diameters; the knowledge of these two parameters fully constraints the widefield setup distances, given the non-pupil lens surface is fully scanned by the varying the position over the field of view in the object space. The degree of aberrations over the field of view is specified by adjusting Zernike coefficients for each entry of the object space matrix.

The wavefront passing through the pupil lens is modified by the direct application of the phase screen due to the pupil lens. The wavefront passing through the non-pupil lens ($r_{\text{WF at non-pupil lens}} = r_{\text{pupil lens}} < r_{\text{non-pupil lens}}$) doesn't fully overlap the lens; this is taken into account by calculating the relative position between wavefront and lens centers; the computation of aberrations is done in the space of Zernike polynomial coefficients over the circular pupil aperture, the phase modification due to the non-pupil lens cannot be simply performed since it doesn't match the circular domain of the incoming wavefront (due to the pupil); consequently the computation do to the partial overlap of the non-pupil lens is performed by casting the phase modification contribution of the non-pupil lens in cartesian coordinates to the set Zernike coefficients, by taking into account the relative position between the centers of two circular domains and their radiuses, then recasting the contribution back in the space of Zernike coefficients over the pupil of the incoming wavefront. This way the wavefront in the image plane is determined.

By considering all positions over the field of view the simulator takes into account aberrations over the widefield. The simulator acts as an optimizer that minimizes the initial aberrations over the

widefield considering the action of pupil and non-pupil lenses on the system.

The optimization algorithm itself inverts the $Ax = b$ system via least squares minimization. b represents the vector of target aberrations in the object plane that are requiring the correction, repeated over all positions of the field of view; this situation is equivalent to evaluating aberrations in the uncorrected image plane; each aberration is represented by a Zernike basis with $N = 100$ coefficients, forming a vector of real numbers; A is the matrix that represents the action of the system on the wavefront from the object to the image plane given by each lens in terms of Zernike coefficients, for all positions in the field of view; x is the vector of the Zernike coefficients applied to each lens of the system.

The optimal solution provides the matrix of residual aberrations in the image space and the relative RMS for each position over the field of view, as well as Zernike termed aberrations applied to each lens.

Two common widefield microscopy aberration situations have been studied using the simulations: the sample tip-tilt curvature and Petzval (or field) curvature.

6.2   Sample tip-tilt aberration

We consider a situation of widefield tip-tilt aberration; the sample results to be not perfectly aligned with the theoretical object plane. This case has been represented in the simulation as a uniformly increasing defocus Z_2^0 mode over the horizontal direction, with zero in the center of the field of view.

The simulation results for the case of correction with two lenses are presented in Figure 6.1a, Figure 6.1b, Figure 6.1c.

The simulation of the case of the only pupil lens doesn't produce changes, indicating that the pupil only correction doesn't affect tip/tilt alignment errors of the sample.

In case of two lenses simulation, the pupil lens partecipates in the correction; it produces the same (Z_3^1 (horizontal coma)), oppositely directed aberration, balancing the contribution of the non-pupil lens on the widefield correction.

6.3   Petzval curvature

We study the case of Petzval (or field) curvature; in this case the formation of the image is expected to be on a spherical surface; consequently, the simulation models this behaviour as a defocus with an amplitude proportional to the profile of a spherical surface on the image plane.

6.4   Discussion

6.4.1   Sample tip-tilt

The simulations on the widefield sample tip-tilt show the creation of opposing coma modes for the pupil and non-pupil lenses; these modes are oriented in the sample tilt direction; additional modes for the non-pupil lens shown ($Z_{18}, Z_{20}, \dots$) are not accessible to the lens. The simulation also shows that the correction applied using only the pupil lens generates no modes, thus there is no correction in this configuration.

As shown in Figure 6.1b, astigmatism aberrations ($Z_2^{\pm 2}$) remain after the correction procedure as well as the uncorrected defocus (Z_2^0) part. The defocus gradient amplitude is reduced by 50%. The horizonal coma aberration (Z_3^1), shown in the lenses' modal bars (Figure 6.1c) is almost completely cancelled by the opposing action of lenses. The root mean squared of aberrations in widefield is decreased by 20%.

6.4.2 Petzval curvature

The case of Petzval curvature correction takes into examination the full image field correction and the correction using a square with the side of half diameter of the field.

The first case case takes into exam configurations of pupil lens only, non-pupil lens and two lenses acting together (Figure 6.5).

It has been observed that the correction in the pupil lens only case is given by the defocus mode Z_2^0. In case the non-pupil lens together with the defocus mode (Z_2^0), other modes like spherical aberration (Z_4^0) and vertical quadrafoil (Z_4^4) are generated; higher order modes are generated but are not usable due to the capabilities of the lens to generate up to 4th Zernike order aberrations. In case of the two lenses correction, defocus modes (Z_2^0) generated by both lenses compensate each other; the first lens also generates small amounts of spherical aberration (Z_4^0) and vertical quadrafoil (Z_4^4), while the second one gives additional spherical aberration (Z_4^0) and a small amount of vertical quadrafoil (Z_4^4).

Further results relative to the widefield RMS of relevant aberration modes is presented in Figure 6.6; second order aberrations ($Z_2^{0,\pm 2}$), coma ($Z_3^{\pm 1}$) and spherical aberration (Z_4^0) are present.

The both lenses case provides the best full field RMS (0.094λ RMS) but leaves the central region with a relevant amount of aberrations.

In case of the reduced widefield correction, the total RMS is reduced (0.192λ RMS vs 0.142 RMS) but the corrected field is at the diffraction limited aberration limit (up to 0.07λ RMS, Marechal criterion); the situation is visualized in Figure 6.8. In this case a stronger contribution of both lenses is noticeable; in particular, for the second one, the amplitude of the spherical aberration (Z_4^0) and vertical quadrafoil (Z_4^4) is amplified.
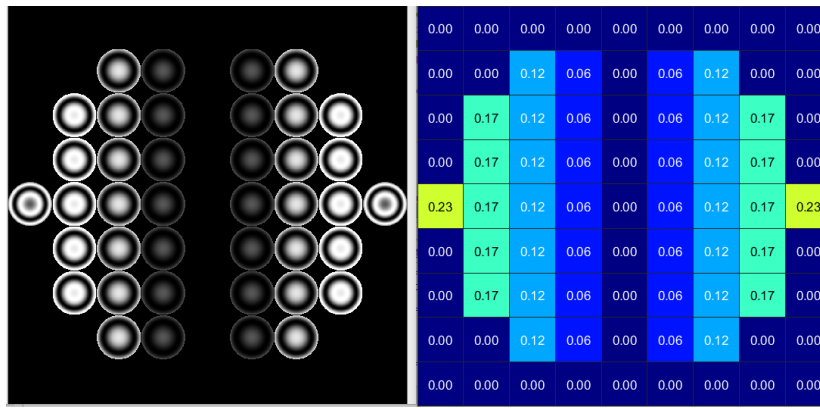
(a) Sample tip-tilt aberration, initial case. The initial mean RMS of the system is 0.093λ. The values in the squares represent the RMS of the specific portion of the field of view.
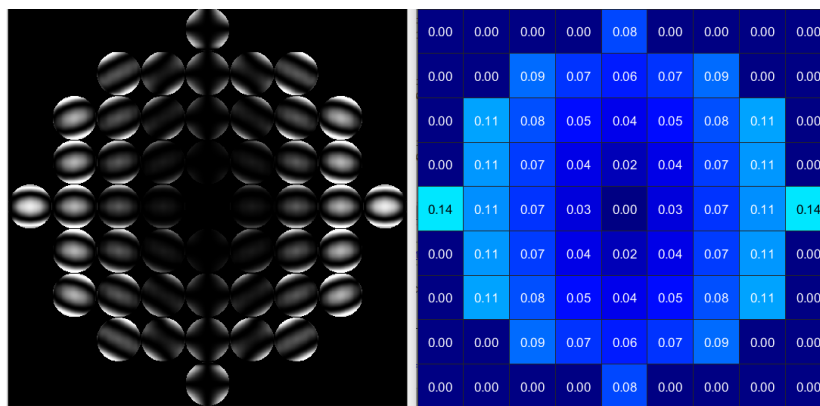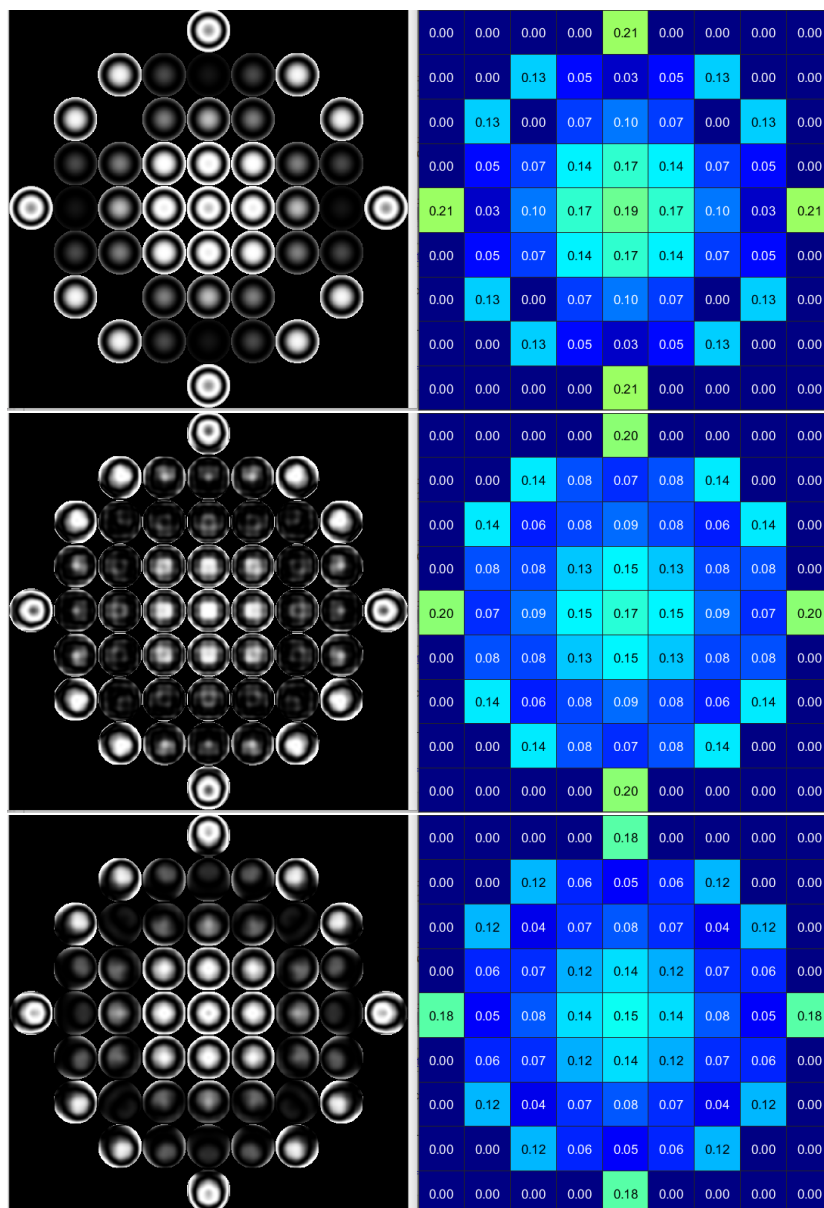

(b) Sample tip-tilt aberration, two-lenses correction. The mean RMS of the system is 0.074λ. The values in the squares represent the RMS of the specific portion of the field of view.
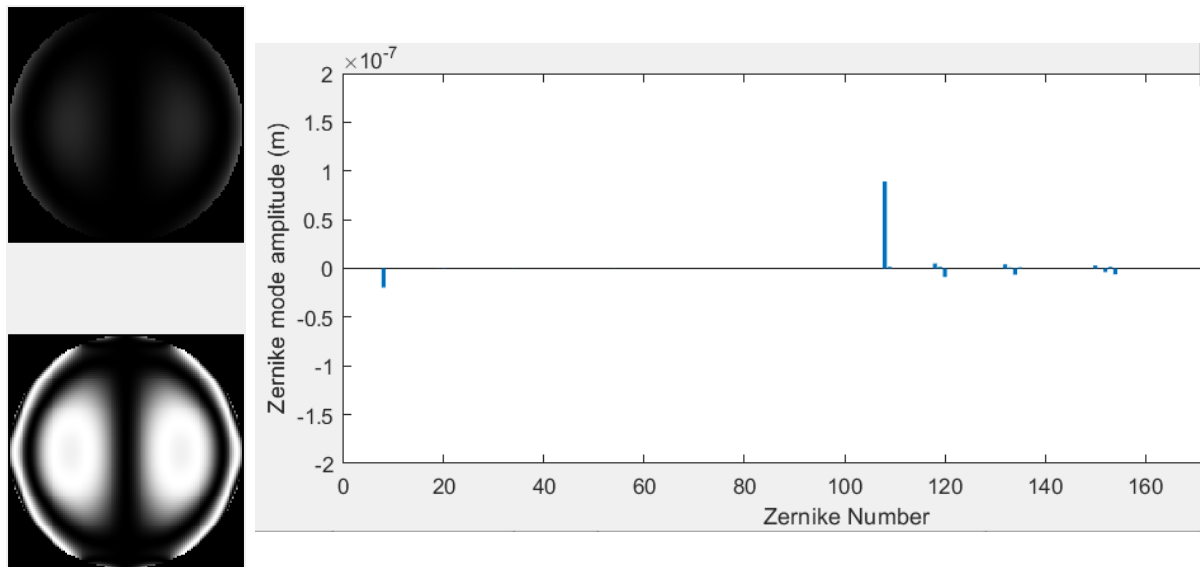
(c) Interferogram of the configuration of two lenses; pupil lens (above) and pupil lens (below). Relative Zernike mode intensity bars ($n < 100$ for pupil lens, $n \geq 100$ for non-pupil lens); the modes produced by the lens ($n \leq 14$) are: Z_3^1 (horizontal coma) for the pupil lens and Z_3^1 (horizontal coma) for the non-pupil lens as well.

Figure 6.1: Sample tip-tilt aberration simulations.
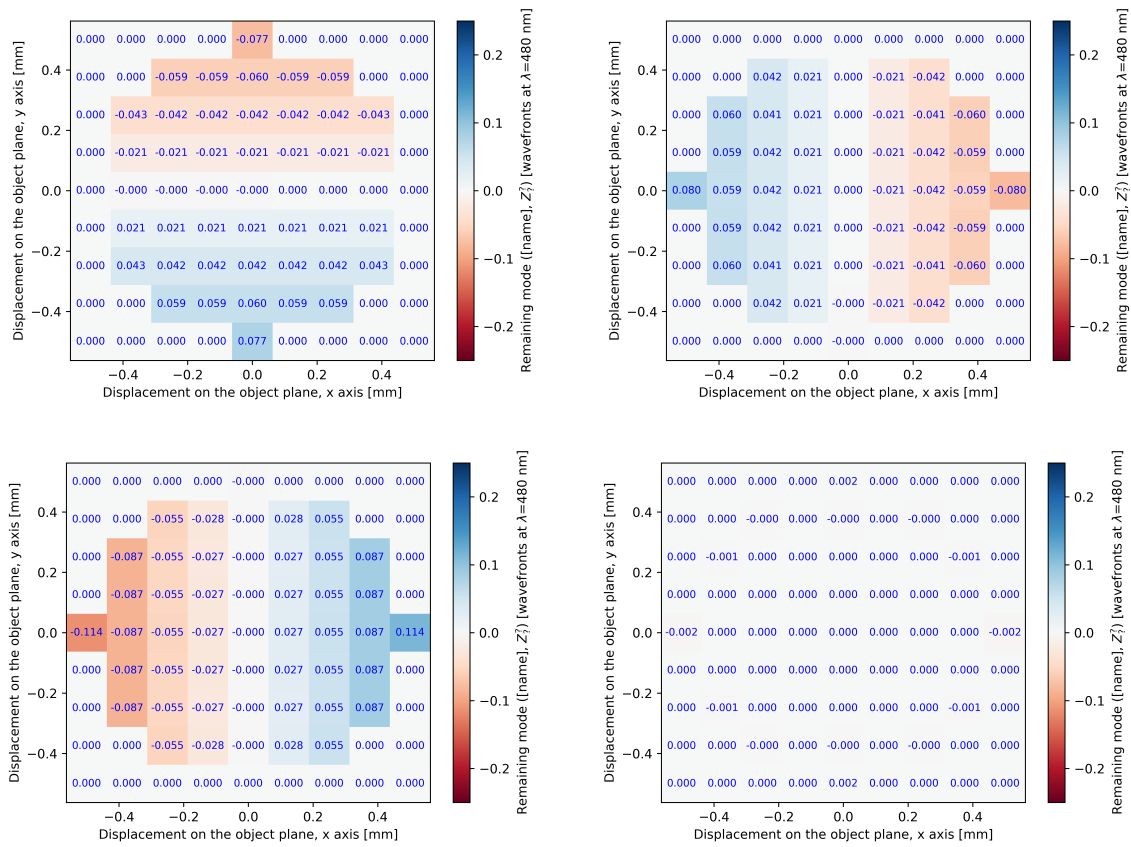
Figure 6.2: Relevant residual aberrations on the widefield. Respectively oblique astigmatism (Z_2^{-2}), vertical astigmatism (Z_2^2), defocus (Z_2^0) and horizonal coma (Z_3^1).
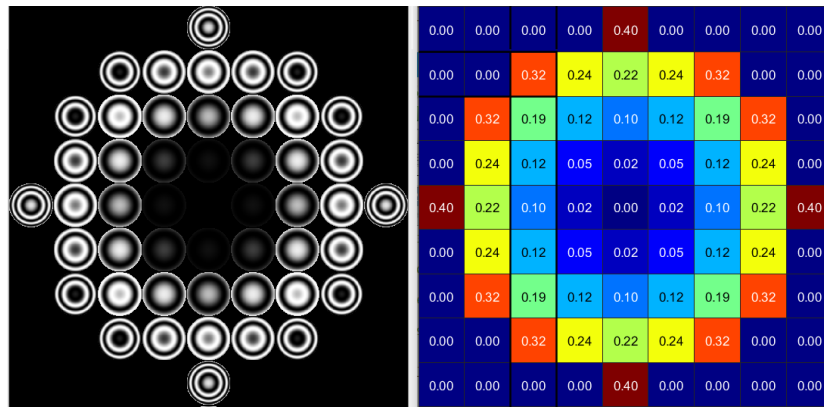
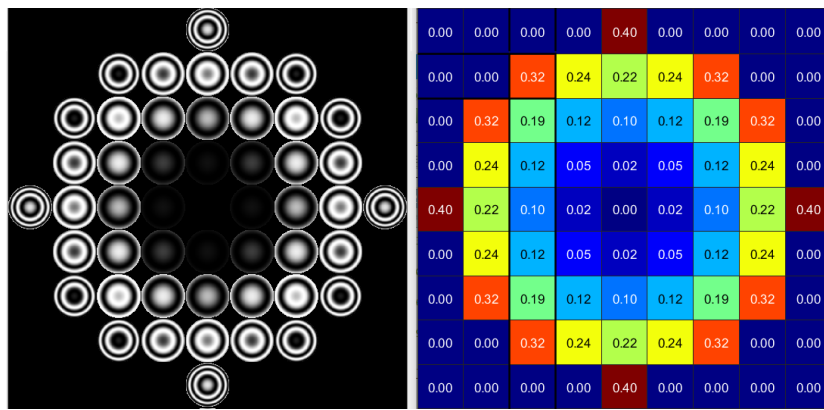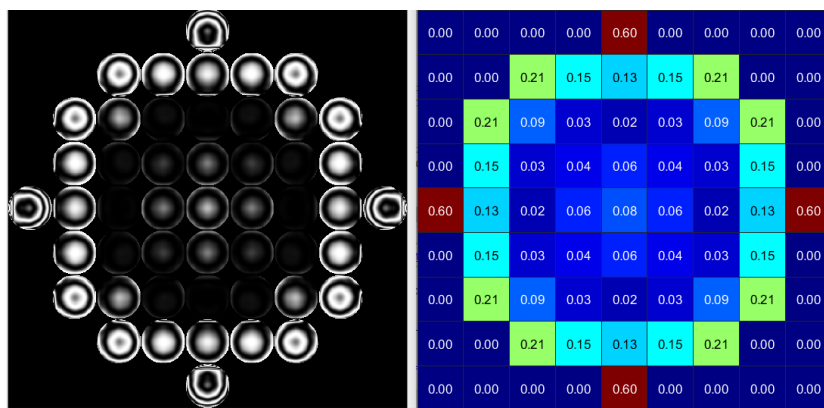Figure 6.3: Widefield aberrations representation, initial field curvature case. The initial mean RMS of the system is 0.192λ. The values in the squares represent the RMS of the specific portion of the field of view.

Figure 6.4: Widefield aberrations representation, respectively pupil lens, non-pupil lens and two lenses correction for field curvature case. The mean RMS of the system is 0.098λ (pupil lens only), 0.109λ (non-pupil lens only) and 0.094λ (two lenses). The values in the squares represent the RMS of the specific portion of the field of view.
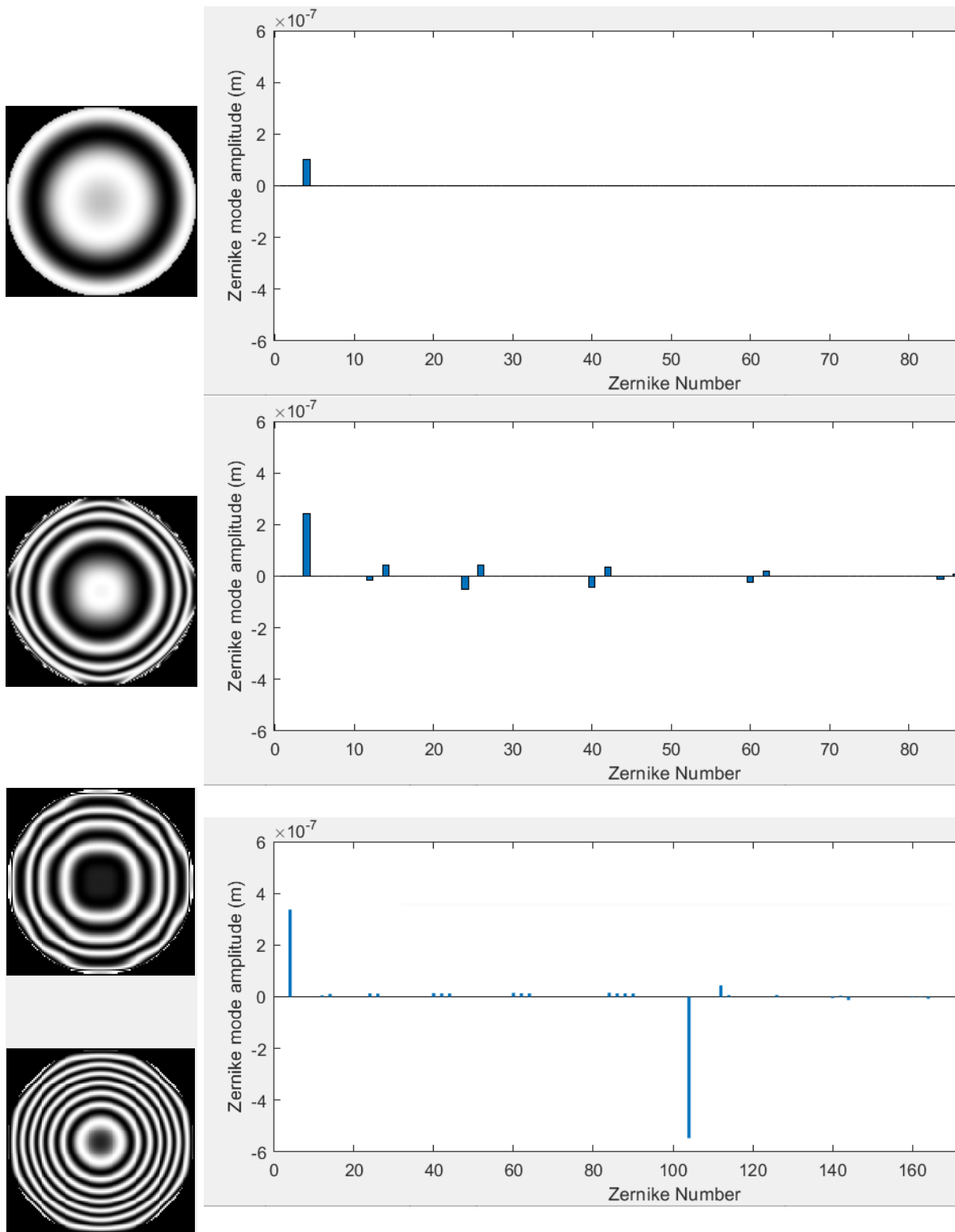
Figure 6.5: Interferogram and modal bars representation in case of Petzval curvature. Pupil lens only configuration (above) produces defocus (Z_2^0) mode. Non-pupil lens only configuration (middle) also shows a little of spherical aberration (Z_4^0) and vertical quadrafoil (Z_4^4) mode. The configuration of two lenses (below) shows the generation of oppositing defocus modes (Z_2^0) and a relevant amount of spherical aberration (Z_4^0) for the non-pupil lens. The relative Zernike mode intensity bars in the two lenses configuration are: $n < 100$ for pupil lens, $n \geq 100$ for non-pupil lens; the modes produced by the lens are $n \leq 14$
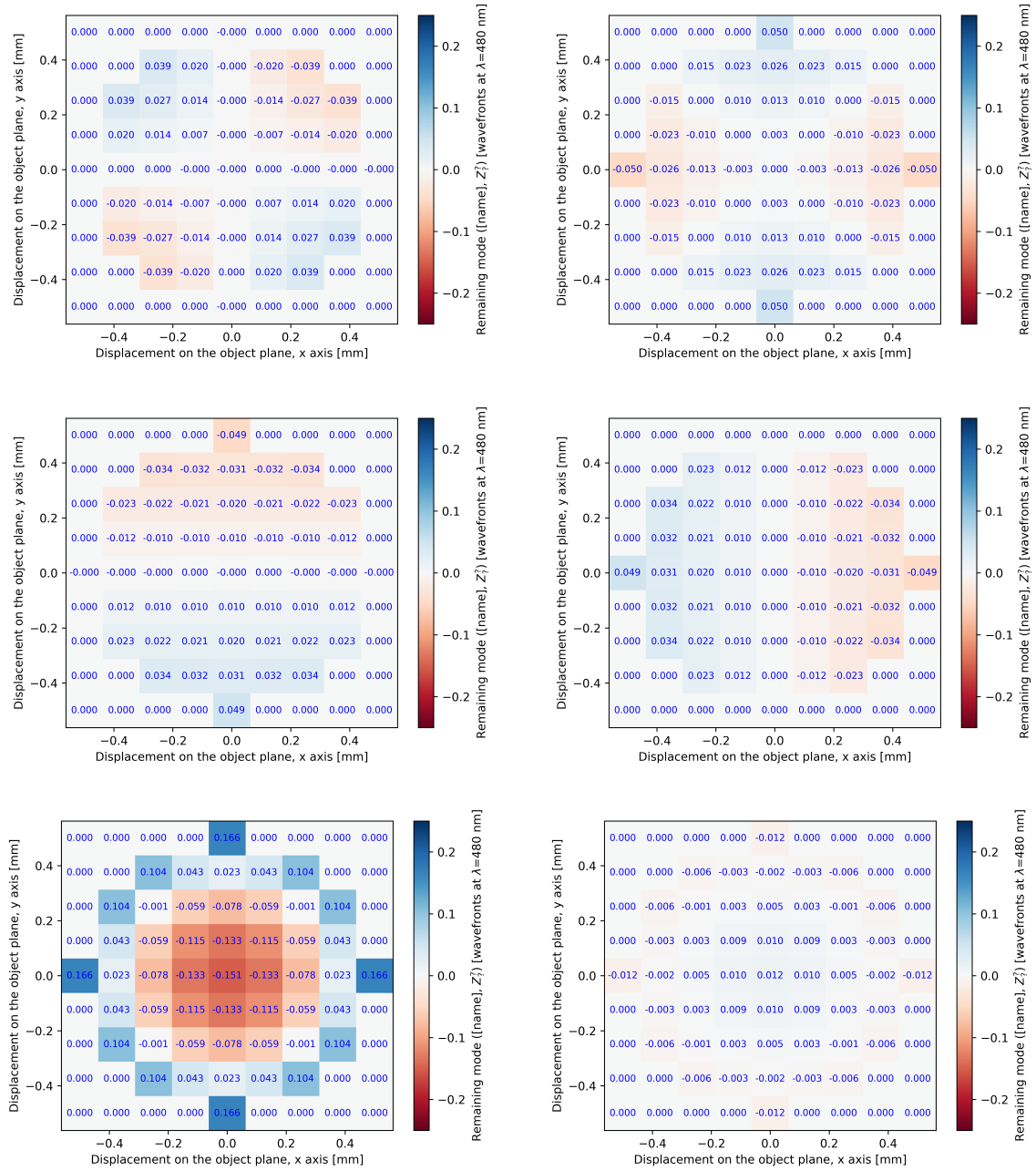
Figure 6.6: Relevant residual aberrations on the widefield. Respectively oblique astigmatism (Z_2^{-2}), vertical astigmatism (Z_2^2), vertical coma (Z_3^{-1}), horizontal coma (Z_3^1), defocus (Z_2^0) and spherical aberration (Z_4^0).

Figure 6.7: Widefield aberrations representation, initial field curvature case (5/9 radius wide-field correction). The initial mean RMS of the system is 0.192λ. The values in the squares represent the RMS of the specific portion of the field of view.

Figure 6.8: Widefield aberrations representation, two lenses field curvature case (5/9 radius widefield correction). The mean RMS of the system is 0.142λ. The values in the squares represent the RMS of the specific portion of the field of view.
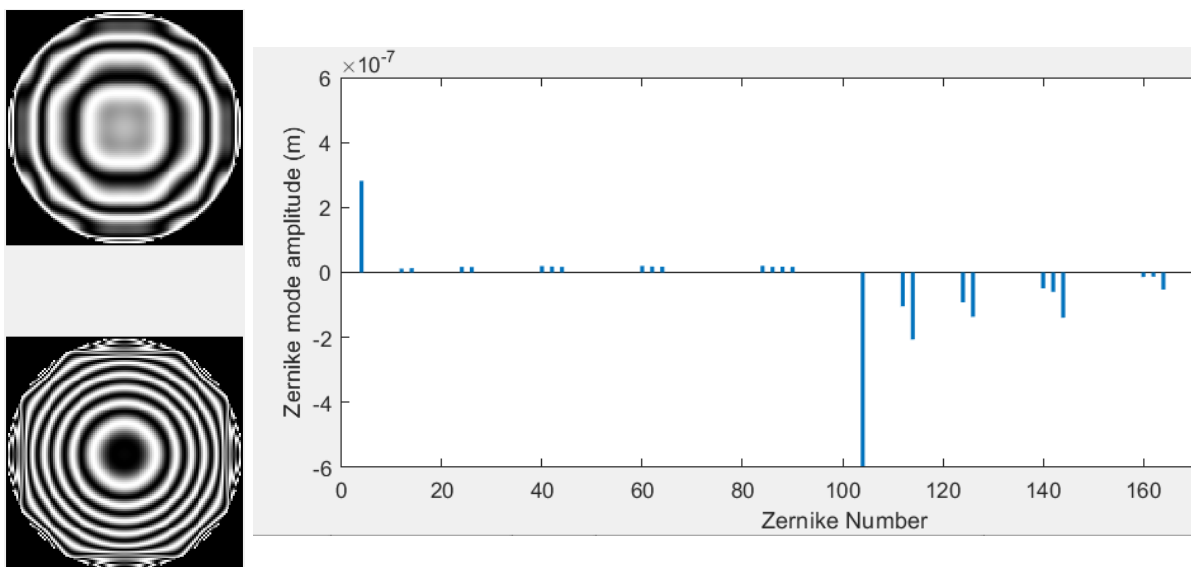
Figure 6.9: Interferogram of the configuration of two lenses; pupil lens (above) and pupil lens (below). Relative Zernike mode intensity bars ($n < 100$ for pupil lens, $n \geq 100$ for non-pupil lens); the modes produced by lenses ($n \leq 14$) are: Z_2^0 (defocus) for the pupil lens and Z_2^0 (defocus), Z_4^0 (spherical aberration), Z_4^4 (vertical quadrafoil) for the non-pupil lens.

Chapter 7

Sample analysis

7.1 Experimental goal

The experiment has been designed with the purpose to implement a transmissive multiconjugated adaptive optics (MCAO) correction system for microscopy; compared with the solutions employing deformable mirrors (section 4.1), deformable lenses don't require the modification of the optical path of the system; this results in a convenient solution, given research-grade microscope complexity allows strict conditions for the optical path customization. The usage of optical lenses, in contrast with spatial light modulators, allows the production of continuous wavefront shaping over the lens' surface and avoids problems like SLM pixel cross-talk.

In this practical implementation we demonstrate the correction capabilities of the multiconjugated adaptive optics MCAO configuration with both pupil and non-pupil lenses, in comparison with the pupil single lens configuration in case of a $1.134\,\text{mm} \times 0.713\,\text{mm}$ field of view; we also include the non-pupil lens configuration for reference with simulation results.

With this experimental activity we focus on measuring effects of the sample tip-tilt deviation on the quality of the resulting image. We estimate the actuation configuration of lenses after the correction; consequently we observe the behaviour of lens induced aberrations (written in Zernike basis, for each lens) as function of a specific tilt angle.

Theoretically, the pupil only case is expected to be uncorrected due to the antisymmetry of the wavefront as function of the observation distance over the tilting axis in the image plane, while the application of aberrations using the pupil deformable lens always results in a symmetrical wavefront contribution. The usage of the non-pupil lens breaks the symmetry and allows to discriminate the correction over different positions in the field of view.

The sample tip-tilt case simulations show no aberration variations should observed for the case of the only pupil lens; for the case of both lenses, horizontal coma (Z_3^1) should be observed for the non-pupil lens and, at a minor degree, for the pupil lens with an opposing amplitude direction.

7.2 Analysis pipeline

We perform the analysis of output images using two different methods.

The first type of analysis makes use of the USAF 1951 sharpness characteristics; the image quality is estimated as the frequency response of the modulation transfer function (MTF) by analysing the local features in different zones.
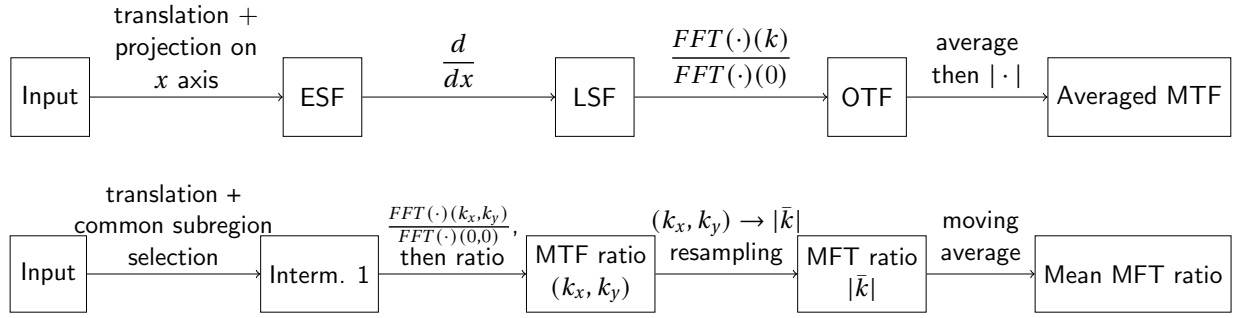
Figure 7.1: General analysis scheme.
Respectively edge differentiation method (above) and full image MTF ratio method (below).
The edge differentiation method makes use of the image proprocessing stage by superimposing
common image regions; a line in a region of interest is selected obtaining edge spread function
(ESF); the line spread function (LSF) is obtained after the differentiation; it is converted to
the optical transfer function (OTF) via Fourier transformation; multiple estimates are averaged
providing a candidate mean OTF; the modulation transfer function (MTF) is obtained after
the absolute value application.
The full image MTF ratio method selects the common subregion for images; both images are
Fourier-transformed and zero-frequency normalized, their ratio is taken pixel by pixel producing
an MTF ratio in (k_x, k_y) domain; the resampling to $|k|$ domain is done by averaging logarithms
of MTF ratios; an $N = 20$ moving average is applied for visualization purposes.

The second method uses the full image to describe the response of the system. This is done by
comparing the corrected and the initial images in the Fourier domain.

The full analysis pipeline of two methods is brefly illustrated in Figure 7.1.

7.2.1   Preprocessing stage

Images are preprocessed with a two step procedure:

- relative position identification and translation;

- common subregion cut (relevant step only for full image analysis).

In the relative position identification step, a simple algorithm based on Fourier Transformation,
provided by [16], has been used.

Using shift properties of the Fourier Transform when f_2 is a translated version of f_1:

$$f_2(x, y) = f_1(x - x_0, y - y_0)$$

becomes

$$F_2(k_x, k_y) = e^{-j(k_x x + k_y y)} \cdot F_1(k_x, k_y)$$

in the Fourier domain.

The calculation of the cross-power spectrum leads to

$$\frac{F(k_x, k_y)G^*(k_x, k_y)}{|F(k_x, k_y)G(k_x, k_y)|} = e^{j(k_x x + k_y y)} \tag{7.1}$$
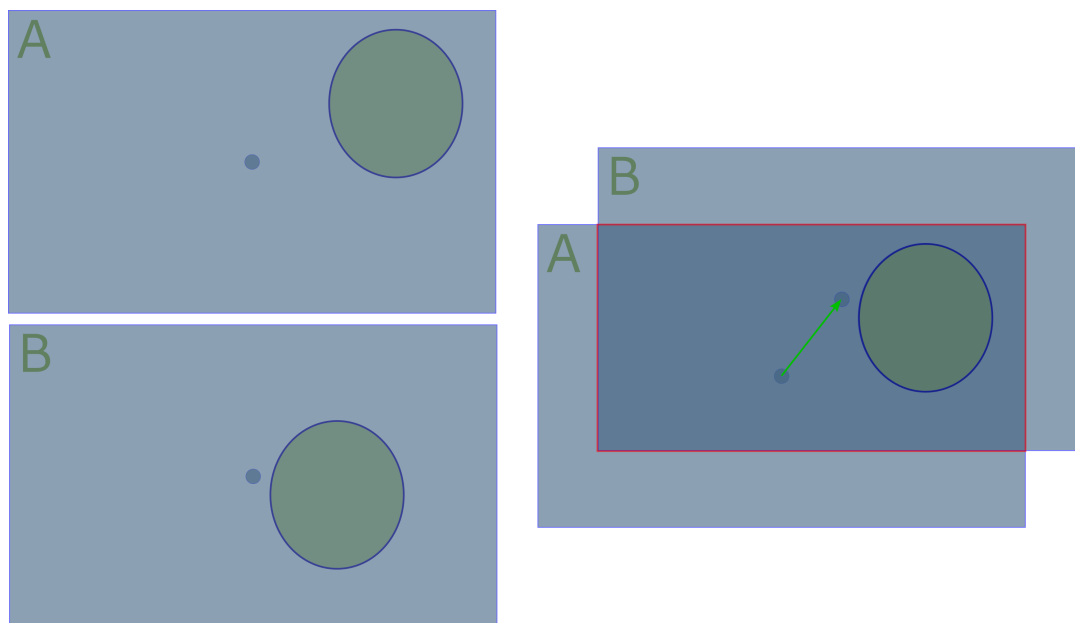
Figure 7.2: Preprocessing stage. The procedure identifies the translation vector for two images (green arrow) then selects the common subregion (red border).

which is a translated Delta function $\delta(x - x_0, y - y_0)$ in Fourier space.

The algorithm evaluates the inverse Fourier transform of Equation 7.1 and finds the maximum intensity index of the resulting matrix which corresponds to the translation vector. Given two images as input, the second is translated accordingly.

In case of full image analysis, two images have been cut taking away their non-overlapping portions in order to evaluate the spatial frequency characteristics over the same features; the non-overlap is made evident after centering two images using the translation algorithm (above), the translation vector specifies the portion of image needed to be cut.

For the edge differentiation method (subsection 7.2.2), the translated image is directly used.

7.2.2 Edge differentiation method

The edge differentiation method [9] has been used in order to estimate the modulation transfer function (MTF) of the microscope and compare the correction effect of different adaptive lenses configurations; in order to estimate the effect of the correction in the context of widefield microscopy, four corners of the target have been analysed.

The edge differentiation method can be used when imaging elements with sharp edges; this allows to determine the transition profile between the dark and illuminated regions and compare the degree of smearing due to aberrations in the specific image region in terms of modulation transfer function (MTF).

As first step, an intensity histogram over an axial line is plotted, highlighting the feature that presents the transition region; the resulting diagram represents the edge spread function (ESF). The derivative of ESF is calculated, producing the line spread function (LSF). The line spread function is Fourier-transformed and normalized by the zero-frequency term, producing the optical transfer function (OTF) of the system.
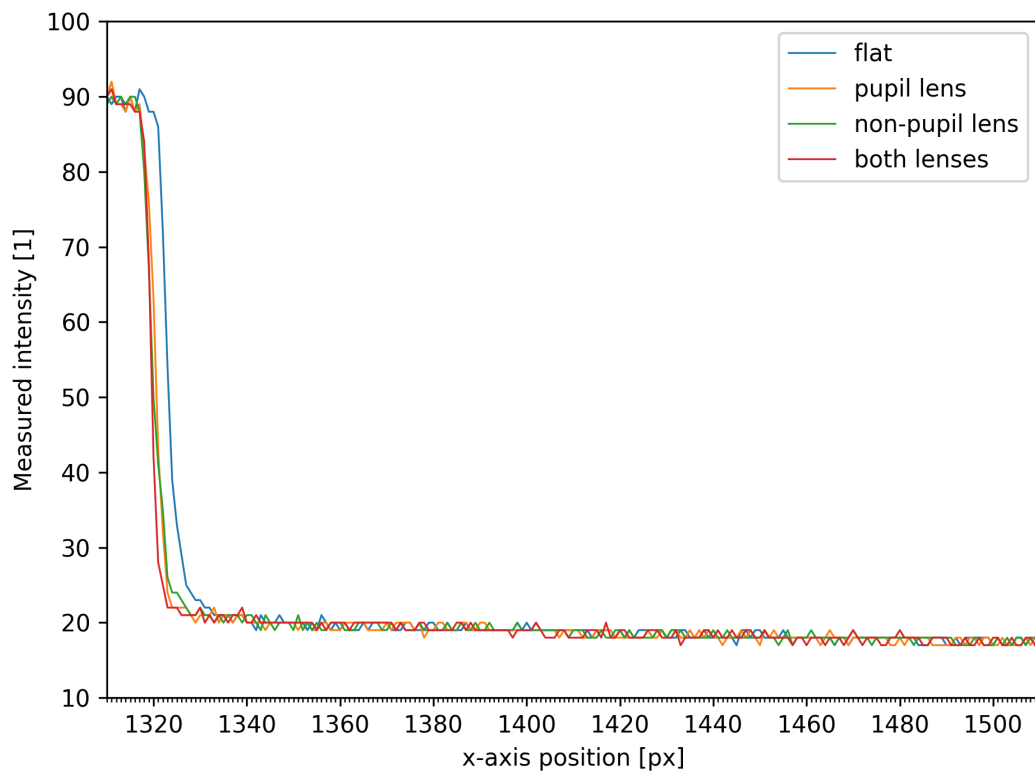
Figure 7.3: Example of edge spread function (ESF) experimental data in the edge differentiation method.

In order to improve the noise of the estimates, the resulting modulation transfer is recalculated 30 times, by translating the ESF estimation diagram position along the perpendicular axis in the $\delta y = [-15, 14]$ px range. Different OTF estimates are used to produce a mean estimate of the system; finally the modulation transfer function (MTF) is estimated by calculating the absolute value.

The method relies on the convolutional properties of aberration inducing optical system that creates images (let I the "perfect" image, i the resulting image after being convolved with the transfer function of the system m, C is a constant intensity rescaling dependent on the system):

$$i(x, y) = C \cdot I(x, y) * m(x, y)$$

The simple description of the method leads to:

$$\mathcal{F}[\frac{d}{dx} ESF(x)](k_x) = 2\pi k_x \left[\frac{1}{\sqrt{2\pi}} \frac{1}{i k_x} + \sqrt{\frac{\pi}{2}} \delta(k_x) \right] \cdot C \cdot \hat{m}(k_x)$$

which models the perfect edge as a Heaviside function $I(x, y) = H(x, y)$. The resulting expression gives the definition of the modulation transfer function:

$$\frac{|\mathcal{F}[\frac{d}{dx} ESF(x)](k_x)|}{\mathcal{F}[\frac{d}{dx} ESF(x)](0)} = \frac{|\hat{m}(k_x)|}{\hat{m}(0)} = MTF(k_x)$$

the edge shouldn't necessarily be centered, as the calculation of the Fourier-transformed $i(x, y)$ is just multiplied by a $e^{i k_x \Delta x_0}$ factor, which is not relevant with the following application of the absolute value.

7.2.3 Full image spectral MTF ratio estimation

The following analysis method estimates the correction contribute of the adaptive optics system by comparing the frequency content of the image rispect to a reference uncorrected case.

The images are prepared, by translating one of them to their relative center and cutting the common subregion (the cut is usually about $0 - 10$ px on both axes for a 1610×1010 px^2 image).

The images are transferred to the Fourier space; for each (k_x, k_y) value, the norm is calculated, followed by the normalization by the zero-frequency component; consequently, for each spatial frequency (k_x, k_y), the values of two images are divided.

The frequency space is resampled in circles of equal $|k| = \sqrt{k_x^2 + k_y^2}$ using $N_{bins} \approx 800$; the new value in $|k|$ is calculated as average of the logarithm of the values in (k_x, k_y) that belong the appropriate $|k|$-space partition.

A moving 20-sample average has been applied for an improved data visualization.

Mathematically, contribution of the optical system to the image quality is described as a convolution, as in the previous section:

$$i(x, y) = I(x, y) * m(x, y)$$

Two images of the same object, uncorrected and corrected, written in the Fourier space:

$$\hat{i}_1(k_x, k_y) = \hat{I}(k_x, k_y) \cdot \hat{m}_1(k_x, k_y)$$
$$\hat{i}_2(k_x, k_y) = \hat{I}(k_x, k_y) \cdot \hat{m}_2(k_x, k_y)$$

can be used to obtain:

$$q(k_x, k_y) = \frac{|\hat{i}_2(k_x, k_y)|/\hat{i}_2(0,0)}{|\hat{i}_1(k_x, k_y)|/\hat{i}_1(0,0)} = \frac{|\hat{m}_2(k_x, k_y)|/\hat{m}_2(0,0)}{|\hat{m}_1(k_x, k_y)|/\hat{m}_1(0,0)} = \frac{MTF_2(k_x, k_y)}{MTF_1(k_x, k_y)}$$

which gives means to calculate the relative modulation transfer function improvement.

7.3   USAF 1951 tip-tilt sample
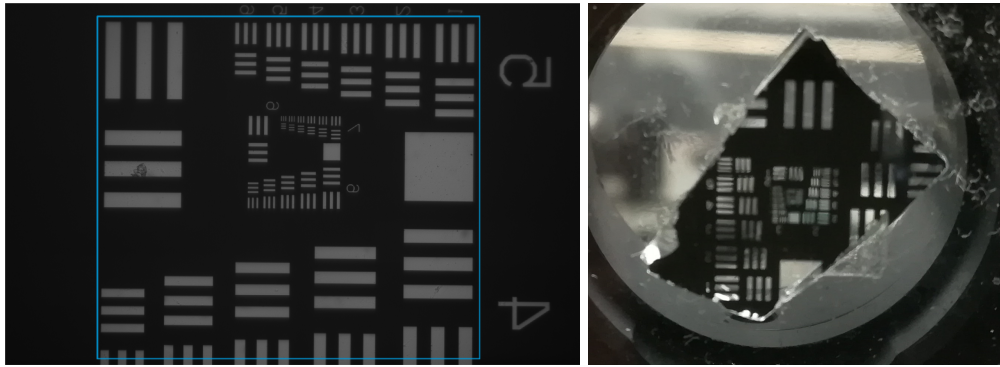
Figure 7.4: USAF 1951 test sample. On the left, the image of the sample through the microscopy setup on the camera, in blue the boundary of the zone on which the correction is applied; on the right, the sample itself.

The sample used in this experiment is a USAF 1951 target. Compared to biological microscopy samples, USAF 1951 provides features of different lengths as well as high contrast borders. These properties provide a clear visual feedback and a simpler evaluation of aberration effects. The available distances between the features go down to $4.39\,\mu m$ of the 7th group smallest element. In order to study the effects on the widefield correction we focused on the corner elements of the target images inside the field of view.

We have performed the measurement of the analysis set using the optical microscopy setup discussed in the previous sections; the set consists of images produced by tilting the USAF 1951 target sample by a specified angle difference respect to a zero point; the zero point location is closely located to the zero tilt angle. Five measurement sets with a linearly increasing tilt angle (5 tilt stage micrometric rotations) with steps of $0.98°$ over the vertical direction around the zero point; five measurement sets has been taken as well with steps of $1.16°$ over the horizontal direction.

For each measurement set the following adaptive optics correction conditions have been compared: calibration-set flat lenses (flat), pupil lens correction only (lens 1), non-pupil lens correction only (lens 2), two lenses correction.

The correction algorithm (Converge) follows the quadratic model optimization (subsection 4.3.3) over the Zernike modes of two lenses; specifically, the pupil lens 14 modes (up to 4th order) are optimized in order, following the mode ordering, then the procedure is repeated for the other lens; this loop is repeated for three times with decreasing amplitudes of modes limits; the maximum

Horizontal shift $\Delta\theta = -2.32°$	Pre (10^{-3})	Post (10^{-3})
Lens 1	13.86	14.44
Lens 2	13.84	14.30
Two lenses	13.83	14.85

Vertical shift $\Delta\theta = -1.96°$	Pre (10^{-3})	Post (10^{-3})
Lens 1	14.30	14.57
Lens 2	14.23	15.04
Two lenses	14.27	15.17

Horizontal shift $\Delta\theta = -1.16°$	Pre (10^{-3})	Post (10^{-3})
Lens 1	13.36	14.59
Lens 2	13.34	13.98
Two lenses	13.24	14.85

Vertical shift $\Delta\theta = -0.98°$	Pre (10^{-3})	Post (10^{-3})
Lens 1	13.76	14.70
Lens 2	13.78	14.44
Two lenses	13.69	15.20

Horizontal shift $\Delta\theta = 0.00°$	Pre (10^{-3})	Post (10^{-3})
Lens 1	14.31	14.79
Lens 2	14.21	14.63
Two lenses	14.28	14.92

Vertical shift $\Delta\theta = 0.00°$	Pre (10^{-3})	Post (10^{-3})
Lens 1	14.31	14.79
Lens 2	14.21	14.63
Two lenses	14.28	14.92

Horizontal shift $\Delta\theta = 1.16°$	Pre (10^{-3})	Post (10^{-3})
Lens 1	13.11	14.30
Lens 2	13.06	13.71
Two lenses	13.02	14.61

Vertical shift $\Delta\theta = 0.98°$	Pre (10^{-3})	Post (10^{-3})
Lens 1	13.35	14.59
Lens 2	13.36	14.28
Two lenses	13.34	14.82

Horizontal shift $\Delta\theta = 2.32°$	Pre (10^{-3})	Post (10^{-3})
Lens 1	13.10	13.94
Lens 2	13.10	13.70
Two lenses	13.00	14.39

Vertical shift $\Delta\theta = 1.96°$	Pre (10^{-3})	Post (10^{-3})
Lens 1	12.78	14.28
Lens 2	12.87	13.44
Two lenses	12.60	14.57

Table 7.1: Full correction zone metric function values; the metric function is the variance of the correction zone.

amplitude window semiwidth are respectively $0.60\,\mu m$, $0.36\,\mu m$ and $0.22\,\mu m$ for each iteration. The final wavefront for each lens is registered and used to evaluate the corrected aberrations during the process.

The lenses' modes after the execution of the algorithm are represented in Figure 7.5 - Figure 7.7 as interferograms, the corresponding Zernike mode amplitudes are in Figure 7.8 - Figure 7.11 and the zonal metric function correction is represented in Figure 7.12 - Figure 7.14. The values of the full image metric function values are reported in Table 7.1.

We analyse images in two ways in order to compare the effect of aberrations; for this, we implement multiple Python scripts to automatically perform the analysis (subsection 7.2.1, subsection 7.2.2, subsection 7.2.3) and visualize its results (Figure 7.17 - Figure 7.25, Figure 7.26 - Figure 7.30).

The first way takes into account the local effect of aberrations, measuring the effect on the sharpness of well defined features of the sample; the form of USAF 1951 target defines zones of complete illumination as well complete darkness, the analysis of the sharpness profile of the intermediate region allows to compare the degree of aberrations present. The image has been analysed in four visible corners of the USAF 1951 target using the edge differentiation method as described in subsection 7.2.2, obtaining estimations of the modulation transfer function (MTF) values.
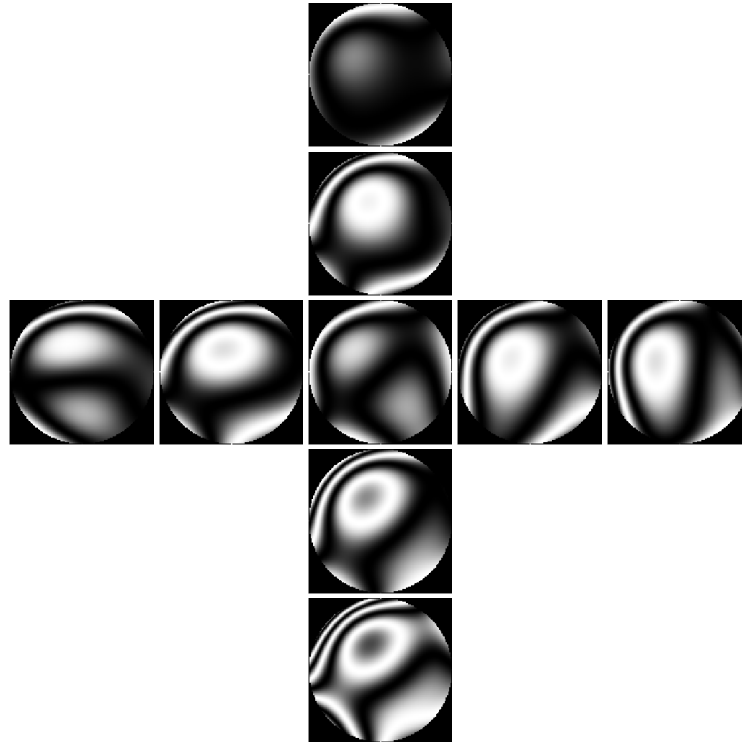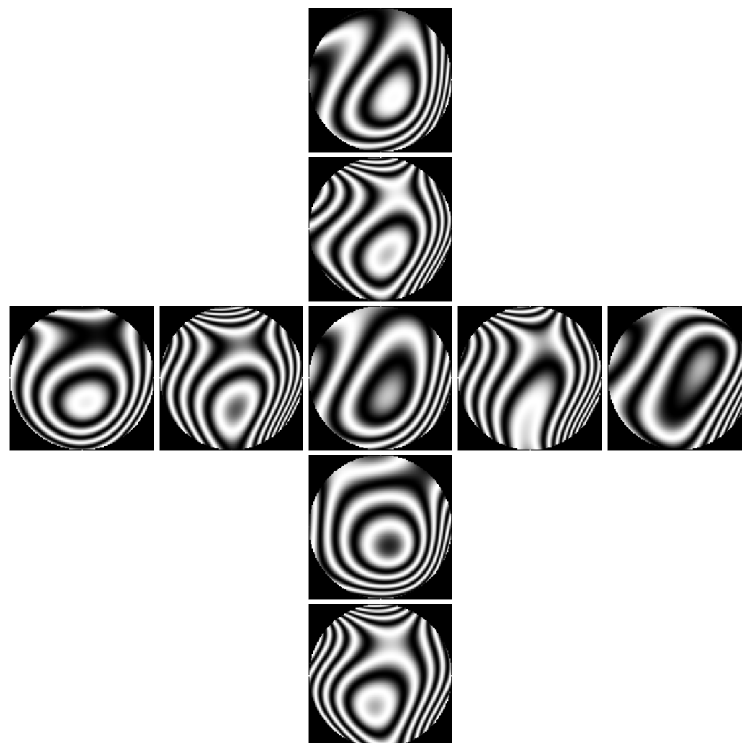
Figure 7.5: Interferograms of the wavefront of the pupil lens for different tilting angles; the correction has been performed using only the pupil lens. $\Delta\theta = 0.98°$ of angle difference between each figure in the vertical direction, $\Delta\theta = 1.16°$ in the horizontal direction.
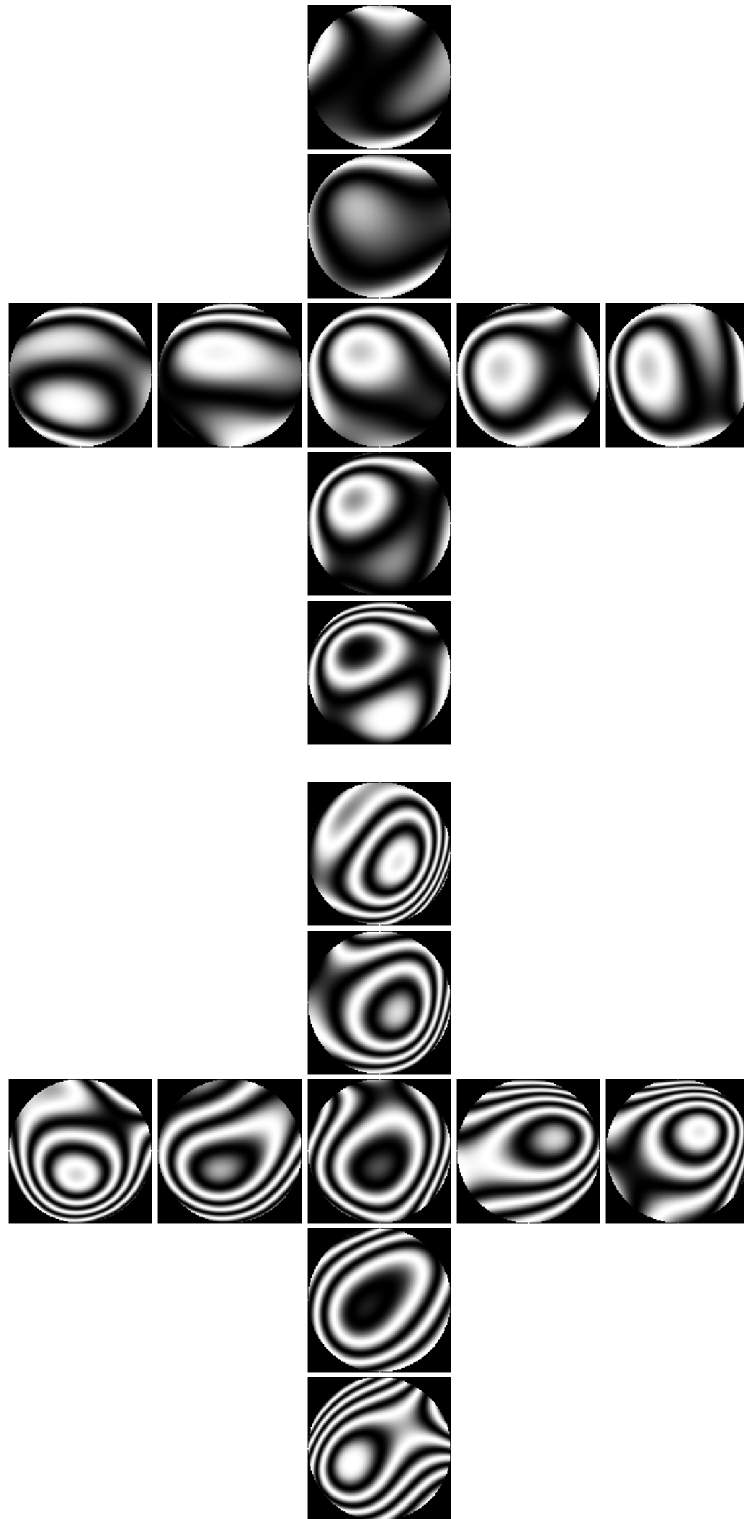

Figure 7.6: Interferograms of the wavefront of the non-pupil lens for different tilting angles; the correction has been performed using only the non-pupil lens. $\Delta\theta = 0.98°$ of angle difference between each figure in the vertical direction, $\Delta\theta = 1.16°$ in the horizontal direction.
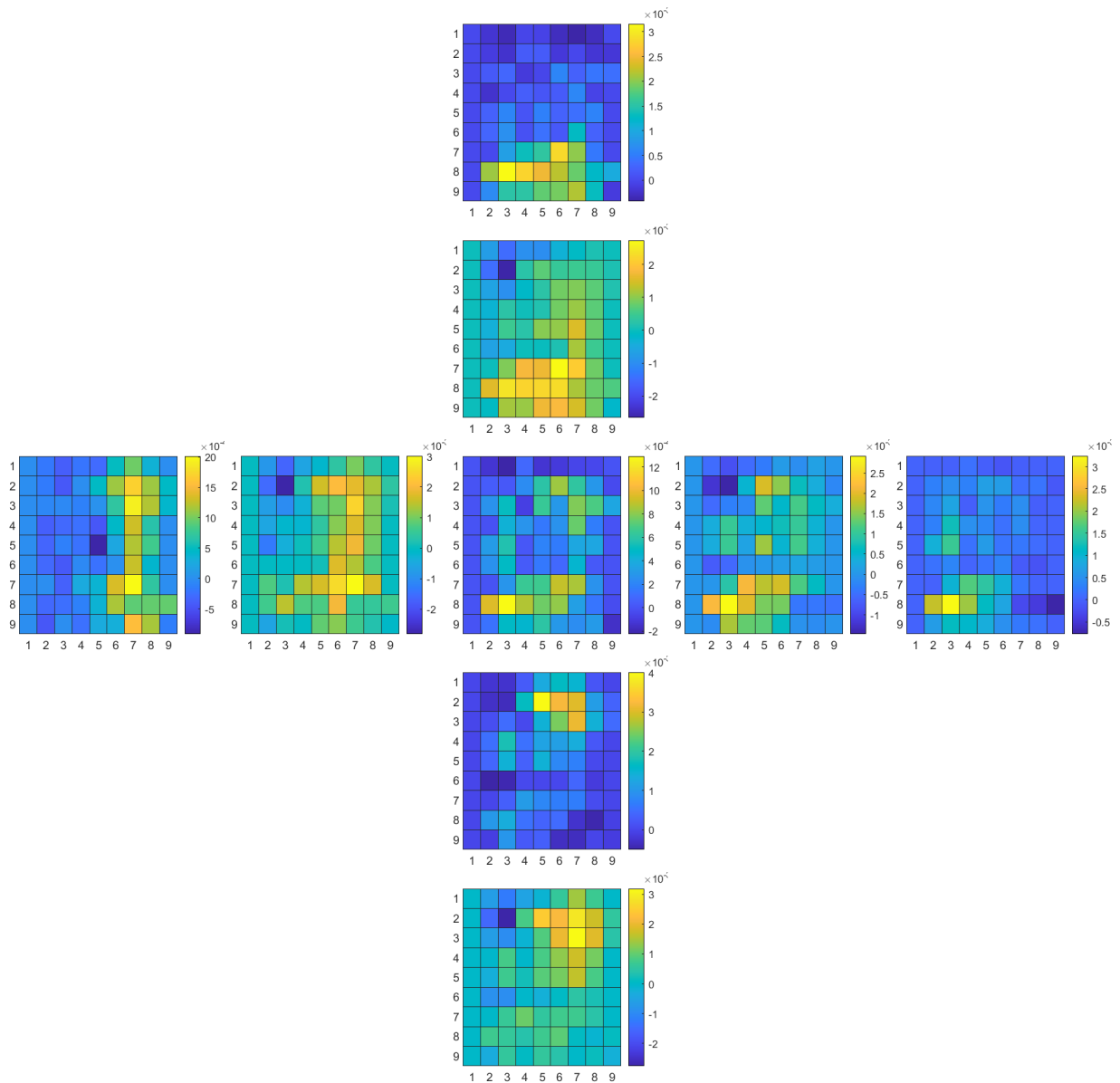
Figure 7.7: Interferograms of the wavefront of the pupil (above) and non-pupil lens (below) for different tilting angles; the correction has been performed using two deformable lenses together. $\Delta\theta = 0.98°$ of angle difference between each figure in the vertical direction, $\Delta\theta = 1.16°$ in the horizontal direction.
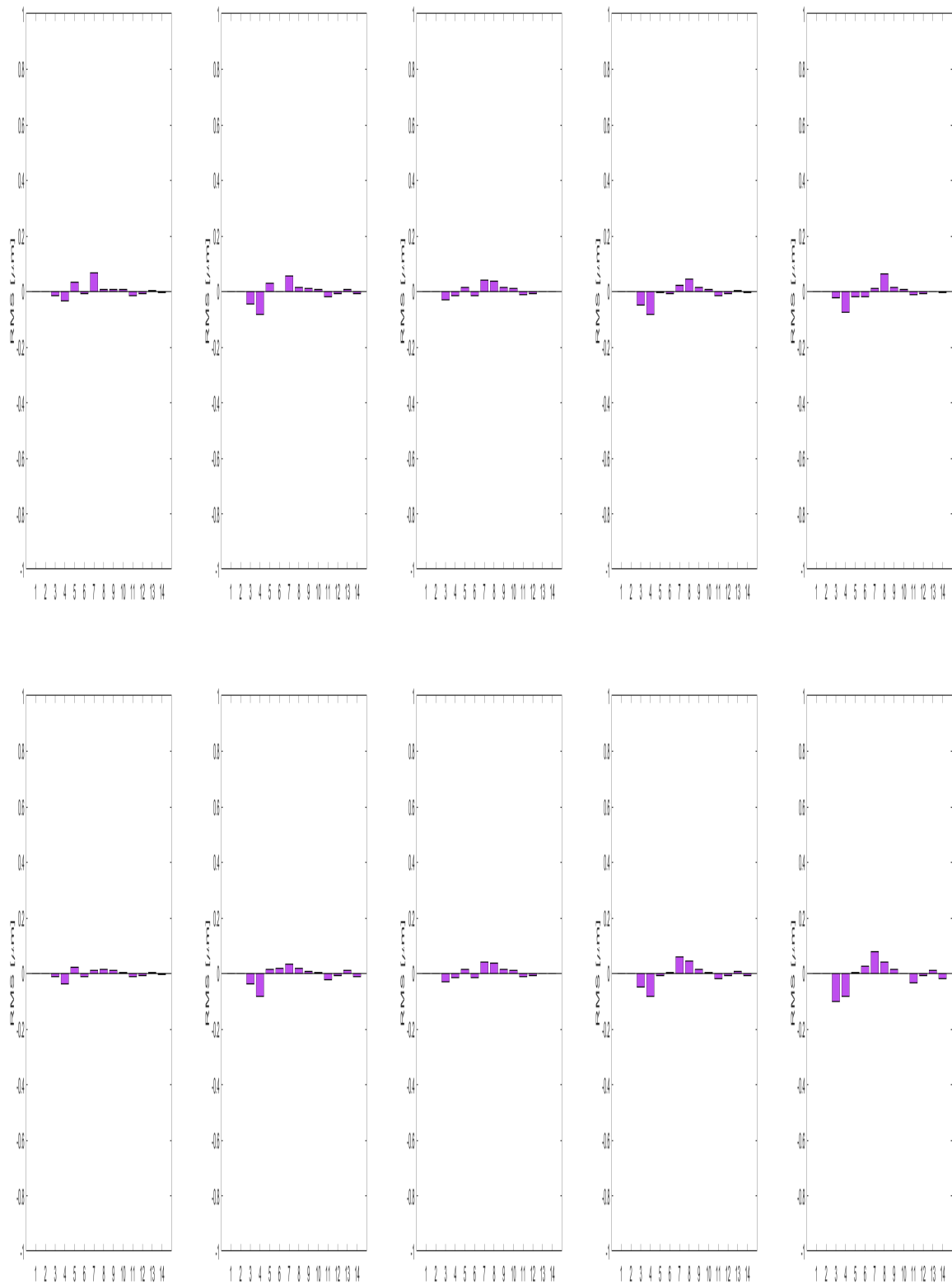
Figure 7.8: Modal bars of the pupil lens in the pupil only lens correction. Horizontal tilt with $\Delta\theta = 1.16°$ increment (above); vertical tilt with $\Delta\theta = 0.98°$ increment (below).
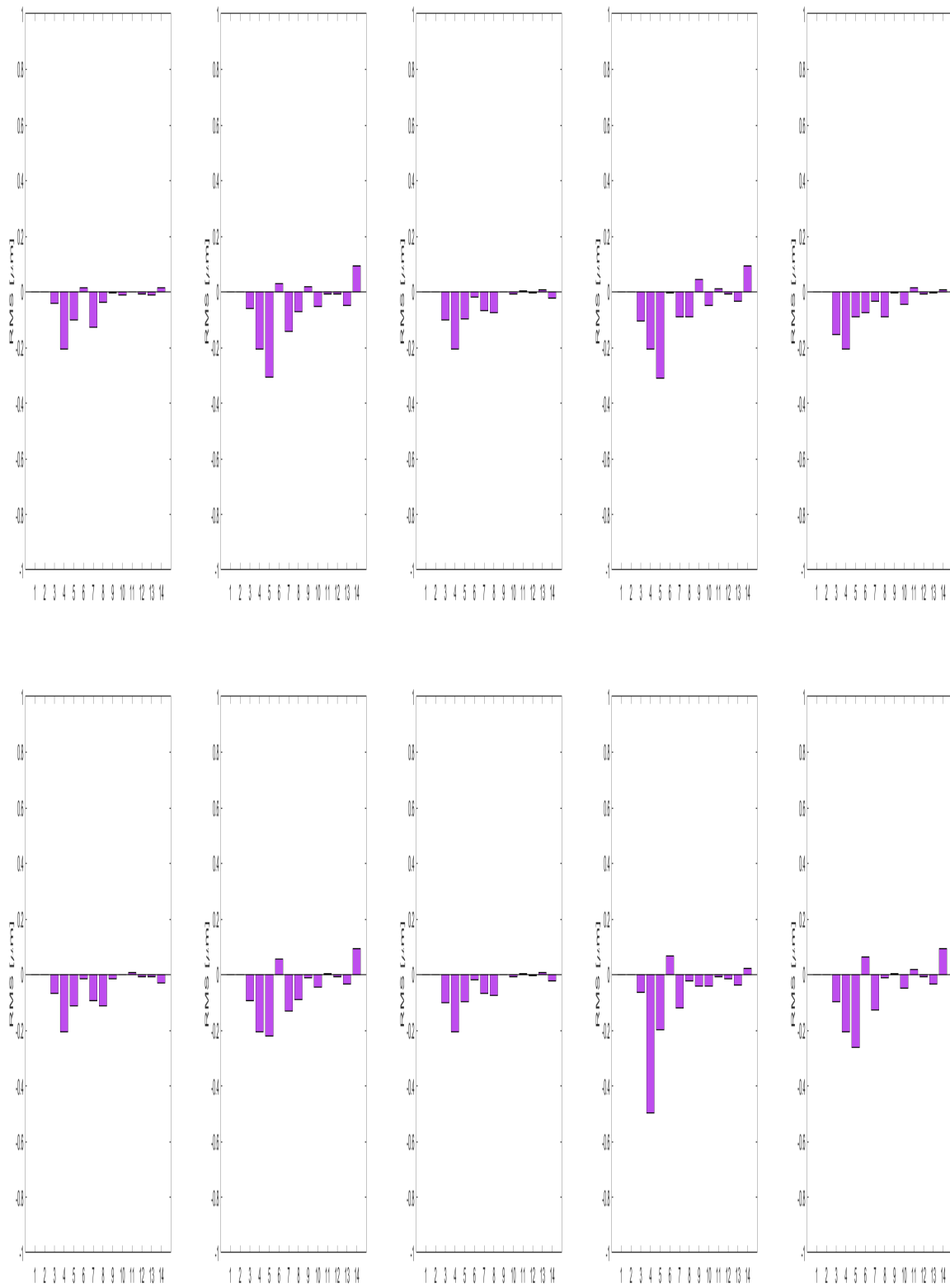
Figure 7.9: Modal bars of the non-pupil lens in the non-pupil only lens correction. Horizontal tilt with $\Delta\theta = 1.16°$ increment (above); vertical tilt with $\Delta\theta = 0.98°$ increment (below).

,
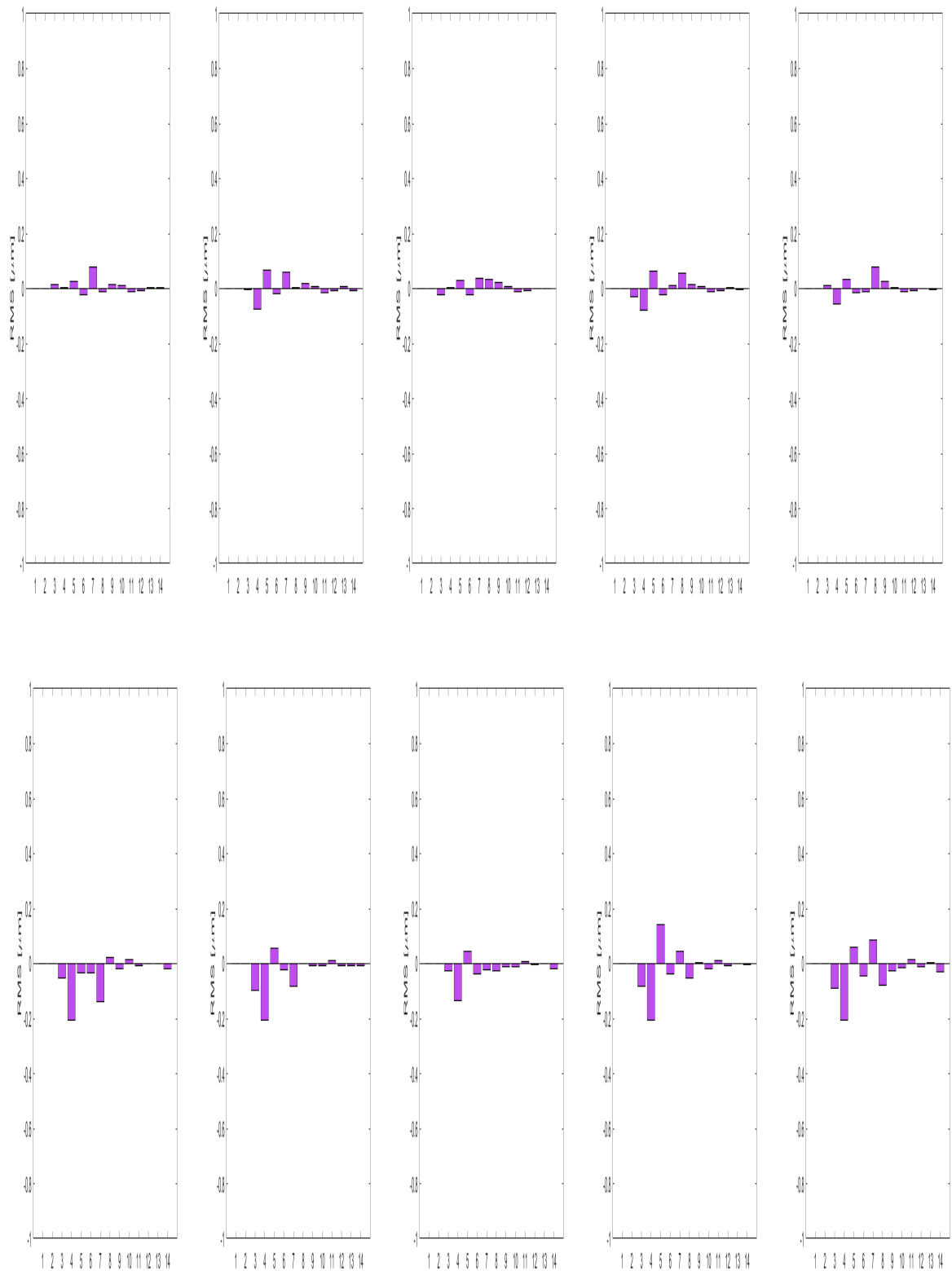
Figure 7.10: Modal bars in the two lenses correction. Horizontal tilt with $\Delta\theta = 1.16°$ increment; pupil lens modes (above), non-pupil lens modes (below).
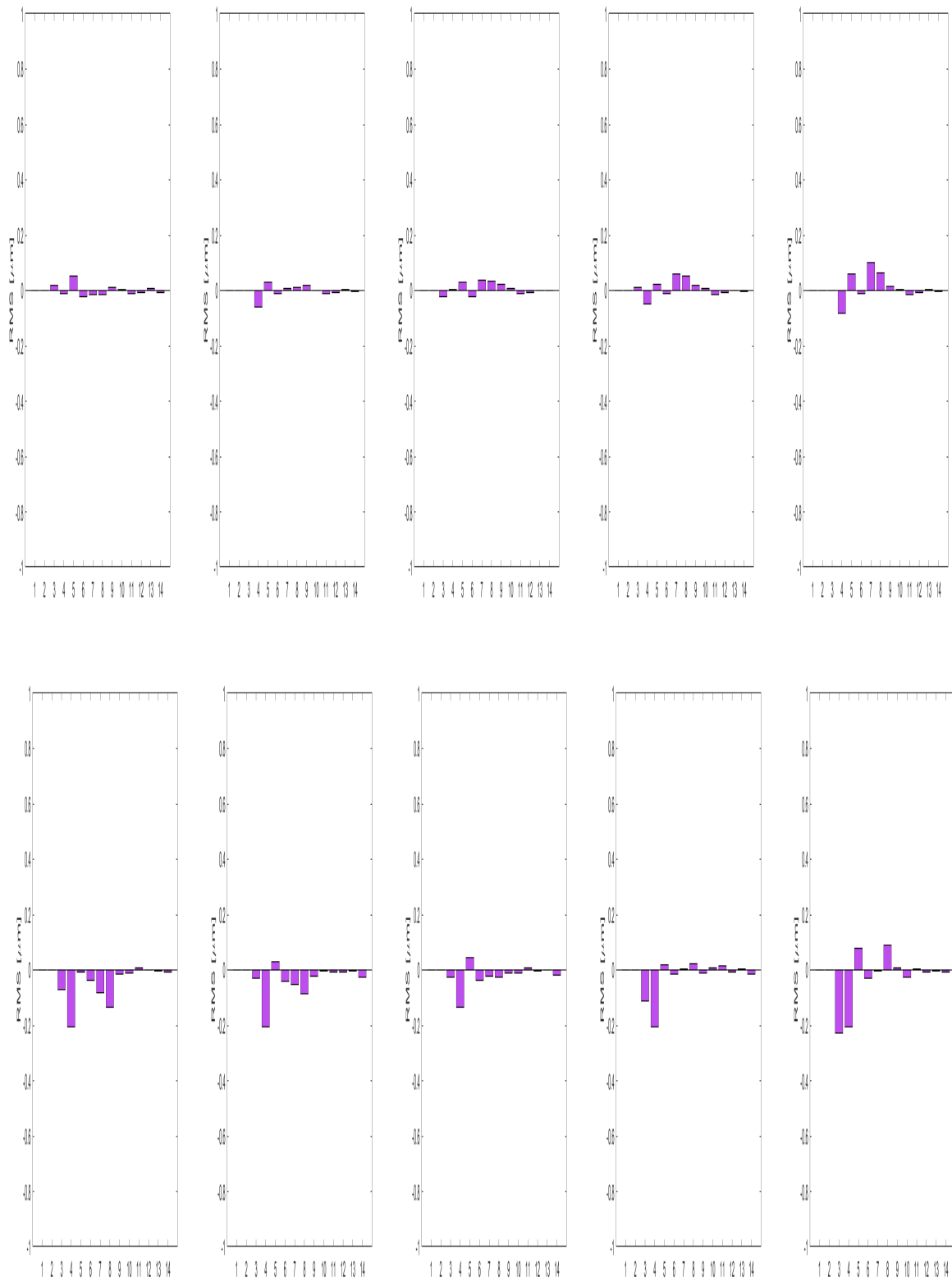
Figure 7.11: Modal bars in the two lenses correction. Vertical tilt with $\Delta\theta = 0.98°$ increment; pupil lens modes (above), non-pupil lens modes (below).
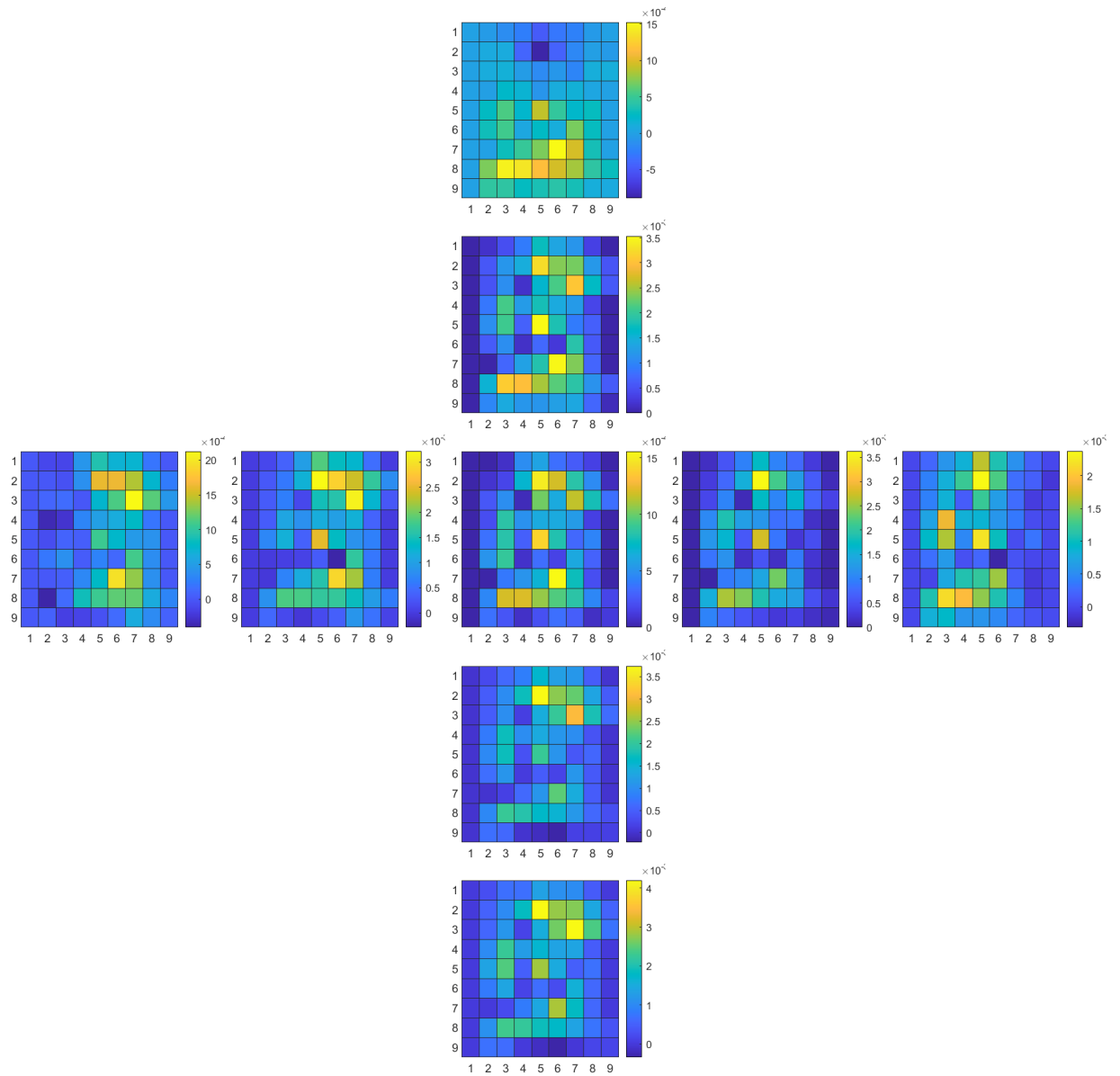
Figure 7.12: Widefield zonal matrices; each diagram shows the metric function change for different tilting angles comparing the post-corrected image with a pre-corrected one; the correction has been performed using only the pupil lens. $\Delta\theta = 0.98°$ of angle difference between each figure in the vertical direction, $\Delta\theta = 1.16°$ in the horizontal direction.

Figure 7.13: Widefield zonal matrices; each diagram shows the metric function change for different tilting angles comparing the post-corrected image with a pre-corrected one; the correction has been performed using only the non-pupil lens. $\Delta\theta = 0.98°$ of angle difference between each figure in the vertical direction, $\Delta\theta = 1.16°$ in the horizontal direction.
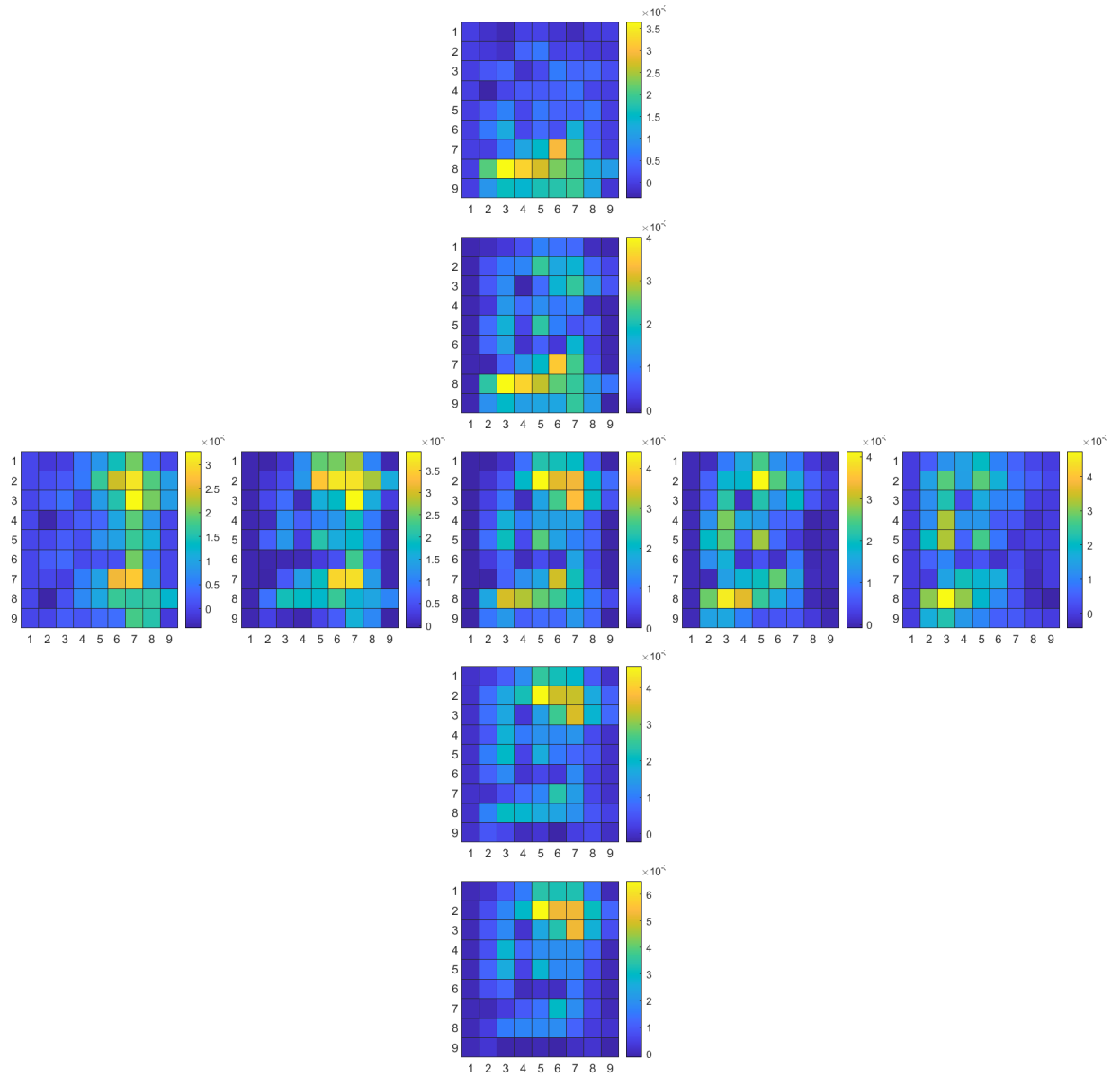
Figure 7.14: Widefield zonal matrices; each diagram shows the metric function change for different tilting angles comparing the post-corrected image with a pre-corrected one; the correction has been performed using two deformable lenses together. $\Delta\theta = 0.98°$ of angle difference between each figure in the vertical direction, $\Delta\theta = 1.16°$ in the horizontal direction.
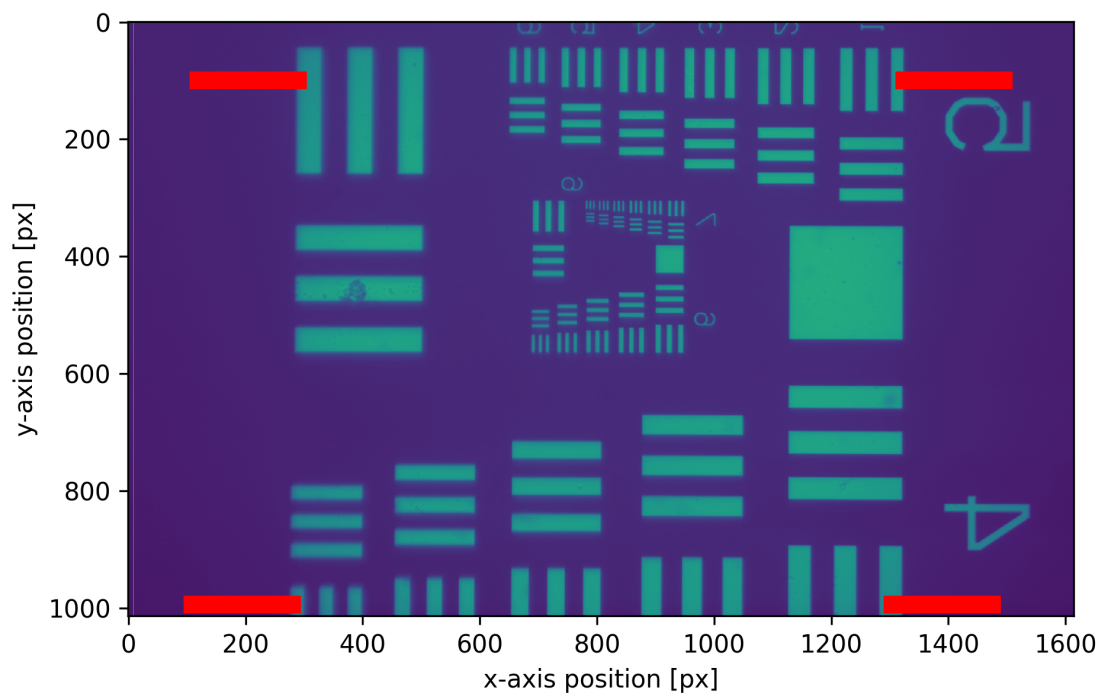
Figure 7.15: Edge differentiation method analysis example image; the edge profile has been analysed by considering a row of pixels, for all rows inside the red region, then averaged as described in subsection 7.2.2.
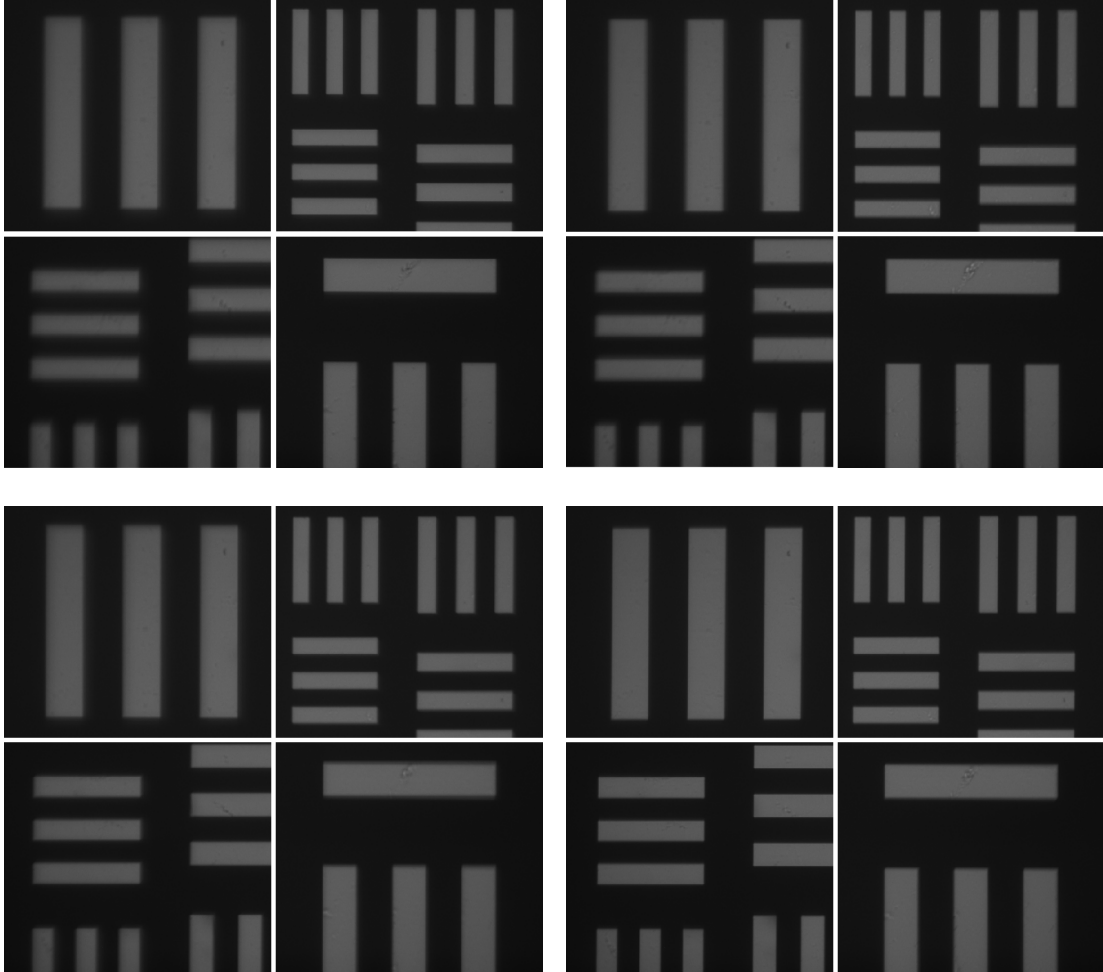
Figure 7.16: Example of USAF 1951 corner zones in different correction configurations (Horizontal $\Delta\theta = 2.32°$). Each group of four images represents each correction (flat, lens 1 only, lens 2 only, two lenses); inside one group, four corner zones of the image are visualized.

The second way analyses in the image globally by estimating the MTF ratio in the Fourier domain as described in subsection 7.2.3.

7.3.1 Analysis
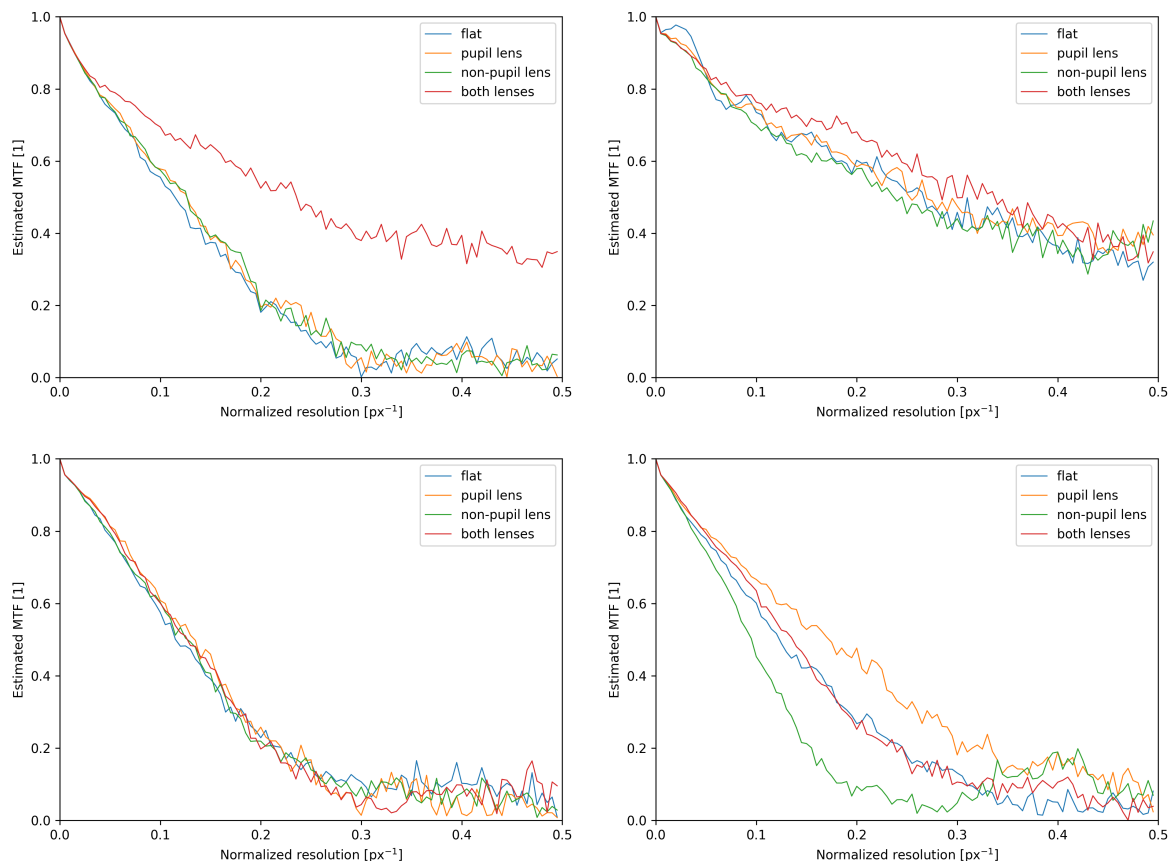
Figure 7.17: MTF, $\Delta\theta = 0°$ configuration. Each graph takes into consideration the corresponding corner on the USAF image (Figure 7.15).

The correction results are reported in form of graphs Figure 7.17 - Figure 7.25 concerning the differential edge analysis; while the global image MTF ratio is reported in Figure 7.26 - Figure 7.30.

7.3.2 Discussion

The interferograms of lens' modes after the correction are shown in Figure 7.5, Figure 7.6, Figure 7.7 as well as Figure 7.8, Figure 7.9, Figure 7.10, Figure 7.11 showing a monotonic variation of coma modes ($Z_3^{\pm 1}$) as function of the tilt angle in a specified direction; second order modes ($Z_2^{-2,0,+2}$) exhibit arbitrary values due to imperfect manual defocus adjustment; residual variations of higher order modes are found. This behaviour is observed in pupil lens only and both lenses of two lenses configurations. The expected behavior of the pupil lens case, shown in simulations, shouldn't have mode contributions, but monotonically varying coma ($Z_3^{\pm 1}$) modes are present; a possible explanation can be the presence of a non-uniform feature distribution over the field of view with a preference by the algorithm towards a specific optimization region, the additional modes, in theory locked by symmetries in the simulation, are used for the correction.
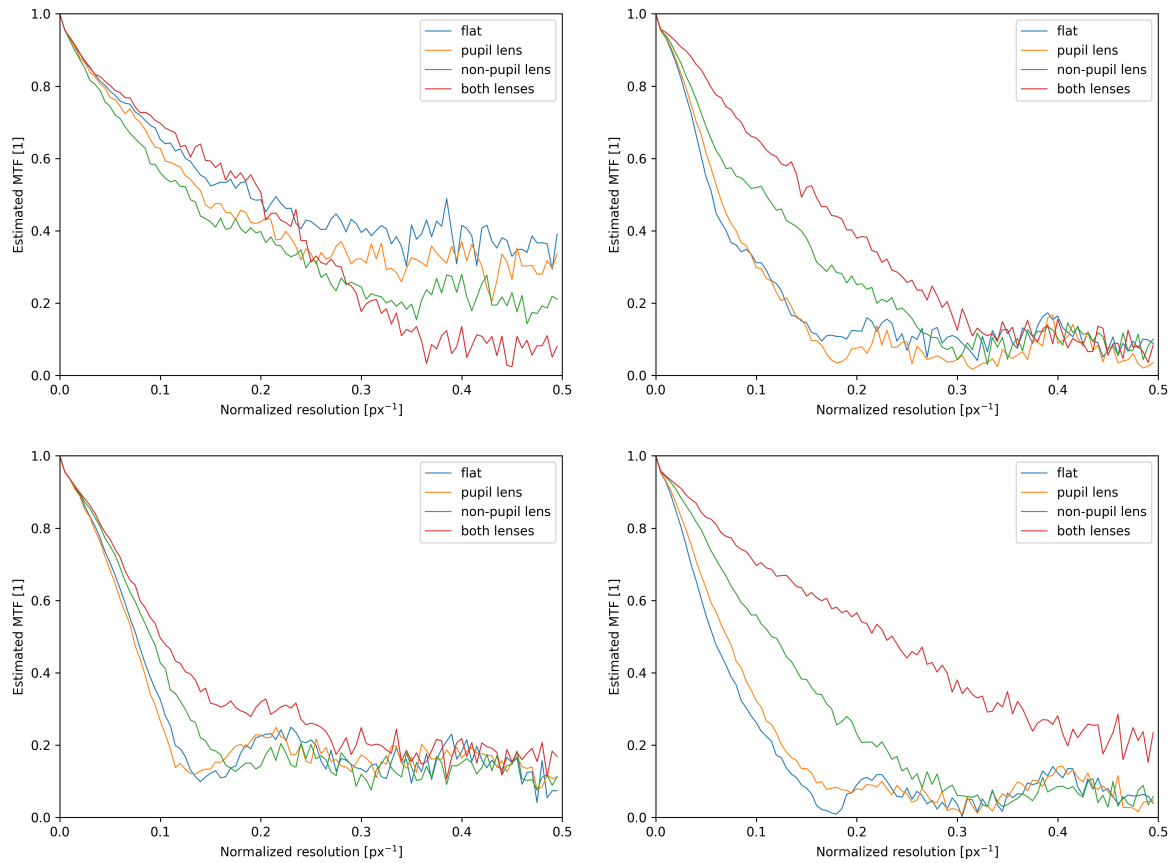
Figure 7.18: MTF, Horizontal $\Delta\theta = -2.32°$ configuration. Each graph takes into consideration the corresponding corner on the USAF image (Figure 7.15).
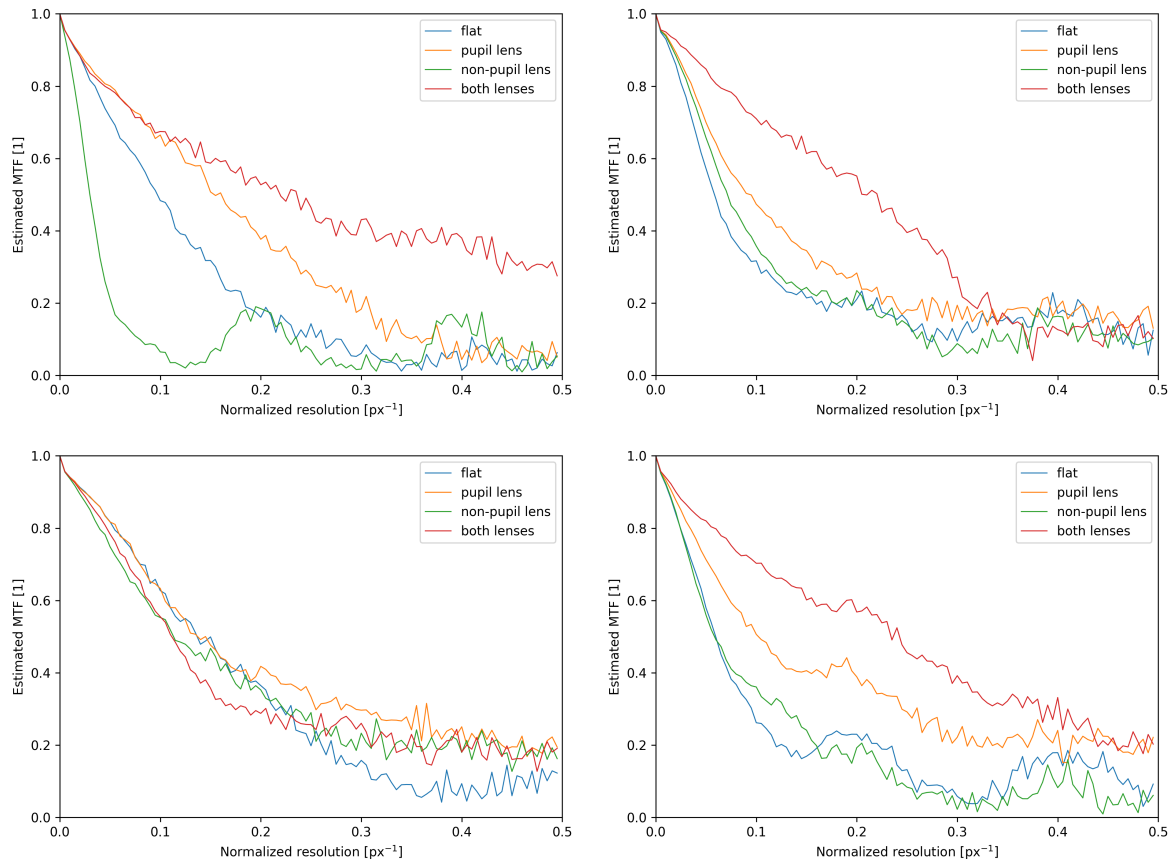
Figure 7.19: MTF, Horizontal tilt $\Delta\theta = -1.16°$ configuration. Each graph takes into consideration the corresponding corner on the USAF image (Figure 7.15).
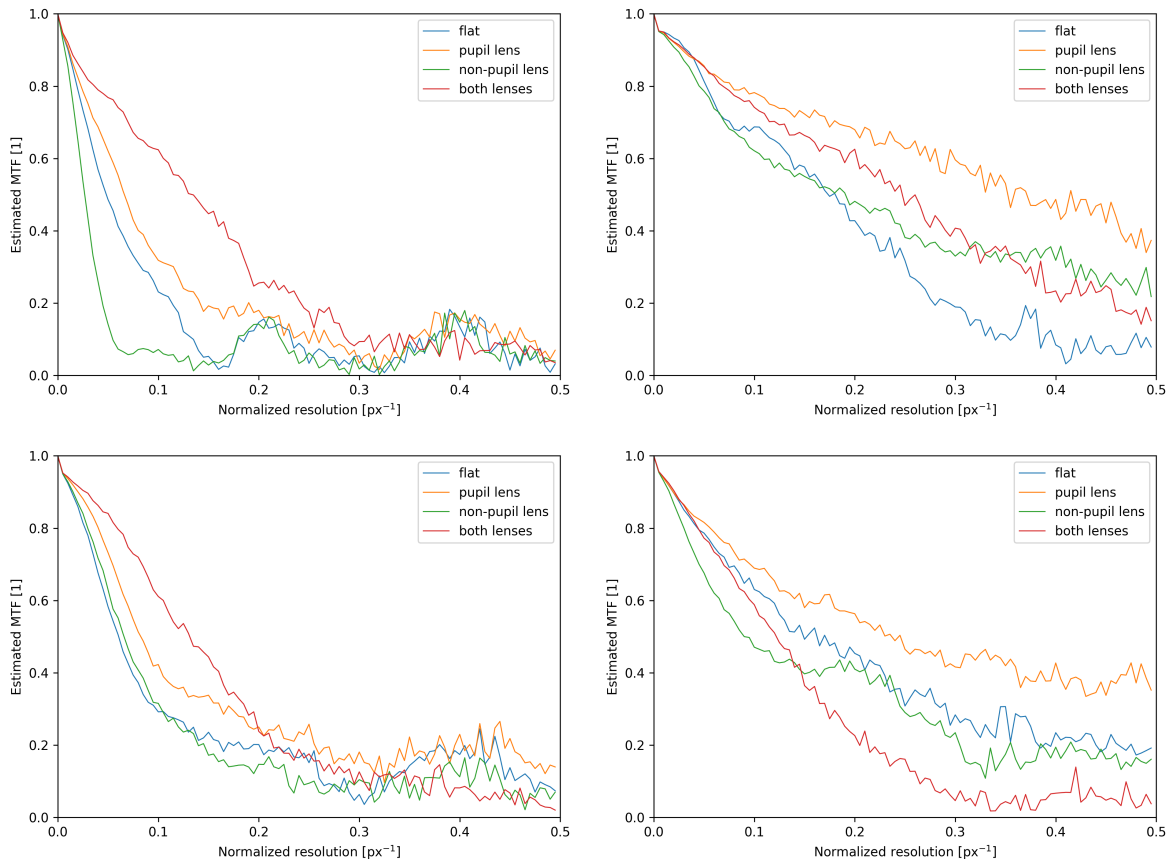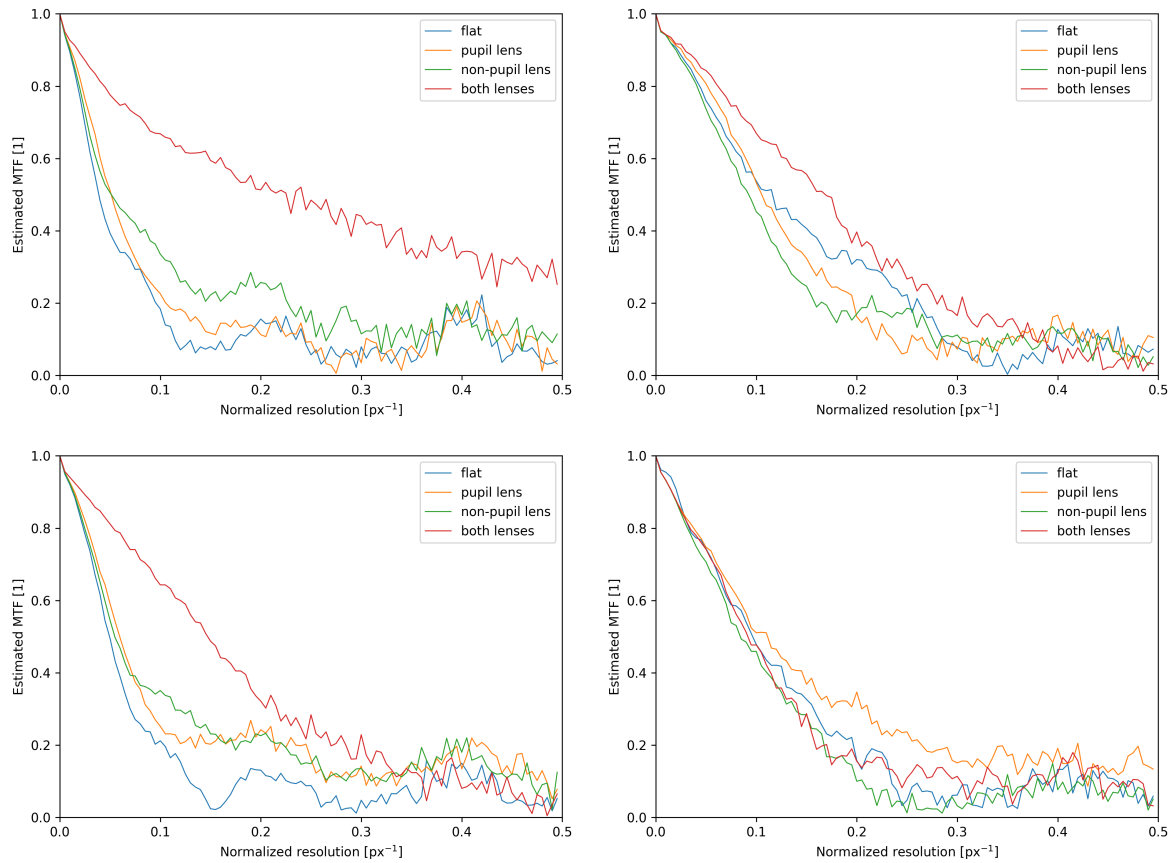
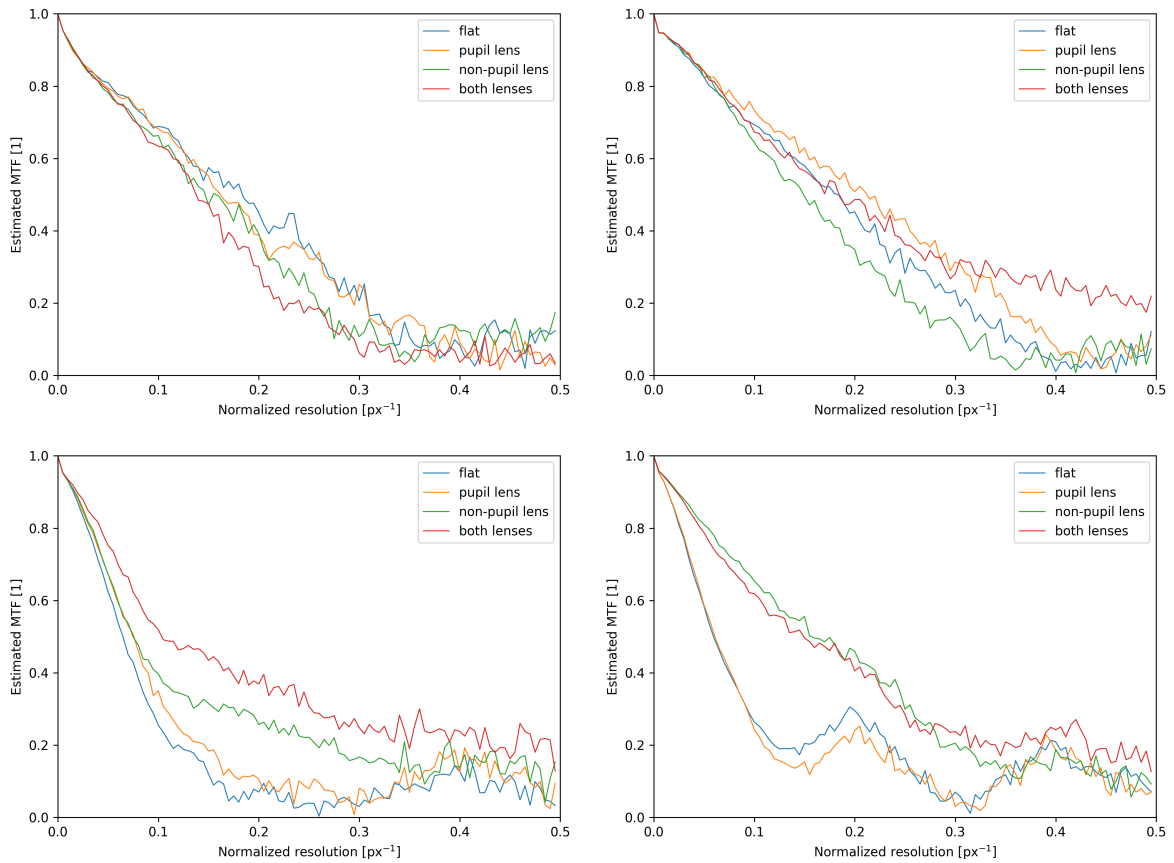Figure 7.20: MTF, Horizontal $\Delta\theta = 1.16°$ configuration. Each graph takes into consideration the corresponding corner on the USAF image (Figure 7.15).

Figure 7.21: MTF, Horizontal tilt $\Delta\theta = 2.32°$ configuration. Each graph takes into consideration the corresponding corner on the USAF image (Figure 7.15).

Figure 7.22: MTF, Vertical $\Delta\theta = -1.95°$ configuration. Each graph takes into consideration the corresponding corner on the USAF image (Figure 7.15).
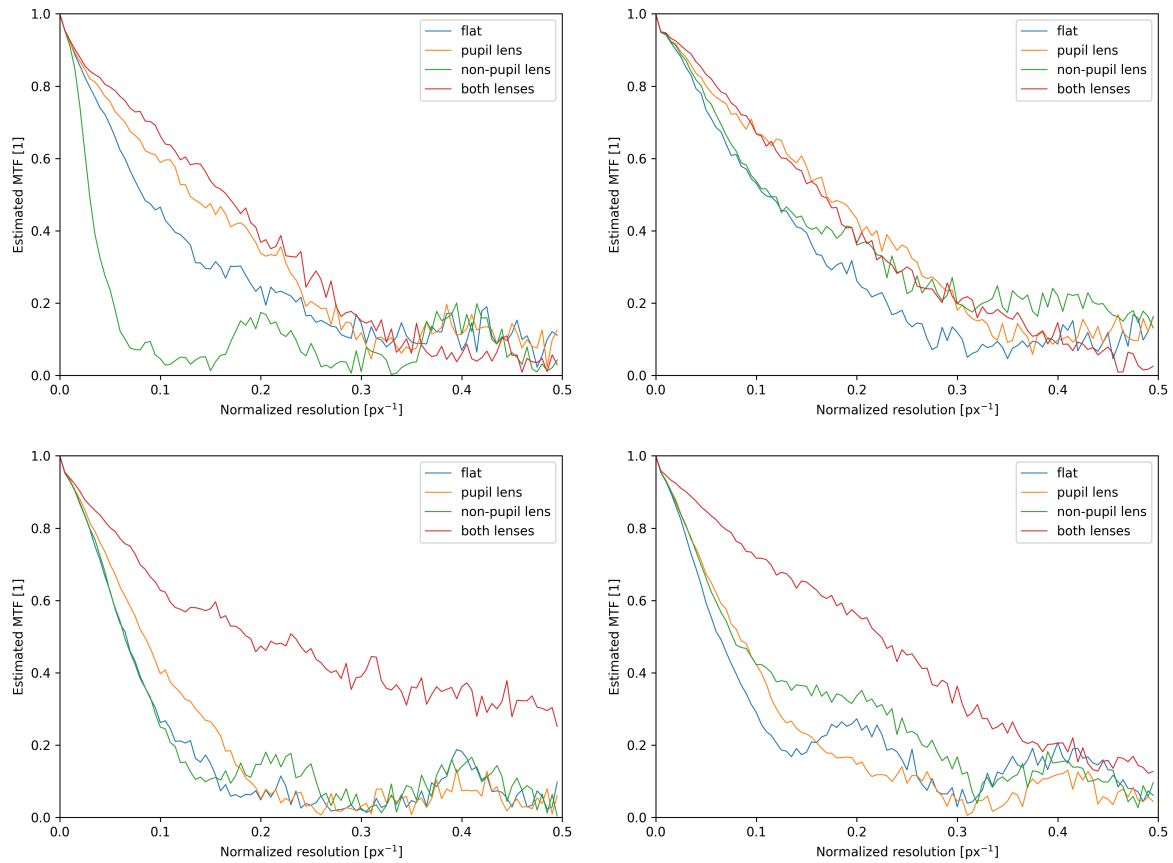
Figure 7.23: MTF, Vertical tilt $\Delta\theta = -0.98°$ configuration. Each graph takes into consideration the corresponding corner on the USAF image (Figure 7.15).
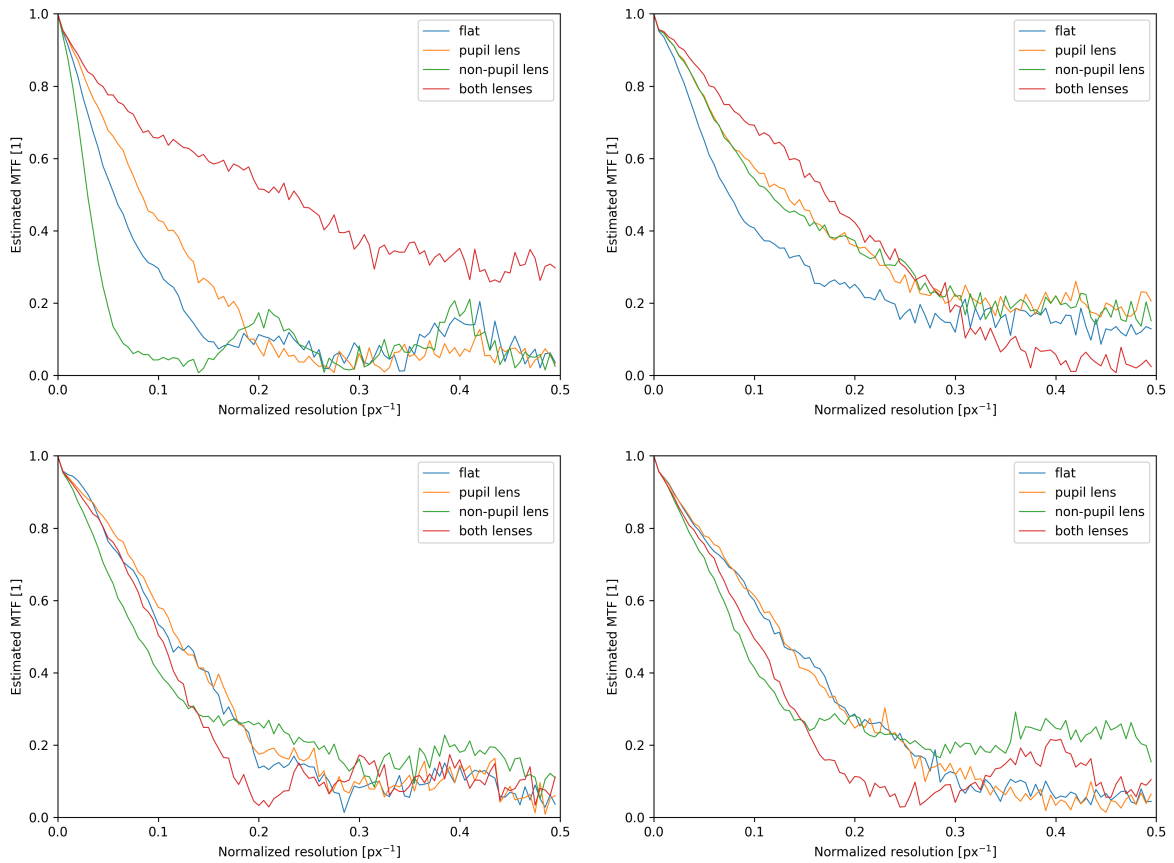
Figure 7.24: MTF, Vertical $\Delta\theta = 0.98°$ configuration. Each graph takes into consideration the corresponding corner on the USAF image (Figure 7.15).
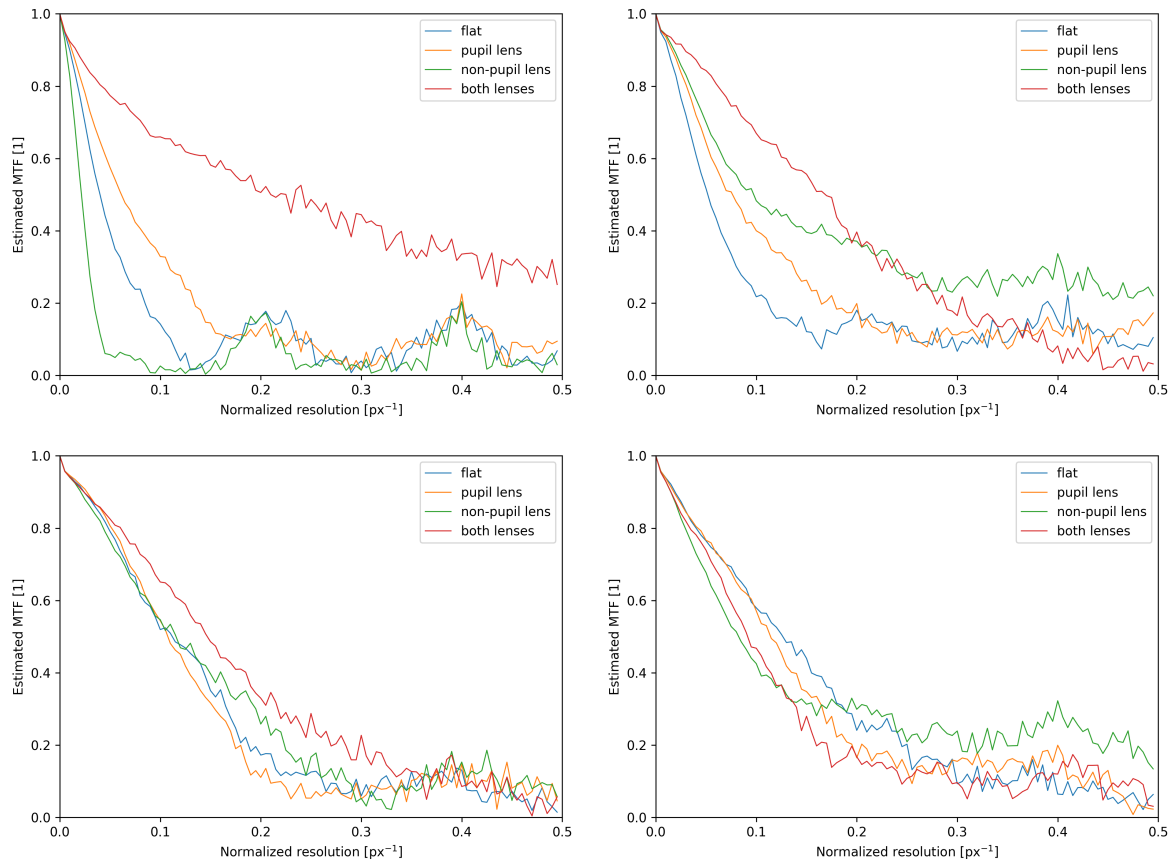
Figure 7.25: MTF, Vertical tilt $\Delta\theta = 1.95°$ configuration. Each graph takes into consideration the corresponding corner on the USAF image (Figure 7.15).
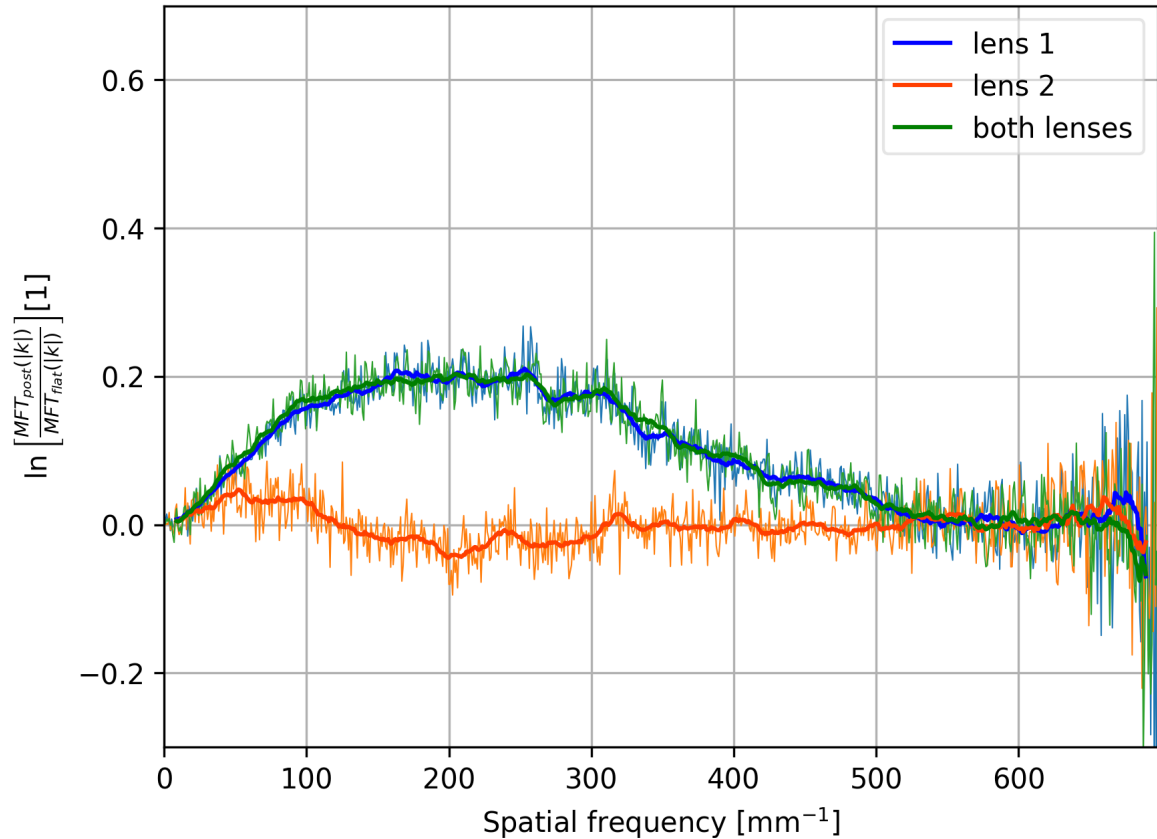
Figure 7.26: Full image MTF ratio, $\Delta\theta = 0°$ configuration.

Edge differentiation method

The analysis through the edge differentiation method shows a strong MTF increase for the two lenses correction compared to the flat case, even though the improvement is not consistent when evaluated over the full widefield image and results in an MTF decrease in a multiple cases (for example Figure 7.24) in one of the zones; the improvement is seen in three corners of the image of four in almost all cases. The estimate of MTF in case of a successful correction corresponds to $0.5 - 0.6$ for $1/5$ of the spatial sampling frequency.

The correction done by the pupil lens only case is more consistent even when evaluated respect to the flat case but overall the MTF increase is much less evident compared to the case of two lenses.

The estimate of MTF is considered for frequencies less than 0.25 the spatial sampling frequency of pixels due to the increasingly high levels of noise.

Full image MTF ratio estimation

Regarding the results of the full image MTF ratio estimation, an increase of spatial frequency components up to $500\,\mathrm{mm}^{-1}$ has been found; the most relevant improvement is registered in the $50-400\,\mathrm{mm}^{-1}$ spatial frequency range ($710\,\mathrm{mm}^{-1}$ corresponds to the half spatial sampling frequency the object imaged by the setup), corresponding to features in the $2.5 - 20\,\mathrm{\mu m}$ range.

The correction with the non-pupil lens results to be inconsistent; the behaviour is confirmed by the full image MTF ratio evaluation over different configurations, where the amplitude of spatial

frequencies is decreased $(100 - 350\,\text{mm}^{-1}$ range) respect to the flat case, as well as the direct examination of output images which show a strong decrease of sharpness in large region of the image.

The MTF ratio in the spatial frequency domain shows an improvement of the two lenses configuration compared to the only pupil lens one, quantifiable in a $5-10\%$ MTF increase over a $50-400\,\text{mm}^{-1}$ frequency range. The MTF ratio improvement between the pupil lens correction and the flat case is overall about 25% in the spatial frequency range of $100 - 350\,\text{mm}^{-1}$ up $500\,\text{mm}^{-1}$.
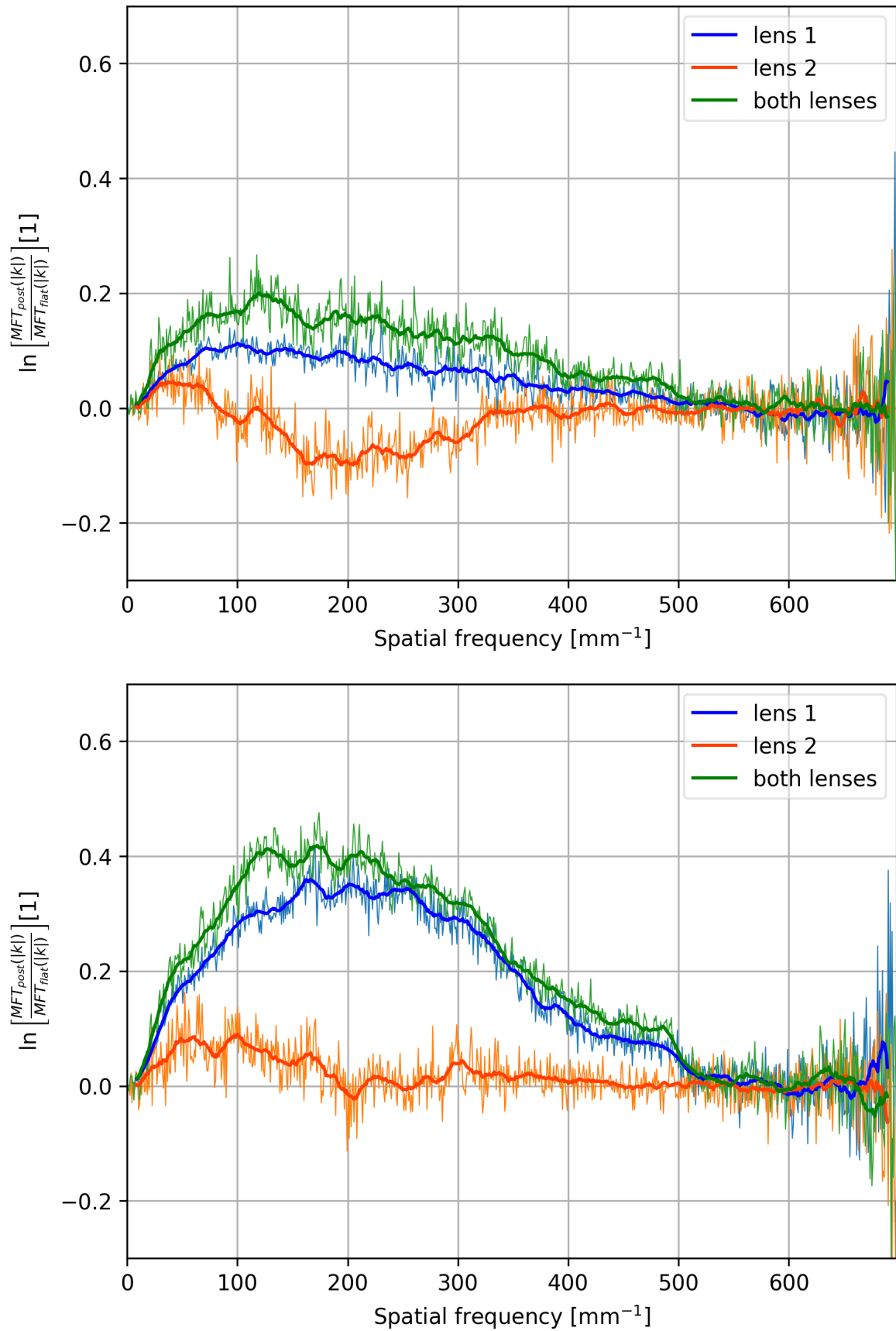
Figure 7.27: Full image MTF ratio, horizontal $\Delta\theta = -2.32°$ (above) and $\Delta\theta = -1.16°$ (below) sample tilt configurations.
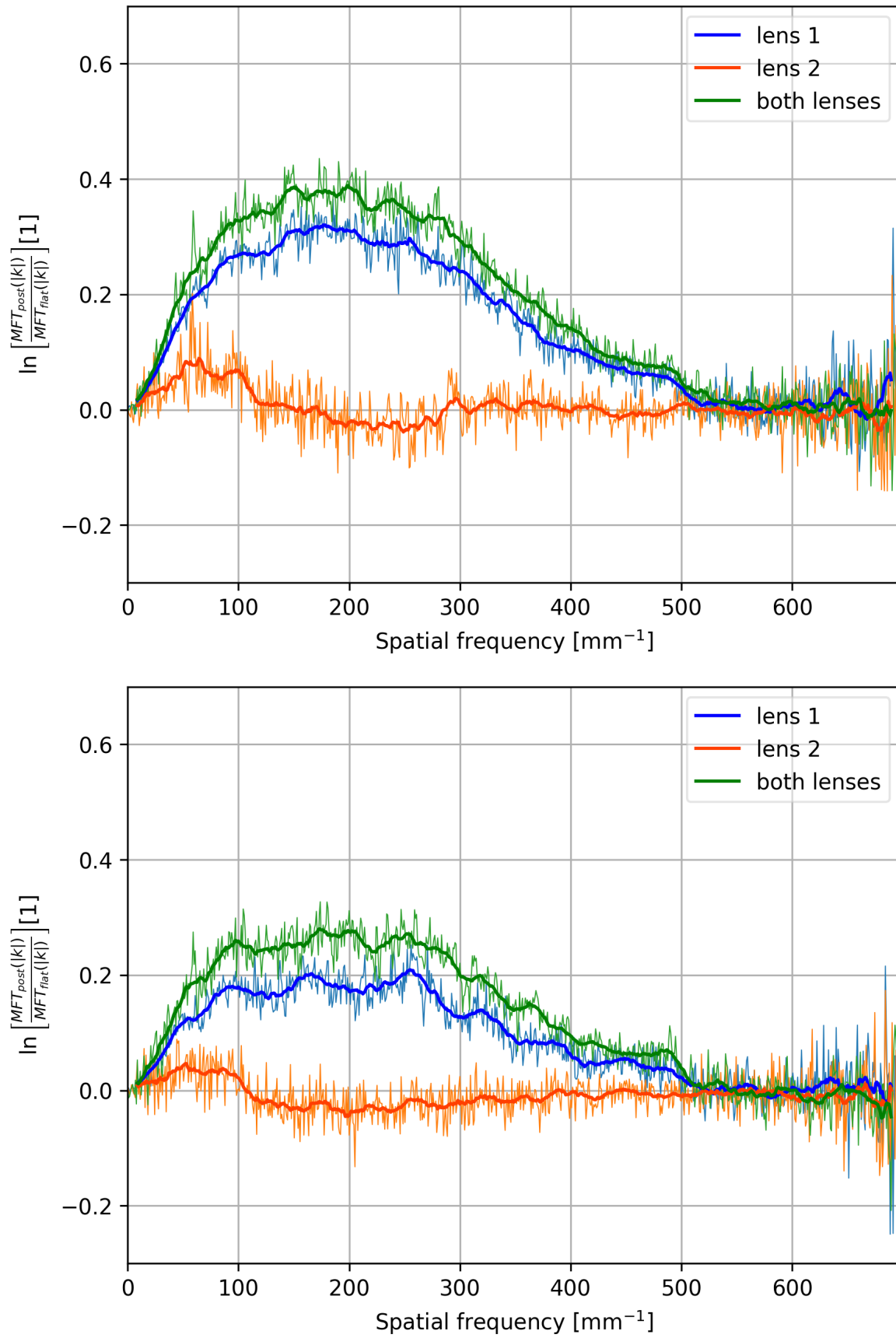
Figure 7.28: Full image MTF ratio, horizontal $\Delta\theta = 1.16°$ (above) and $\Delta\theta = 2.32°$ (below) sample tilt configurations.

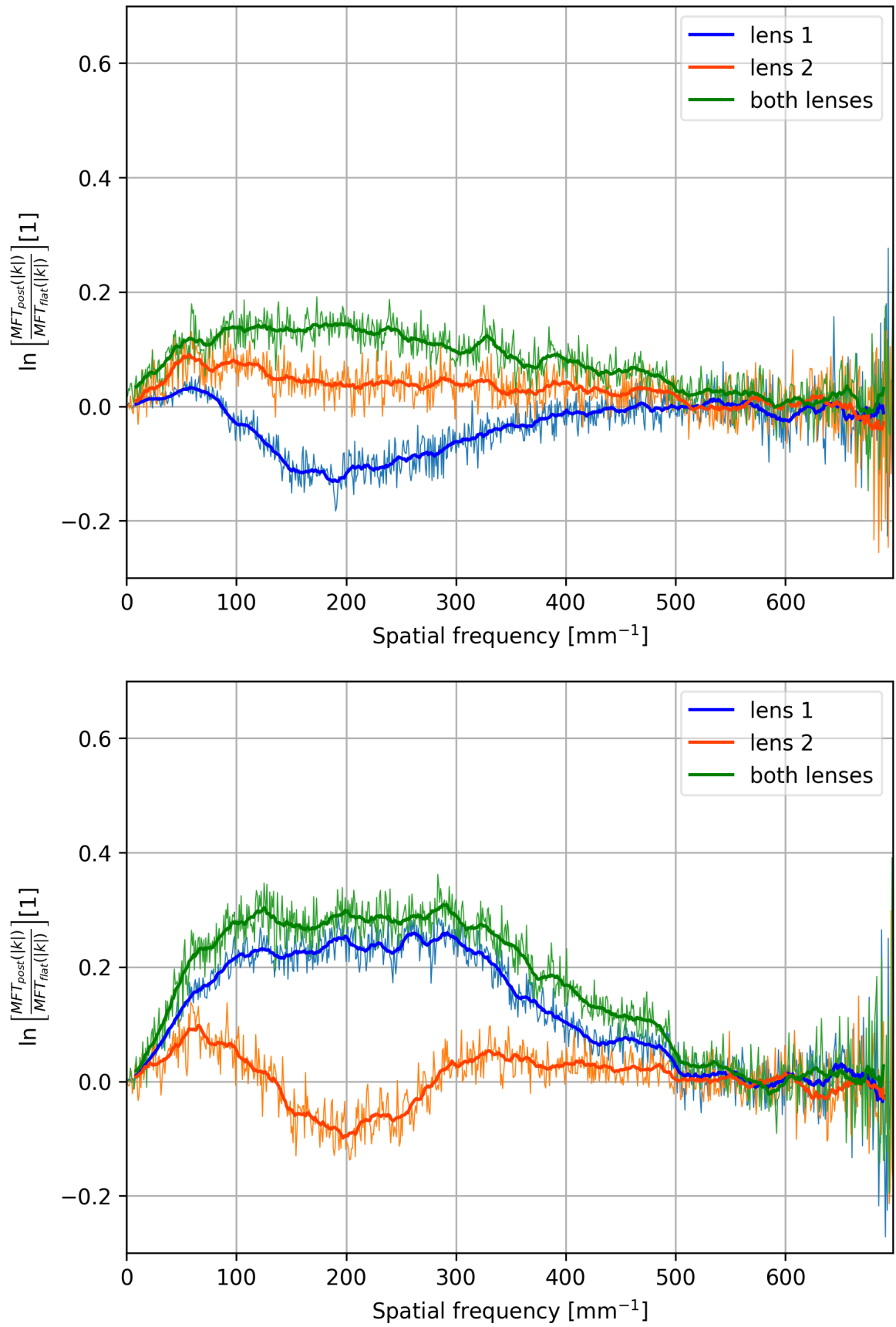Figure 7.29: Full image MTF ratio, vertical $\Delta\theta = -1.95°$ (above) and $\Delta\theta = -0.98°$ (below) sample tilt configurations.

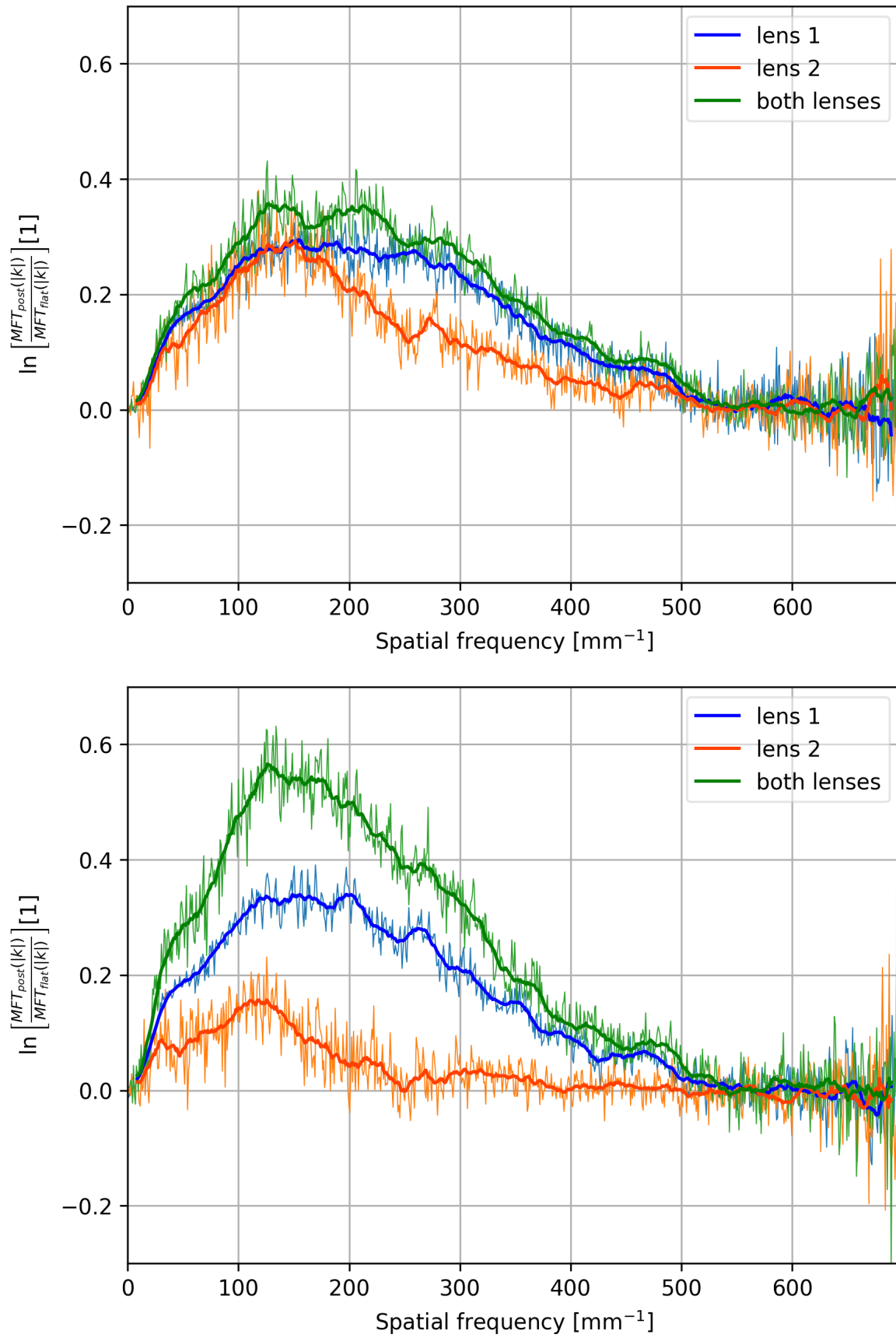Figure 7.30: Full image MTF ratio, vertical $\Delta\theta = 0.98°$ (above) and $\Delta\theta = 1.95°$ (below) sample tilt configurations.

Chapter 8

Conclusions

The adaptive optics correction system based on two deformable lenses, with capability to correct up to the 4th Zernike order modes, has been used in order to improve the quality of images generated in a widefield microscopy setup, using a USAF 1951 target as the sample.

The tilting of the sample case has been experimentally measured and studied using flat, pupil lens, non-pupil lens and two lenses configurations. The widefield setup is simulated, expecting no aberrations in case of pupil lens only case and the presence of coma $(Z_3^{\pm 1})$ aberrations in case two lenses correction, with a 20% aberration RMS decrease (Figure 6.1c).

Experimental measurements result in a consistent monotonic variation of coma $(Z_3^{\pm 1})$ modes for both pupil lens (Figure 7.5 and Figure 7.8), and two lenses configurations (Figure 7.7, Figure 7.10, Figure 7.11) for an increasing tip / tilt angle of the sample together with an inconsistent variation of second order modes (defocus and astigmatisms $Z_2^{0,\pm 2}$).

The image quality has been studied by estimating the modulation transfer function (MTF) locally, using sharpness proprieties of the USAF 1951 target, and globally, by analysing the spatial spectral content of images and evaluting MTF ratios compared to flat configurations.

The local analysis shows a consistent behaviour for the pupil lens configuration, while a stronger but incomplete widefield correction in case of two lenses (one corner of four corners suffers from a decrease of MTF compared to the flat configuration).

The global analysis indicates the pupil lens configuration receives a correction of 25% MTF increase compared to the flat configuration for spatial frequency components in a range of $100 - 350\,\mathrm{mm}^{-1}$ with an improvement up to $500\,\mathrm{mm}^{-1}$; the relevant corrected modes result to be astigmatisms $(Z_2^{\pm 2})$, defocus (Z_2^0) and comas $(Z_3^{\pm 1})$, as described by the lens' modes. Two lenses configuration gives an additional $5 - 10\%$ MTF over the pupil lens configuration over the same spatial frequency range; same type of aberrations is corrected in case of both lenses (Figure 7.27 - Figure 7.30).

The simulation of the Petzval curvature indicates the introduction of defocus mode (Z_2^0) for the pupil lens configuration; for the two lenses case, two lenses compensate each other defocus modes while produce additional spherical aberration modes (Z_4^0); the spherical aberration additional effect is weak and doesn't guarantee a low aberration RMS in the central part of the field; a reduced correction field (5/9 the field of view radius) results in a stronger effect of the second lens and a improved correction of central part of the field of view, amounting to the double corrected area.

Related to the experimental goal to this work, the results show that:

- the two lenses configuration results in agreement with simulations, displaying monotonically varying coma modes on both lenses; the correction using single pupil lens shouldn't produce modes, but coma ($Z_3^{\pm1}$) aberrations are observed; in both cases spurious second order modes ($Z_2^{0,\pm2}$) are detected;

- the correction using two lenses performs better than the single pupil lens in terms of the spectral content over the whole field of view, as in the global image analysis, showing a improvement of $5 - 10\%$ over a spatial frequency range of $100 - 350\text{mm}^{-1}$ and a positive improvement up to 500mm^{-1}; the correction shown at the corners of the field of view by the local image analysis is not complete for the two lenses compared to the single pupil lens system and 3 of 4 corners are improved in most cases; the variation ranges from a similar to greatly improved MTF values.

Appendix A

Appendix

A.1 Rayleigh-Sommerfield integral (free light propagation)

A precise description of the light propagation in diffractive terms is given by Kirchhoff, which was made mathematically consistent using the formulation by Rayleigh and Sommerfield.

In order to find the expression of the propagating scalar electric field $E(\bar{r})$ we start by writing Helmholtz equation

$$(\nabla^2 + k^2)E(\bar{r}) = 0, \quad k = \frac{\omega}{c} \tag{A.1}$$

The corresponding Green function solution satisfies

$$(\nabla'^2 + k^2)G(\bar{r} - \bar{r}') = -\delta(\bar{r} - \bar{r}') \tag{A.2}$$

$$G(\bar{r} - \bar{r}') = \frac{e^{-jk|\bar{r} - \bar{r}'|}}{4\pi|\bar{r} - \bar{r}'|} \tag{A.3}$$

where ∇' is the gradient along $\bar{r}'$.

We are going to consider an integral expression of the electric field in the $z \geq 0$ region and use it to find the explicit result in terms of propagation along the z-axis planes.

$$\int_V [G(\bar{r}')\nabla'^2 E(\bar{r}') - E(\bar{r}')\nabla'^2 G(\bar{r}')] \, dV' =$$

$$\int_V [G(\nabla'^2 E + k^2 E) - E(\nabla'^2 G + k^2 G)] \, dV' \overset{(A.1),\,(A.2)}{=}$$

$$\int_V E(\bar{r}')\delta(\bar{r} - \bar{r}') \, dV' = E(\bar{r})u_V(\bar{r}) = \begin{cases} E(\bar{r}) & \text{if } r \in V \\ 0 & \text{otherwise} \end{cases} \tag{A.4}$$

where $u_V(\bar{r})$ is the indicator function on the volume V.

We make use of the Green's second identity to recast the expression into a surface integral form

$$\int_V [G\nabla'^2 E - E\nabla'^2 G] \, dV' = -\oint_{S+C} \left[G\frac{\partial E}{\partial n'} - E\frac{\partial G}{\partial n'} \right] dS'$$
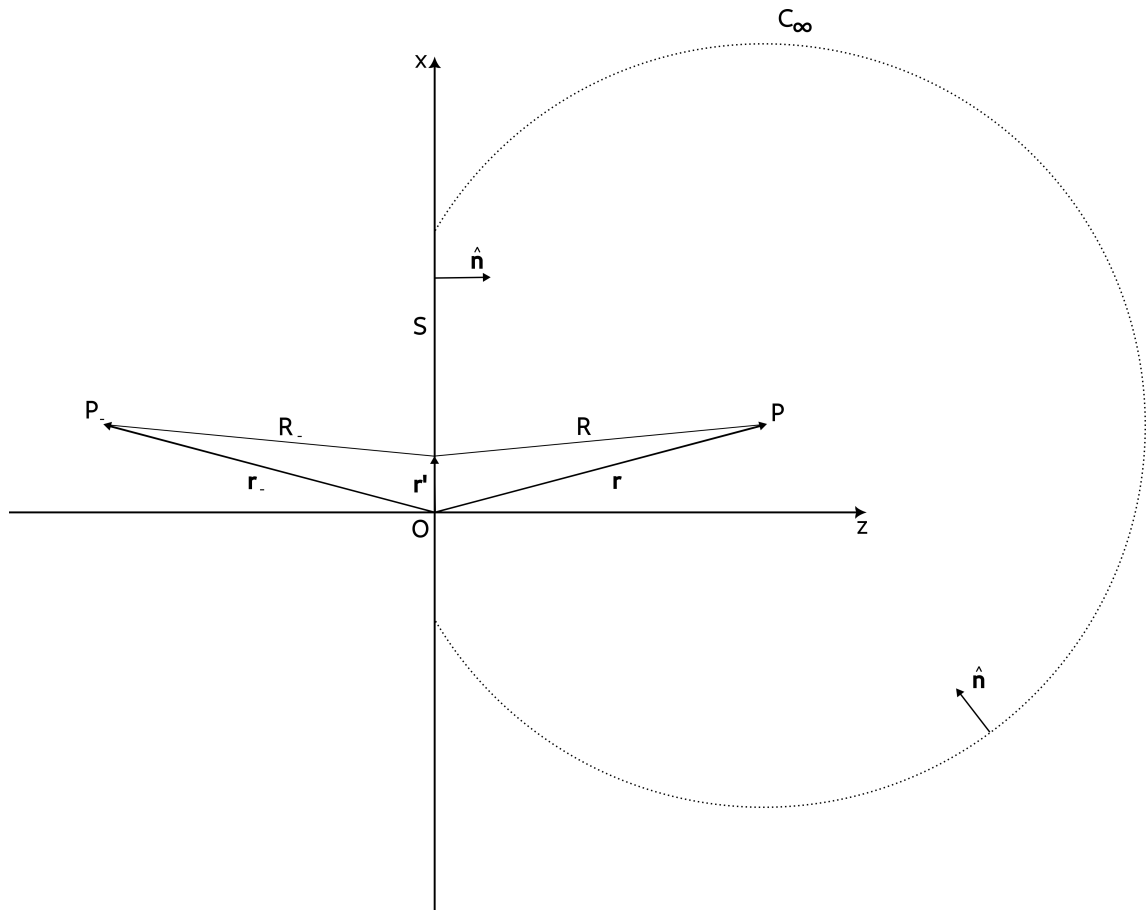
Figure A.1: Rayleigh-Sommerfield integral derivation figure

A physical *radiating* source should create waves that decay consistently with *Sommerfield's radiation condition*, which fixes the boundary conditions of the Helmholtz equation (Equation A.1) over the specified volume:

$$r\left(\frac{\partial E}{\partial r} + jkE\right) \to 0, \quad \text{for } r \to \infty \tag{A.5}$$

By sending its radius of the spheric cap to infinity $(C \to C_\infty)$ and by applying the condition (Equation A.5) to the electric field E and the Green solution G, we obtain that the surface integral over C_∞ vanishes:

$$-\int_{C_\infty}\left[G\frac{\partial E}{\partial n'} - E\frac{\partial G}{\partial n'}\right]dS' = -\int_{C_\infty}\left[G\left(\frac{\partial E}{\partial r'} + jkE\right) - E\left(\frac{\partial G}{\partial r'} + jkG\right)\right]dS' = 0$$

By putting together Equation A.4 we find:

$$E(\bar{r})u_V(\bar{r}) = \int_S\left[E\frac{\partial G}{\partial n'} - G\frac{\partial E}{\partial n'}\right]dS' \tag{A.6}$$

The reflected Green's function is introduced to simplify the calculations

$$G_-(\bar{r}, \bar{r}') = G(\bar{r}_- - \bar{r}') \tag{A.7}$$

in particular the point $\bar{r}_-$ is defined as the reflection of the observation point $\bar{r}$ respect to xy-plane, so that $\bar{r}_- = (r_x, r_y, -r_z)$ given $\bar{r} = (r_x, r_y, r_z)$.

The choice is justified due to Equation A.6, which has a vanishing LHS in the negative z-axis region; assuming $\bar{r}$ being located on the positive z-axis coordinates:

$$E(\bar{r}) = \int_S\left[E\frac{\partial G}{\partial n'} - G\frac{\partial E}{\partial n'}\right]dS'$$
$$0 = E(\bar{r}_-) = \int_S\left[E\frac{\partial G_-}{\partial n'} - G_-\frac{\partial E}{\partial n'}\right]dS' \tag{A.8}$$

Since the integral is performed on $z = 0$ plane, then $G = G_-$; the subtraction of terms of Equation A.8 result in a simplification;

$$E(\bar{r}) = \int_S E(\bar{r}')\frac{\partial}{\partial n'}(G - G_-)\,dS' \tag{A.9}$$

for $\hat{n} = \hat{z}$:

$$\frac{\partial G}{\partial n'} = \frac{\partial G}{\partial z'}\bigg|_{z=0}, \quad \frac{\partial G_-}{\partial n'} = \frac{\partial G_-}{\partial z'}\bigg|_{z=0} = -\frac{\partial G}{\partial z'}\bigg|_{z=0}$$

The derivative rispect to z-axis of the Green's function can be easily calculated:

$$-\frac{\partial G}{\partial z}\bigg|_{z'=0} = \frac{\partial G}{\partial z'}\bigg|_{z'=0} = \frac{z}{R}\left(jk + \frac{1}{R}\right)\frac{e^{-jkR}}{4\pi R}$$

where $R = |\bar{r} - \bar{r}'|$

So, finally the Rayleigh-Sommerfield formula:

$$E(\bar{r}) = 2 \int_S \frac{z}{R} \left(jk + \frac{1}{R} \right) \frac{e^{-jkR}}{4\pi R} \cdot E(\bar{r}') \, dS' \tag{A.10}$$

which can be rewritten in cartesian coordinates:

$$E(x, y, z) = 2 \int_{-\infty}^{+\infty} \int_{-\infty}^{+\infty} \frac{z}{R} \left(jk + \frac{1}{R} \right) \frac{e^{-jkR}}{4\pi R} \cdot E(x', y', 0) \, dx' dy' \tag{A.11}$$

where $R = |\bar{r} - \bar{r}'| = \sqrt{(x - x')^2 + (y - y')^2 + z^2}$

In should be reminded that the result validity is limited to the transverse optical planes along the optical axis; this condition is general enough for the treatment of a large class of applications.

Bibliography

[1] Chang-Ling Chung et al. "Plug-and-play adaptive optics for two photon high-speed volumetric imaging". In: *Journal of Physics: Photonics* 4.2 (2022), p. 024003. DOI: 10.1088/2515-7647/ac6120. URL: https://doi.org/10.1088/2515-7647/ac6120.

[2] Richard Davies and Markus Kasper. "Adaptive Optics for Astronomy". In: *Annual Review of Astronomy and Astrophysics* 50.1 (2012), pp. 305–351. DOI: 10.1146/annurev-astro-081811-125447. URL: https://doi.org/10.1146%2Fannurev-astro-081811-125447.

[3] Delphine Débarre, Martin J. Booth, and Tony Wilson. "Image based adaptive optics through optimisation of low spatial frequencies". In: *Opt. Express* 15.13 (2007), pp. 8176–8190. DOI: 10.1364/OE.15.008176. URL: https://opg.optica.org/oe/abstract.cfm?URI=oe-15-13-8176.

[4] Delphine Débarre et al. "Adaptive optics for structured illumination microscopy". In: *Optics Express* 16.13 (June 2008), p. 9290. DOI: 10.1364/oe.16.009290. URL: https://doi.org/10.1364/oe.16.009290.

[5] Tommaso Furieri. *Adaptive optical microscopy using the pupil segmentation*. https://hdl.handle.net/20.500.12608/24283. 2019. URL: https://hdl.handle.net/20.500.12608/24283.

[6] Joseph W Goodman. *Introduction to Fourier optics*. Vol. 1. 2005.

[7] Karen M. Hampson et al. "Adaptive optics for high-resolution imaging". In: *Nature Reviews Methods Primers* 1.1 (Oct. 2021). DOI: 10.1038/s43586-021-00066-7. URL: https://doi.org/10.1038/s43586-021-00066-7.

[8] Ulrich Kubitscheck, ed. *Fluorescence microscopy*. en. 2nd ed. Weinheim, Germany: Wiley-VCH Verlag, Apr. 2017.

[9] Fang Lei and Hans J. Tiziani. *A comparison of methods to measure the modulation transfer function of aerial survey lens systems from the image structures*. en. 1988. DOI: 10.18419/OPUS-4342. URL: http://elib.uni-stuttgart.de/handle/11682/4359.

[10] Ruizhe Lin et al. "Subcellular three-dimensional imaging deep through multicellular thick samples by structured illumination microscopy and adaptive optics". In: *Nature Communications* 12.1 (2021). DOI: 10.1038/s41467-021-23449-6. URL: https://doi.org/10.1038/s41467-021-23449-6.

[11] Dong C. Liu and Jorge Nocedal. "On the limited memory BFGS method for large scale optimization". In: *Mathematical Programming* 45.1-3 (Aug. 1989), pp. 503–528. DOI: 10.1007/bf01589116. URL: https://doi.org/10.1007/bf01589116.

[12] Kuo Niu and Chao Tian. "Zernike polynomials and their applications". In: *Journal of Optics* 24.12 (2022), p. 123001. DOI: 10.1088/2040-8986/ac9e08. URL: https://dx.doi.org/10.1088/2040-8986/ac9e08.

[13] S. J. Orfanidis. *Electromagnetic Waves and Antennas*. 2016. URL: https://www.ece.rutgers.edu/~orfanidi/ewa.

[14] Zhongya Qin et al. "Adaptive optics two-photon microscopy enables near-diffraction-limited and functional retinal imaging in vivo". In: *Light: Science &amp Applications* 9.1 (2020). DOI: 10.1038/s41377-020-0317-9. URL: https://doi.org/10.1038/s41377-020-0317-9.

[15] Ali Rahimi and Benjamin Recht. "Random Features for Large-Scale Kernel Machines". In: *Proceedings of the 20th International Conference on Neural Information Processing Systems*. NIPS'07. Vancouver, British Columbia, Canada: Curran Associates Inc., 2007, 1177–1184. ISBN: 9781605603520. DOI: 10.5555/2981562.2981710.

[16] B.S. Reddy and B.N. Chatterji. "An FFT-based technique for translation, rotation, and scale-invariant image registration". In: *IEEE Transactions on Image Processing* 5.8 (Aug. 1996), pp. 1266–1271. DOI: 10.1109/83.506761. URL: https://doi.org/10.1109/83.506761.

[17] F. Rigaut et al. "Gemini multiconjugate adaptive optics system review - I. Design, trade-offs and integration". In: *Monthly Notices of the Royal Astronomical Society* 437.3 (2013), pp. 2361–2375. DOI: 10.1093/mnras/stt2054. URL: https://doi.org/10.1093%2Fmnras%2Fstt2054.

[18] François Rigaut and Benoit Neichel. "Multiconjugate Adaptive Optics for Astronomy". In: *Annual Review of Astronomy and Astrophysics* 56.1 (Sept. 2018), pp. 277–314. DOI: 10.1146/annurev-astro-091916-055320. URL: https://doi.org/10.1146/annurev-astro-091916-055320.

[19] Lina Streich et al. "High-resolution structural and functional deep brain imaging using adaptive optics three-photon microscopy". In: *Nature Methods* 18.10 (2021), pp. 1253–1258. DOI: 10.1038/s41592-021-01257-6. URL: https://doi.org/10.1038/s41592-021-01257-6.

[20] M. Teich et al. "Adaptive particle image velocimetry based on sharpness metrics". In: *Journal of the European Optical Society-Rapid Publications* 14.1 (2018). DOI: 10.1186/s41476-018-0073-0. URL: https://doi.org/10.1186%2Fs41476-018-0073-0.

[21] Michael Totzeck. "Validity of the scalar Kirchhoff and Rayleigh–Sommerfeld diffraction theories in the near field of small phase objects". In: *Journal of The Optical Society of America A-optics Image Science and Vision* 8 (1991), pp. 27–32. URL: https://api.semanticscholar.org/CorpusID:121858773.

[22] Hans R. G. W. Verstraete et al. "Wavefront sensorless adaptive optics OCT with the DONE algorithm for in vivo human retinal imaging [Invited]". In: *Biomedical Optics Express* 8.4 (Mar. 2017), p. 2261. DOI: 10.1364/boe.8.002261. URL: https://doi.org/10.1364/boe.8.002261.

[23] H.R.G.W. Verstraete. "Optimization-based adaptive optics for optical coherence tomography". PhD thesis. 2017. DOI: 10.4233/UUID:F6059AB2-ADB2-4647-81BE-09847FA9BD9F. URL: http://resolver.tudelft.nl/uuid:f6059ab2-adb2-4647-81be-09847fa9bd9f.